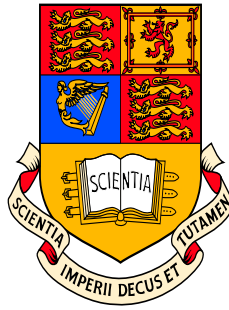# Study of the rare decay $B^0 \rightarrow \pi^0 \pi^0$ at *BABAR*

D. A. Bowerman

Imperial College of Science Technology and Medicine.

A thesis submitted for the degree of
Doctor of Philosophy
of The University of London
and the Diploma of Imperial College.

October, 2002

Abstract

The *BABAR* experiment operating at the PEP-II e^+e^- collider is designed to study *CP* violation effects in the B-meson system. From May 1999 to June 2002 approximately $81\,\mathrm{fb}^{-1}$ of data have been collected at the $\Upsilon(4S)$ resonance, containing (87.9 ± 1.4) Million $B\overline{B}$ pairs.

From this data sample the branching fraction for the decay $B^0 \to \pi^0\pi^0$ has been extracted using a multi-dimensional maximum likelihood technique. With an efficiency of 20.4%, we find $36^{+15\ +1}_{-14\ -1}$ $B^0 \to \pi^0\pi^0$ events and measure the branching fraction to be

$$\mathcal{B}(B^0 \to \pi^0\pi^0) = (2.0^{+0.9\ +0.3}_{-0.8\ -0.2}) \times 10^{-6}$$

where the first error is statistical and the second systematic. The statistical significance is 3.1σ and we report an upper limit of

$$\mathcal{B}(B^0 \to \pi^0\pi^0) < 3.6 \times 10^{-6}\ (90\%CL).$$

The results of the fit are confirmed using a simple cut based analysis technique.

Acknowledgements

to Richard James, Anthony Pellegrini and Mick who gave me career and life advice at difficult times. I hope this thesis proves you were right!

Great thanks must go to my family, who have supported me throughout my academic career and in everything I've tried to achieve. Mum, Dad, Sarah, and Mr.Hootie, I love you lots and thanks for everything. Most of all I would like to thank Jane. Since the first day at Datamonitor, through many wonderful days in Palo Alto and to the last at Notting Hill, my life has been so much brighter for her presence. Without doubt I've had the time of my life with her these last three years. This thesis is dedicated to Jane.

Author's Contribution

The author has worked for the past three years on the *BABAR* experiment. The crosstalk measurements described in chapter 3 and the subsequent analysis was performed in conjunction with Martin Kocian. The author developed the entire measurement procedure and took a substantial role in the actual data taking. The subsequent characterisation of the crosstalk in different regions of the detector was performed entirely by the author. The final electronics calibration correction was developed in conjunction with Martin Kocian.

The $B^0 \to \pi^0\pi^0$ branching fraction analysis, described in chapters 4,5 and 6 was developed with help from Adrian Bevan and the Charmless Two-body working group at SLAC. The analysis is similar to the official *BABAR* analysis described in [22] as the author played a large part in its development. There are substantial differences between the two and the final analysis and work presented in this thesis have been carried out solely by the author.

Contents

List of Figures

List of Tables

Chapter 1

CP Violation in the B Meson System

1.1   Introduction

The charge conjugation operator, $\widehat{C}$, transforms a particle to its antiparticle, while the parity operator, $\widehat{P}$, acts on space-time so that $t \to t$ and $\underline{r} \to -\underline{r}$. When it was discovered in 1956 [1] that the weak interactions were not invariant under the $\widehat{C}$ and $\widehat{P}$ transformations separately, it was expected that the weak interaction respected the combined CP transformation.

The first evidence for CP violation came from Cronin and Fitch in 1964 [2]. They observed small CP violating effects in the decay of K^0 mesons, through the observation that the $K^0_L \to \pi^+\pi^-$ decay occurs.

CP violation fits easily into the Standard Model (SM) of particle physics through the three generations of quarks. This gives rise to complex couplings between the quark flavours which in turn leads to CP violation.

CP violation is one of the three Sakharov conditions needed to explain the baryon asymmetry in the universe [3], but the amount of CP violation predicted by the SM is too small to explain the baryon asymmetry we see. While CP violation was

discovered some time ago, it remains one of the least well tested areas of the SM. It is therefore vital to probe CP violating effects to fully test the SM, and possibly see new physics.

The B meson sector is expected to provide many stringent tests of the SM description of CP violation. Two dedicated B meson experiments, *BABAR* and BELLE, are currently in operation, and recently saw the first evidence for CP violation in the B sector [4] [5].

In this chapter the formalism for describing B meson physics will be introduced, and the SM description of CP violation through the CKM quark coupling matrix will be discussed. The three types of possible CP violation will be described. The chapter concludes by describing how CP violation can be measured at *BABAR*. Particular detail is given to the measurement of the CP violating asymmetry $\sin(2\alpha)$ and the role of the decay $B^0 \rightarrow \pi^0\pi^0$ in this measurement. A more thorough description of CP violation in the B sector is given in [10], [11] and they provide the basis for much of the discussion in this section.

1.2   Neutral B meson mixing

1.2.1   Introduction

Mixing occurs in the SM from box diagrams of the type shown in Figure 1.1. The process has been observed in the neutral K and B systems. This section describes the quantum mechanics of the two state system of neutral B mesons, but the general formalism is valid for the K system also. Within the neutral B sector we have two different systems, one involving a b-type quark and a d-type quark giving a B_d meson, the other involving a b-type quark and a s-type quark giving a B_s meson. We limit our discussion to the mixing of B_d mesons as these are the type produced at *BABAR*. Mixing plays a major role in our understanding of CP violation and its measurement. This role is further discussed in section 1.4.2.
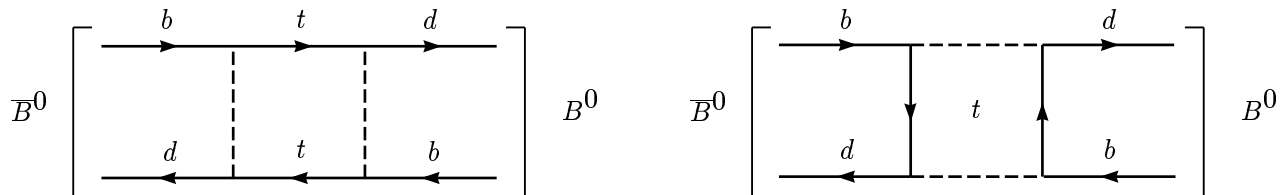
Figure 1.1: Box diagrams for B^0–$\bar{B}^0$ mixing in the Standard Model.

1.2.2   Mixing formalism

In discussing the formalism of mixing, it is necessary to define two different types of state that play a role. Firstly there are flavour eigenstates which have definite quark content. For B mesons these are the B^0 which consists of $\bar{b}d$ quarks, and the $\bar{B}^0$ which has $b\bar{d}$ quarks. These are useful to understand particle production and decay processes. Secondly there are eigenstates of the electroweak Hamiltonian, which are states of definite mass and lifetime and so propogate through space in a definite fashion.

A general state can be constructed from a linear combination of the flavour states $|B^0\rangle$ and $|\bar{B}^0\rangle$

$$|B(t)\rangle = a|B^0\rangle + b|\bar{B}^0\rangle. \tag{1.1}$$

The development of $|B(t)\rangle$ is governed by a time-dependent Schrodinger equation

$$i\frac{\partial}{\partial t}\begin{pmatrix} a \\ b \end{pmatrix} = H\begin{pmatrix} a \\ b \end{pmatrix} \equiv (M - \frac{i}{2}\Gamma)\begin{pmatrix} a \\ b \end{pmatrix} \tag{1.2}$$

where M and Γ are 2×2 Hermitian matrices. CPT invariance leads to the diagonal elements of H being equal (e.g. $H_{11} = H_{22}$). The off-diagonal terms, M_{12} and Γ_{12}, represent the dispersive and absorbative parts of the transition amplitudes from B^0 to $\bar{B}^0$. If there is no CP violation then the overall off-diagonal terms of H are equal also.

Diagonalising H gives rise to the mass eigenstates which are given by

$$|B_L\rangle = p|B^0\rangle + q|\bar{B}^0\rangle \tag{1.3}$$

$$|B_H\rangle = p|B^0\rangle - q|\bar{B}^0\rangle \tag{1.4}$$

which are known as the *Heavy* and *Light* mass eigenstates, where the complex coefficients p and q obey the normalization condition

$$\mid q \mid^2 + \mid p \mid^2 = 1. \tag{1.5}$$

Within the mixing framework it is useful to define the mass and width difference between the neutral B mesons

$$\Delta m_B \equiv M_H - M_L, \qquad \Delta\Gamma_B \equiv \Gamma_H - \Gamma_L \tag{1.6}$$

so that Δm_B is positive by definition. Finding the eigenvalues of 1.2 gives rise to the ratio of p and q which will prove useful in our future discussions of CP violation in the B sector

$$\frac{q}{p} = -\frac{\Delta m_B - \frac{i}{2}\Delta\Gamma_B}{2(M_{12} - \frac{i}{2}\Gamma_{12})}. \tag{1.7}$$

1.2.3   Time evolution of neutral B mesons

Within the neutral B sector, the difference between the lifetime of the weak eigenstates is expected to be very small

$$\Delta\Gamma_B/\Gamma_B = \mathcal{O}(10^{-2}) \tag{1.8}$$

where

$$\Gamma_B = \frac{1}{2}(\Gamma_H + \Gamma_L). \tag{1.9}$$

While $\Delta\Gamma_{B_d}$ has not been measured, this is a rather safe prediction. The difference in width is produced by decay channels common to the B^0 and $\overline{B}^0$ and the branching fractions for such decays are at the 10^{-3} level. As various channels contribute with differing signs we expect that their sum will not be greater than the individual level, therefore $\Delta\Gamma_{B_d} \ll \Gamma_{B_d}$.

The difference in mass between the mass eigenstates, Δm_{B_d}, has been measured [6]

$$x_d \equiv \Delta m_B/\Gamma_B = 0.730 \pm 0.029 \tag{1.10}$$

therefore

$$\Delta\Gamma_B \ll \Delta m_B. \tag{1.11}$$

A general B state $|\Psi(t)\rangle$ can be written as an admixture of the B_H and B_L states which evolve in time

$$|\Psi(t)\rangle = a_H(t)|B_H\rangle + a_L(t)|B_L\rangle \tag{1.12}$$

where the amplitudes are given by

$$a_H(t) = a_H(0)e^{-iM_H t}e^{-\frac{1}{2}\Gamma_H t}, \qquad a_L(t) = a_L(0)e^{-iM_L t}e^{-\frac{1}{2}\Gamma_L t}. \tag{1.13}$$

So a state which is created at $t = 0$ as initially pure $|B^0\rangle$ has $a_L(0) = a_H(0) = 1/(2p)$. Similarly $a_L(0) = -a_H(0) = 1/(2q)$ would represent an initial $|\overline{B}^0\rangle$ state. The time evolution of these states is therefore given by

$$|B^0(t)\rangle = g_+(t)|B^0\rangle + (q/p)g_-(t)|\overline{B}^0\rangle \tag{1.14}$$

$$|\overline{B}^0(t)\rangle = (p/q)g_-|B^0\rangle + g_+(t)|\overline{B}^0\rangle \tag{1.15}$$

where

$$g_+(t) = e^{-iMt}e^{-\Gamma_B t/2}\cos(\Delta m_B t/2) \tag{1.16}$$

$$g_-(t) = e^{-iMt}e^{-\Gamma_B t/2}i\sin(\Delta m_B t/2) \tag{1.17}$$

where $M = \frac{1}{2}(M_L + M_H)$ and it is assumed that the lifetime difference between the states is zero so $\Gamma_L = \Gamma_H = \Gamma_B$.

1.2.4 Time evolution for coherent $B\overline{B}$ states

At *BABAR* e^+e^- are collided to produce a boosted $\Upsilon(4S)$ which then decays to a $B\overline{B}$ pair. The B^0 and $\overline{B}^0$ mesons produced from the decay are in a coherent $L = 1$ state. This means that each of the two particles evolves in time as described in section 1.2.3. They do however evolve in phase meaning that at any particular time before decay, there is exactly one B^0 and one $\overline{B}^0$ present. Once one of the particles decays, the other continues to evolve so there are possible events with two B^0 or two $\overline{B}^0$ decays.

The coherent state of the $B\overline{B}$ pair allows us to investigate the mixing between the B and $\overline{B}$ states. If one meson, say the B^0, decays at time $(t = t_{tag})$, then the other meson must be a $\overline{B}^0$ at that time. The $\overline{B}^0$ will continue to evolve before decaying at some later time $(t = t_{decay})$.

By tagging the flavour of the first B decay through its decay to leptons or kaons, we know the flavour of the second B at that time. If we fully reconstruct the decay of the second in a flavour specific decay mode B then its flavour at $(t = t_{decay})$ is known. By measuring the distance between the two decay vertices it is possible to measure the time difference $(\Delta(t) = t_{decay} - t_{tag})$ and so know the time the second B had to mix flavours. It is therefore possible to map out the time dependence of the mixing parameters.

1.3   *CP* Violation in the Standard Model

1.3.1   The CKM matrix

The electroweak Lagrangian, before symmetry breaking, may be written as

$$-\mathcal{L} = \frac{g}{\sqrt{2}}(\overline{u}_L^I \overline{c}_L^I \overline{t}_L^I)\gamma^\mu \begin{pmatrix} d_L^I \\ s_L^I \\ b_L^I \end{pmatrix} W_\mu^+ + h.c. \tag{1.18}$$

where g is the weak coupling constant, γ^μ are the Dirac matrices, I denotes the interaction states, L denotes the left handed projections of the fermion fields u, and W_μ^+ are the charged weak bosons. The weak interaction allows fields to couple with one another, so the resulting observed mass eigenstates are mixed states of the original quarks. Representing the transformations by which the original mass matrix is diagonalised by V_{iL} and V_{iR} for the left and right fermionic fields i, one has that

$$V_{dL} M_d V_{dR}^\dagger = M_d^{diag} \tag{1.19}$$

$$V_{uL} M_u V_{uR}^\dagger = M_u^{diag} \tag{1.20}$$

which gives a Lagrangian of

$$-\mathcal{L} = \frac{g}{\sqrt{2}}(\overline{u}_L\overline{c}_L\overline{t}_L)\gamma^\mu V_{uL}V_{dL}^\dagger \begin{pmatrix} d_L \\ s_L \\ b_L \end{pmatrix} W_\mu^+ + h.c. \tag{1.21}$$

One may then define a matrix V such that

$$V = V_{uL}V_{dL}^\dagger = \begin{pmatrix} V_{ud} & V_{us} & V_{ub} \\ V_{cd} & V_{cs} & V_{cb} \\ V_{td} & V_{ts} & V_{tb} \end{pmatrix} \tag{1.22}$$

V is the Cabibbo-Kobayashi-Maskawa (CKM) matrix [12]. The CKM matrix is necessarily unitary, such that

$$VV^\dagger = 1. \tag{1.23}$$

A general $n{\times}n$ complex matrix has $2n^2$ parameters. Because it is unitary there are n^2 constraints. Of the remaining parameters, 3 can be written as angles related to the number of independent rotations in 3 dimensions, and the remaining 6 are phases. It is possible to remove 5 of the CKM phases by unobservable quark phase redefinitions, leaving one irremovable phase. This phase has the ability to introduce *CP* violation and it lead Kobayashi and Maskawa [7] to suggest a third quark generation long before there was any experimental evidence for it. Hence this phase is known as the Kobayashi-Maskawa phase.

The irremovable phase allows *CP* violation to occur. If we consider the expanded form of the charged current Lagrangian from equation 1.21

$$-\mathcal{L} = \frac{g}{\sqrt{2}}[(\overline{u}_i\gamma^\mu W^{+\mu}(1-\gamma^5)V_{ij}d_j) + (\overline{d}_j\gamma^\mu W^{-\mu}(1-\gamma^5)V_{ij}^*u_i)] \tag{1.24}$$

where $\frac{1}{2}(1-\gamma^5)$ is the left handed projection operator. The *CP* operator transforms terms in this equation such that

$$\overline{\psi}_i\psi_j \rightarrow \overline{\psi}_j\psi_i, \qquad \overline{\psi}_i\gamma^\mu W_\mu(1-\gamma_5)\psi_j \rightarrow \overline{\psi}_j\gamma^\mu W_\mu(1-\gamma_5)\psi_i \tag{1.25}$$

so that applying the transformations to equation 1.24 exchanges the terms except that V_{ij} and V_{ij}^* are not interchanged. If all the elements of V_{ij} are real then the two terms remain unchanged, but if there are complex elements to V_{ij} then *CP* violation can occur.

There are many parameterisations of the CKM matrix; the standard one is given by

$$V = \begin{pmatrix} c_{12}c_{13} & s_{12}c_{13} & s_{13}e^{-i\delta_{KM}} \\ -s_{12}c_{23} - c_{12}s_{23}s_{13}e^{-i\delta_{KM}} & c_{12}c_{23} - s_{12}s_{23}s_{13}e^{-i\delta_{KM}} & s_{23}c_{13} \\ s_{12}c_{23} - c_{12}c_{23}s_{13}e^{-i\delta_{KM}} & -c_{12}s_{23} - s_{12}c_{23}s_{13}e^{-i\delta_{KM}} & c_{23}c_{13} \end{pmatrix} \quad (1.26)$$

where $s_{ij} = \sin\theta_{ij}$, $c_{ij} = \cos\theta_{ij}$, θ_{ij} denotes the mixing angle between the ith and j^{th} generations and δ_{KM} is the Kobayashi-Maskawa complex phase. Wolfenstein noticed that $c_{13} \approx 1$ and that experimentally $s_{12} \approx 0.22$. Using a small angle approximation he developed the *standard* Wolfenstein approximation [8]

$$V = \begin{pmatrix} 1 - \lambda_W^2/2 & \lambda_W & A\lambda_W^3(\rho - i\eta) \\ -\lambda_W & 1 - \lambda_W^2/2 & A\lambda_W^2 \\ A\lambda_W^3(1 - \rho - i\eta) & -A\lambda_W^2 & 1 \end{pmatrix} + \mathcal{O}(\lambda_W^4) \quad (1.27)$$

where λ_W is the sine of the Cabbibo angle, s_{12}, A and ρ are real numbers and the complex term is given by η.

1.3.2   The Unitarity Triangle

The unitarity of the CKM matrix (equation 1.23) implies nine different relations between the matrix elements. The most interesting for the B sector is given by

$$V_{ud}V_{ub}^* + V_{cd}V_{cb}^* + V_{td}V_{tb}^* = 0. \quad (1.28)$$

The relations of this sort can be expressed as triangles in the complex plane and are known as the unitarity triangles. The sides and angles of the unitarity triangles can be related to experimentally measurable quantities. Each of the triangles has an area which effectively represents the amount of *CP* violation. Unlike the other relations, equation 1.29 is particularly interesting as all the individual terms are of the same order of magnitude, meaning that the triangle formed is relatively open so predicting large, measurable *CP* asymmetries in the B sector.

The rescaled unitarity triangle is shown in figure 1.2 as it sits in the complex plane. This form comes from choosing a phase convention such that $(V_{cd}V_{cb}^*)$ is real and by dividing the sides by $|V_{cd}V_{cb}^*|$. This gives a triangle with one side with a length of
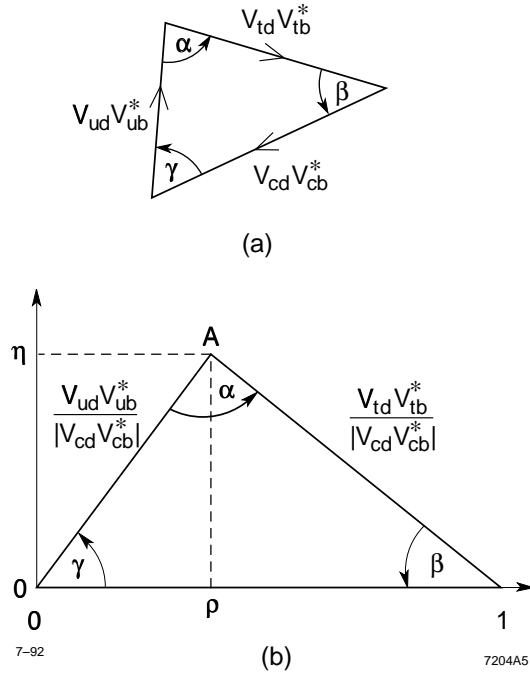
Figure 1.2: The unitarity triangle. The upper plot shows an unscaled version, whille the lower plot shows a version scaled as described in the text. The apex of the triangle is at $(\rho(1-\frac{\lambda_W^2}{2}), \eta(1-\frac{\lambda_W^2}{2}))$.

one along the real axis. Two vertices of the triangle are fixed at (0,0) and (1,0) and the third vertex is given by the $(\overline{\rho}, \overline{\eta})$ where

$$\overline{\rho} = \left(1 - \frac{\lambda_W^2}{2}\right)\rho \quad \text{and} \quad \overline{\eta} = \left(1 - \frac{\lambda_W^2}{2}\right)\eta. \tag{1.29}$$

The unitarity triangle in the $(\overline{\rho}, \overline{\eta})$ plane gives angles α, β and γ defined as

$$\alpha \equiv arg\left[-\frac{V_{td}V_{tb}^*}{V_{ud}V_{ub}^*}\right], \qquad \beta \equiv arg\left[-\frac{V_{cd}V_{cb}^*}{V_{td}V_{tb}^*}\right], \qquad \gamma \equiv arg\left[-\frac{V_{ud}V_{ub}^*}{V_{cd}V_{cb}^*}\right]. \tag{1.30}$$

These angles are directly related to physical quantities and can be measured by CP asymetries in various B decays.

1.4   The 3 Types of CP Violation

There are three ways in which CP violation may occur in the SM, these are:

1. CP violation in decay;

2. *CP* violation in mixing;

3. *CP* violation in the interference between decays with and without mixing;

This section describes these three processes.

1.4.1   *CP* violation in decay

CP violation in decay is governed by the value of $l = |\overline{A}_{\overline{f}}/A_f|$, where A_f represents the amplitude for the B^0 decaying to the final state f and $\overline{A}_{\overline{f}}$ is the amplitude for the $\overline{B}^0$ decaying to the final state $\overline{f}$. It turns out that the quantity l is independent of phase conventions and is physically meaningful. *CP* violation occurs in decay if $l \neq 1$ and is caused by the interference of different decay amplitudes. *CP* violation in decay is often also known as *direct CP* violation.

Two types of phase can appear in A_f and $\overline{A}_{\overline{f}}$. Complex terms in the Lagrangian term contributing to the amplitude will appear in conjugate form between the two conjugate amplitudes. Their phases therefore appear with opposite sign in A_f and $\overline{A}_{\overline{f}}$. These complex *CP* violating terms occur only in the electroweak sector through the CKM matrix as was discussed in section 1.3, consequently these phases are often known as *weak* phases.

The second type of phase that can enter the decay amplitude are known as the *strong* phases as they originate from terms describing rescattering processes which are dominated by the strong force. Such terms do not violate *CP* as they enter A_f and $\overline{A}_{\overline{f}}$ with the same sign. For both sets of phases, it is only the relative phase shift that has physical meaning. A global phase shift has no physical consequence.

We can express the amplitudes A as the contribution of three parts; $|A_i|$ its magnitude, $e^{i\phi_i}$ its weak phase, and $e^{i\delta_i}$ its strong phase component. If several amplitudes contribute to the process $B \rightarrow f$, then A_f can be expressed as

$$A_f = \sum_i |A_i| e^{i(\delta_i + \phi_i)} \tag{1.31}$$

We can also express the quantity l as

$$l = \left| \frac{\overline{A}_{\overline{f}}}{A_f} \right| = \left| \frac{\sum_i |A_i| e^{i(\delta_i - \phi_i)}}{\sum_i |A_i| e^{i(\delta_i + \phi_i)}} \right|. \tag{1.32}$$

where we can see that the weak phase enters the conjugate process with a different sign. For $l \neq 1$ meaning that direct CP violation occurs, it is necessary that at least two terms entering the amplitudes having different weak phases also acquire different strong phases. This is because

$$|A|^2 - |\overline{A}|^2 = -2 \sum_{i,j} |A_i||A_j| \sin(\phi_i - \phi_j) \sin(\delta_i - \delta_j) \tag{1.33}$$

so that if either the strong or weak phases are the same for a given process then the conjugate amplitude magnitudes are equal giving $l = 1$, and there is no CP violation.

CP violation in decay is typically described by the time integrated asymmetry

$$a_f = \frac{\Gamma(B \to f) - \Gamma(\overline{B} \to \overline{f})}{\Gamma(B \to f) + \Gamma(\overline{B} \to \overline{f})} \tag{1.34}$$

which in terms of the decay amplitudes is given by

$$a_f = \frac{1 - |\overline{A}/A|^2}{1 + |\overline{A}/A|^2} = \frac{1 - l^2}{1 + l^2}. \tag{1.35}$$

CP violation in decay can occur in both charged and neutral B meson decay. Typically we look for direct CP violation in charged modes as it is the only process that can give CP violation, while in the neutral modes it competes with the other processes described in this section. The only evidence so far seen for direct CP violation is in the kaon system [9].

1.4.2 CP violation in mixing

Expanding the notation and arguments developed in section 1.2.2, it is possible to attain a second quantity like l that is independent of phase conventions and is physically meaningful

$$\left| \frac{q}{p} \right|^2 = \left| \frac{M_{12}^* - \frac{i}{2} \Gamma_{12}^*}{M_{12} - \frac{i}{2} \Gamma_{12}} \right| \tag{1.36}$$

If *CP* is conserved, the mass eigenstates would be *CP* eigenstates and this would lead to the relative phase between M_{12} and Γ_{12} vanishing giving equation 1.36 equal to 1. Therefore *CP* violation in mixing, or *indirect CP* violation as it is often known, requires that

$$\left| \frac{q}{p} \right| \neq 1 \tag{1.37}$$

or in other words, that the mass eigenstates are different from *CP* eigenstates. *CP* violation in mixing has been seen in the kaon system through semileptonic decays. The asymmetry of interest is given by

$$\delta_l = \frac{\Gamma(K_L \to l^+ \overline{\nu} X) - \Gamma(K_L \to l^- \nu X)}{\Gamma(K_L \to l^+ \overline{\nu} X) + \Gamma(K_L \to l^- \nu X)} \tag{1.38}$$

where the large difference between the K_S and K_L lifetimes makes it straightforward to produce a beam of K_L with which to make the measurement. The current world averages for these measurements are [6]

$$\delta_l = (3.33 \pm 0.14) \times 10^{-3}. \tag{1.39}$$

As the lifetime difference between the mass eigenstates in the B sector is much smaller than that of the kaon sector, measuring indirect *CP* violation is far more challenging. Such a measurement could be possible through the time dependent asymmetry of neutral B decays to semileptonic states

$$a_{sl} = \frac{\Gamma(\overline{B}^0(t) \to l^+ \nu X) - \Gamma(B^0(t) \to l^- \nu X)}{\Gamma(\overline{B}^0(t) \to l^+ \nu X) + \Gamma(B^0(t) \to l^- \nu X)} \tag{1.40}$$

which in terms of $|q/p|$ is given by

$$a_{sl} = \frac{1 - |q/p|^4}{1 + |q/p|^4}. \tag{1.41}$$

From the discussion in section 1.2 we see that *CP* violation in mixing is expected to be small, of the order 10^{-2}, as $|q/p|$ is expected to be close to unity. While experimentally such a measurement is obviously challenging, there are also large theoretical uncertainties in the required calculation of Γ_{12} from the electroweak Hamiltonian discussed in section 1.2.2. Consequently, even if asymmetries are observed in the B sector it will be difficult to relate them to the CKM parameters of the SM.

1.4.3 CP violation in the interference between mixing and decay

There is one more quantity which is independent of phase conventions and physically meaningful and of interest in relation to CP violation

$$\lambda = \frac{q}{p}\frac{\overline{A}_{\overline{f}_{CP}}}{A_{f_{CP}}} \tag{1.42}$$

where $A_{f_{CP}}$ is the amplitude for the decay of the B^0 to a CP eigenstate (f_{CP}). When CP is conserved $|q/p| = 1$ and $|\overline{A}_{\overline{f}_{CP}}/A_{f_{CP}}| = 1$ and the relative phases between (q/p) and $(\overline{A}_{\overline{f}_{CP}}/A_{f_{CP}})$ vanishes. This means that

$$\lambda \neq \pm 1 \tag{1.43}$$

gives the condition for CP violation. Both CP violation in decay and through mixing give rise to the condition 1.43 through $|\lambda| \neq 1$, but it is also possible that $|q/p| = 1$ and $|\overline{A}/A| = 1$ yet there is still CP violation as

$$|\lambda| = 1, \qquad Im\lambda \neq 0. \tag{1.44}$$

This type of CP violation is known as *CP violation in the interference between decays with and without mixing*, or more commonly *CP violation in the interference between mixing and decay*.

From equations 1.14, 1.15, and 1.42 it is possible to define the time-dependent amplitudes for the decay of a B^0 or $\overline{B}^0$ to the CP eigenstate f_{CP}

$$\langle f_{CP}|\hat{H}|B^0(t)\rangle = A_{f_{CP}}(g_+(t) + \lambda g_-(t)) \tag{1.45}$$

$$\langle f_{CP}|\hat{H}|\overline{B}^0(t)\rangle = A_{f_{CP}}(p/q)(g_-(t) + \lambda g_+(t)). \tag{1.46}$$

Using the definitions of $g_+(t)$ and $g_-(t)$ given in equations 1.16 and 1.17 we can define the time dependent decay rates by taking the modulus squared of these amplitudes

$$\Gamma(t)(B^0 \to f_{CP}) = |A_{f_{CP}}|^2 e^{-\Gamma t}[\frac{1 + |\lambda|^2}{2} + \frac{1 + |\lambda|^2}{2}\cos(\Delta mt) - Im(\lambda)\sin(\Delta mt)]$$
$$\tag{1.47}$$

$$\Gamma(t)(\overline{B}^0 \to f_{CP}) = |A_{f_{CP}}|^2 e^{-\Gamma t} [\frac{1+|\lambda|^2}{2} - \frac{1-|\lambda|^2}{2}\cos(\Delta mt) + Im(\lambda)\sin(\Delta mt)].$$

(1.48)

CP violation in the interference of mixing and decay can be observed by comparing the asymmetry of these rates

$$a_{f_{CP}} = \frac{\Gamma(B^0(t) \to f_{CP}) - \Gamma(\overline{B}^0(t) \to f_{CP})}{\Gamma(B^0(t) \to f_{CP}) + \Gamma(\overline{B}^0(t) \to f_{CP})}$$

(1.49)

which from equations 1.47 and 1.48 can be expressed as

$$a_{f_{CP}} = \frac{(1-|\lambda|^2)\cos(\Delta mt) - 2Im(\lambda)\sin(\Delta mt)}{1+|\lambda|^2}.$$

(1.50)

This asymmetry will be non-vanishing if any of the three types of *CP* violation occur, but for *CP* violation in the interference between mixing and decay where $|\lambda| = 1$ the equation simplifies to give

$$a_{f_{CP}} = -Im\lambda\sin(\Delta mt).$$

(1.51)

CP violation of this form presents the most straightforward way of measuring *CP* violation in the *B* system. For *B* decays that are dominated by a single *CP* violating phase, so there is no direct *CP* violation, $a_{f_{CP}}$ can be cleanly related to CKM elements with very small theoretical uncertainties. Additionally for most *B* decays we expect $|\lambda| \approx 1$, meaning that both *CP* violation in decay and in mixing are expected to be small.

1.5   Measuring *CP* Violation at *BABAR*

1.5.1   Introduction

It is possible to measure the angles of the Unitarity triangle (section 1.3.2) by examining the decays of neutral *B* mesons to *CP* eigenstates. Equation 1.51 shows that the imaginary part of λ can be measured by the time dependent asymmetry given in equation 1.49. In this section an overview is given of the measurements of the angles β and α, the two measurements accessible to *BABAR*. Particular theoretical

and experimental attention is given to the measurement of α, as the measurement of $B^0 \to \pi^0\pi^0$ plays a crucial role in the procedure. The section and chapter concludes with the latest measurements of the CKM matrix elements and *CP* asymmetries β and α.

1.5.2   Measuring $\sin(2\beta)$ at *BABAR*
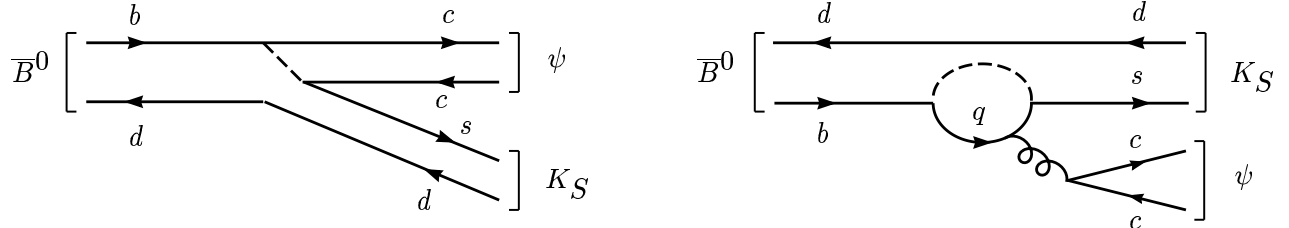
Figure 1.3: The tree (left) and penguin (right) Feynman diagrams for the decay $\overline{B}^0 \to J/\psi K_S$.

Various decays can be used to measure the angle β at *BABAR* [10]. The best method uses the decay of neutral B's to $J/\psi K_S$. The Feynman diagrams for the decay are shown in figure 1.3 both for the tree and penguin processes. In this case, λ as defined in equation 1.36 is given by three terms

$$\lambda(B^0 \to J/\psi K_S) = \left(\frac{q}{p}\right)_B \left(\frac{\overline{A}}{A}\right) \left(\frac{q}{p}\right)_K = -\left(\frac{V_{tb}^* V_{td}}{V_{tb} V_{td}^*}\right) \left(\frac{V_{cs}^* V_{cb}}{V_{cs} V_{cb}^*}\right) \left(\frac{V_{cd}^* V_{cs}}{V_{cd} V_{cs}^*}\right) \quad (1.52)$$

where the first term on the right comes from B^0-$\overline{B}^0$ mixing, the second from the ratio of the decay amplitudes for the B^0 and $\overline{B}^0$ to $J/\psi K_S$ and the third comes from K^0-$\overline{K}^0$ mixing. Hence, from the dominant tree diagram

$$Im\lambda(B^0 \to J/\psi K_S) = -\left(\frac{V_{tb}^* V_{td}}{V_{tb} V_{td}^*}\right) \left(\frac{V_{cd}^* V_{cb}}{V_{cd} V_{cb}^*}\right) = \sin(2\beta) \quad (1.53)$$

and from equation 1.51 the time dependent asymmetry for $B^0 \to J/\psi K_S$ is given by

$$a_{J/\psi K_S} = -Im\lambda \sin(\Delta mt) = -\sin(2\beta)\sin(\Delta mt). \quad (1.54)$$

There are several other neutral B decay modes that can be used to measure $\sin(2\beta)$ but they suffer from greater uncertainties than the $J/\psi K_S$ mode. The theoretical problems arise from penguin diagrams entering with potentially different weak

phases. The penguin diagram for $J/\psi K_S$ is shown in 1.3. The dominant penguin process for this mode, with c in the loop, has the same weak phase as the tree diagram. Penguin processes with different weak phases that could contribute (e.g u and t) are found to be heavily CKM suppressed. Therefore to good accuracy, $|\lambda| = 1$, and the simple relation between the *CP* asymmetry and $\sin(2\beta)$ has a very small theoretical uncertainty for this mode. Unfortunately this is not true of measuring other angles of the unitarity triangle as we will see in the following section.

1.5.3   Measuring $\sin(2\alpha)$ at ***BABAR***
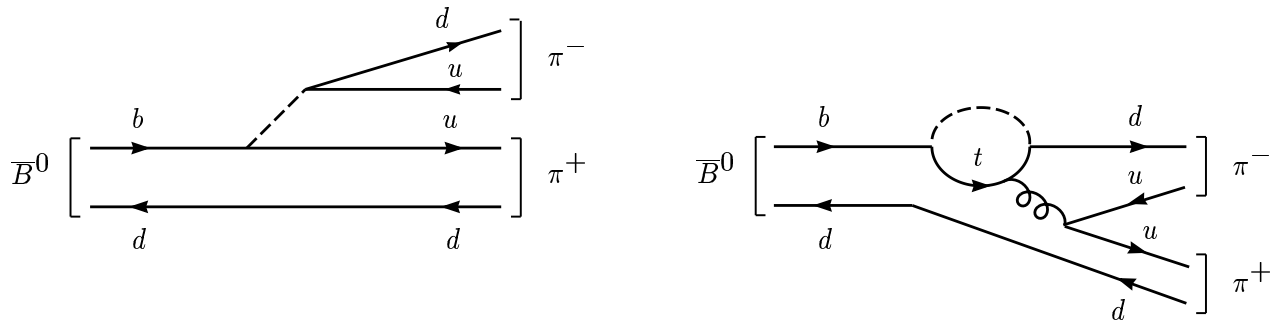
Figure 1.4: The tree (left) and penguin (right) Feynman diagrams for the decay $\overline{B}^0 \rightarrow \pi^+\pi^-$.

The decay $B^0 \rightarrow \pi^+\pi^-$ allows the determination of $\sin(2\alpha)$ in a similar way to $J/\psi K_S$ in the extraction of $\sin(2\beta)$. Taking the tree diagram shown in figure 1.4 we can define λ as

$$\lambda(B^0 \rightarrow \pi^+\pi^-) = \left(\frac{V_{tb}^*V_{td}}{V_{tb}V_{td}^*}\right)\left(\frac{V_{ub}V_{ud}^*}{V_{ub}^*V_{ud}}\right) \tag{1.55}$$

where we have no contribution from K^0 mixing. The imaginary part of λ is then

$$Im\lambda(B^0 \rightarrow \pi^+\pi^-) = \sin(2(\pi - \beta - \gamma)) = \sin(2\alpha) \tag{1.56}$$

and the time dependent asymmetry is given by

$$a_{\pi^+\pi^-} = -Im\lambda \sin(\Delta mt) = -\sin(2\alpha)\sin(\Delta mt). \tag{1.57}$$

In the case of measuring $\sin(2\beta)$ we saw that the decay had a contribution from a penguin diagram which entered with the same weak phase as the tree diagram.

For the decay of $B^0 \to \pi^+\pi^-$ the weak phase is different. We can define the decay amplitudes as a combination of tree and penguin terms

$$A_{\pi^+\pi^-} = Te^{i\phi_T}e^{i\delta_T} + Pe^{i\phi_P}e^{i\delta_P} \tag{1.58}$$

$$\overline{A}_{\pi^+\pi^-} = Te^{-i\phi_T}e^{i\delta_T} + Pe^{-i\phi_P}e^{i\delta_P} \tag{1.59}$$

where T, ϕ_T, and δ_T (P, ϕ_P, and δ_P) represent the magnitude, weak phase and strong phase of the tree (penguin) amplitudes. If the tree and penguin terms have different weak phases so that $\phi_T \neq \phi_P$, λ depends on differing tree and penguin parameters and no longer cleanly measures a single phase. With significant penguin *pollution*, the differing phases mean that direct *CP* violation is also possible so that $|\lambda| \neq 1$. The presence of direct *CP* violation leads to a $\cos(\Delta mt)$ term in the time dependent asymmetry whose coefficient can be measured. Direct *CP* violation does not have to be present; if the strong phases are equal so $\delta_T = \delta_P$ then λ is a pure phase and $|\lambda| = 1$. The phase does depend on the tree and penguin contributions meaning that there is a shift in the value of $\sin(2\alpha)$ extracted due to the penguin contribution. In all these cases, the value extracted is known as $\sin(2\alpha_{eff})$ where α_{eff} is known as "alpha effective".

How big an effect do the penguins have?

Of course penguins are only a problem if they make a significant contribution to the decay amplitude in $B \to \pi^+\pi^-$. While it is difficult to make accurate predictions it is possible to get some idea of how significant the contribution of penguin diagrams are from the relative branching fractions of $B \to \pi^+K^-$ and $B \to \pi^+\pi^-$.

The quantity of interest is the ratio P/T between the penguin and tree amplitudes where

$$P \equiv A(B \to \pi^+\pi^-)|_{penguin} \qquad T \equiv A(B \to \pi^+\pi^-)|_{tree} \tag{1.60}$$

and this ratio can be written as

$$\frac{P}{T} = \frac{A(B \to \pi^+K^-)|_{penguin}}{T} \frac{P}{A(B \to \pi^+K^-)|_{penguin}}. \tag{1.61}$$

To estimate P/T we must make some assumptions. Firstly we assume that the decay $B \to \pi^+ K^-$ is dominated by a $b \to sg$ gluonic penguin process, and that $B \to \pi^+ \pi^-$ is dominated by the $b \to u\bar{u}d$ tree process. Using the branching fractions from the two decays [13]

$$\mathcal{B}(B^0 \to \pi^+ \pi^-) = (4.7 \pm 0.6 \pm 0.2) \times 10^{-6} \tag{1.62}$$

$$\mathcal{B}(B^0 \to \pi^+ K^-) = (17.9 \pm 0.9 \pm 0.6) \times 10^{-6}. \tag{1.63}$$

The ratio between the two is 3.8 so

$$\left| \frac{A(B \to \pi^+ K^-)|_{penguin}}{T} \right| = \sqrt{3.8} = 1.9 \tag{1.64}$$

The second term in equation 1.61 is the ratio of the $b \to d$ and $b \to s$ penguins. This is given by

$$\left| \frac{P}{A(B^0 \to \pi^+ K^-)|_{penguin}} \right| = \left| \frac{V_{td}}{V_{ts}} \right| \times \text{SU}(3) \text{ breaking factor} \tag{1.65}$$

The $SU(3)$ breaking factor is unknown, so for the purpose of this estimation I will ignore it. Using the CKM constraint

$$0.15 \leq \left| \frac{V_{td}}{V_{ts}} \right| \leq 0.34 \tag{1.66}$$

we get an overall result of

$$0.29 \leq \left| \frac{P}{T} \right| \leq 0.65 \tag{1.67}$$

While this is probably an overestimation given that the $SU(3)$ breaking will give a value less than one, it shows that it is likely that penguins play a sizeable role in the $B \to \pi^+ \pi^-$ decay amplitude.

Extracting α in the presence of penguins

Measuring $\sin(2\alpha)$ cleanly using $B \to \pi^+ \pi^-$ requires the separation of the tree and penguin contributions. Gronau and London [14] showed that, by using isospin relations between the different $B \to \pi\pi$ modes, it is possible to extract the tree contribution to $B \to \pi^+ \pi^-$ and so measure $\sin(2\alpha)$ without ambiguity.

Isospin amplitudes can be given the label $I_{\Delta I, I_f}$ where ΔI is the change in isospin of the b-quark decay and I_f is the isospin of the final state which includes the spectator quark. A gluon is pure $I = 0$, so that the gluonic $b \to d$ penguin is pure $\Delta I = 1/2$. The tree level $b \to u\overline{u}d$ decays have both $\Delta I = 1/2$ and $\Delta I = 3/2$ components. Therefore if the $\Delta I = 3/2$ component can be isolated, then the tree contribution with the weak phase of interest can be measured.

Decay Amplitude	Isospin decomposition
$A^{+0} \equiv A(B^+ \to \pi^+\pi^0)$	$\frac{\sqrt{3}}{2}A_{3/2,2}$
$A^{+-} \equiv \frac{1}{\sqrt{2}}A(B^0 \to \pi^+\pi^-)$	$\frac{1}{\sqrt{12}}A_{3/2,2} - \sqrt{\frac{1}{6}}A_{1/2,0}$
$A^{00} \equiv A(B^0 \to \pi^0\pi^0)$	$\frac{1}{\sqrt{3}}A_{3/2,2} + \sqrt{\frac{1}{6}}A_{1/2,0}$

Table 1.1: The isospin composition at the quark level of the various $B \to \pi\pi$ decay modes.

The isospin decomposition of the amplitudes is shown in table 1.1. The three decay amplitudes depend on only two isospin amplitudes. The amplitudes of the *CP* conjugate processes are obtained from the amplitudes A by changing the sign of the CKM phases as the strong phases remain the same. The isospin decomposition gives the following relations for the amplitudes and the conjugate amplitudes

$$\frac{1}{\sqrt{2}}A^{+-} + A^{00} = A^{+0} \tag{1.68}$$

$$\frac{1}{\sqrt{2}}\overline{A}^{+-} + \overline{A}^{00} = \overline{A}^{+0} \tag{1.69}$$

where both relations form triangles in the complex plane that are shown in figure 1.5. As the penguin diagram is purely $\Delta I = 1/2$, the A^{+0} amplitude comes solely from the tree diagram, meaning that the $|A^{+0}| = |\overline{A}^{-0}|$ so the triangles have a base in common. The measurement of the time dependent decay rates for $B^0(t) \to \pi^+\pi^-$ and $\overline{B}^0(t) \to \pi^+\pi^-$ give $|A^{+-}|$ and $|\overline{A}^{+-}|$. Because of the completely neutral final state, and the lack of position resolution of π^0 mesons at *BABAR*, it is impossible to perform a time dependant analysis for $B \to \pi^0\pi^0$. It is however possible in principle to do a time independent analysis so giving $|A^{00}|$ and $|\overline{A}^{00}|$.

The rate for $B^0 \to \pi^0\pi^0$ therefore plays a crucial role in the determination of $\sin(2\alpha)$. Theoretical estimates give a branching fraction of 10^{-6} or lower which would make
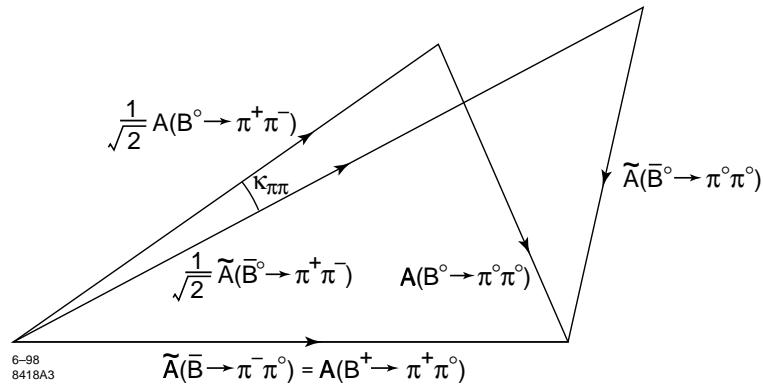
Figure 1.5: Triangles showing the isospin relation between the various $B \to \pi\pi$ decay amplitudes, and the conjugate processes.

the isospin analysis described very difficult. These estimates assume that colour suppression plays a significant role in the decay of B mesons to light mesons. There could however be long-distance rescattering effects that could enhance the branching fraction of $B^0 \to \pi^0\pi^0$ and so make the isospin analysis feasible.

In the event that the branching fraction for $B^0 \to \pi^0\pi^0$ is small, then useful information regarding $\sin(2\alpha)$ can still be extracted. Grossman and Quinn [15] showed that a bound relating α and α_{eff} is given by the relation

$$\sin^2(\alpha_{eff} - \alpha) \leq \frac{\langle \mathcal{B}(B^0 \to \pi^0\pi^0) \rangle_{CP}}{\mathcal{B}(B^+ \to \pi^+\pi^0)} \tag{1.70}$$

where $\langle \mathcal{B}(B^0 \to \pi^0\pi^0) \rangle_{CP}$ is the *CP*-averaged decay rate for $B^0 \to \pi^0\pi^0$, and $\mathcal{B}(B^+ \to \pi^+\pi^0)$ is the rate for the decay $B^+ \to \pi^+\pi^0$. In the case where $B^0 \to \pi^0\pi^0$ is very small, the difference between α_{eff} and α becomes negligible.

$B^0 \to \pi^0\pi^0$ is also expected to exhibit direct *CP* violation, with predictions ranging from $7.5 - 14\%$ [17] up to 32% [18]. As with measuring α, this measurement is difficult as flavour tagging must be used so requiring a high statistics sample of $B^0 \to \pi^0\pi^0$ decays.

Experiment	No. $B\bar{B}$	Yield	Significance	limit (10^{-6})	$\mathcal{B}(\times 10^{-6})$
BABAR	87.9×10^6	23^{+10}_{-9}	2.5	< 3.6	$1.6^{+0.7}_{-0.6}{}^{+0.6}_{-0.3}$
BELLE	31.7×10^6	12 ± 6	2.2	< 5.6	$2.2 \pm 1.5 \pm 0.6$
CLEO	9.7×10^6	$6.2^{+4.8}_{-3.7}$	2.0	< 5.7	$2.2^{+1.7}_{-1.3} \pm 0.7$

Table 1.2: The latest branching fraction results for $B^0 \to \pi^0\pi^0$.

Table 1.5.3 shows the latest branching fraction results for $B^0 \to \pi^0\pi^0$ from *BABAR* [22], BELLE [23] and CLEO [24]. All three experiments see a hint of a signal in the $\mathcal{B}(B^0 \to \pi^0\pi^0) \approx 2 \times 10^{-6}$ region. The latest results from *BABAR* for the other $B \to \pi\pi$ modes are $\mathcal{B}(B^+ \to \pi^+\pi^0) = (5.5^{+1.0}_{-0.9} \pm 0.6) \times 10^{-6}$ [25], and $\mathcal{B}(B^0 \to \pi^+\pi^-) = (4.7 \pm 0.6 \pm 0.2) \times 10^{-6}$ [13].

1.5.4   Current constraints on the CKM matrix and *CP* violation in the *B* sector

There are many constraints on the CKM description of *CP* violation both from direct measurements of the individual CKM elements and relations from indirect sources. All measurements and diagrams are taken from [16] and [19]. $|V_{ud}|$ has been measured from nuclear, neutron and pion β-decays

$$|V_{ud}| = 0.97394 \pm 0.00089 \qquad (1.71)$$

while semileptonic kaon and hyperon decays allow the measurement of $|V_{us}|$ which is the λ_W term in the Wolfenstein parameterisation of the CKM matrix

$$|V_{us}| = 0.2200 \pm 0.0025. \qquad (1.72)$$

Semileptonic B decays allow the measurement of $|V_{ub}|$

$$|V_{ub}| = (3.49 \pm 0.24_{expt} \pm 0.55_{theory}) \times 10^{-3}. \qquad (1.73)$$

Deep inelastic scattering (DIS) of neutrinos and anti-neutrinos on nucleons allow the measurement of both $|V_{cd}|$ and $|V_{cs}|$ where

$$|V_{cd}| = 0.224 \pm 0.014 \qquad (1.74)$$

and the DIS measurements are combined with those from the semileptonic D decays to give $|V_{cs}|$

$$|V_{cs}| = 0.969 \pm 0.058. \qquad (1.75)$$

The *A* term of the Wolfenstein parameterisation is given by $|V_{cb}|$ which can be determined from exclusive and inclusive semileptonic *B* decays to charm final states. The mean from these results is

$$|V_{cb}| = (40.76 \pm 0.50_{expt} \pm 2.00_{theory}) \times 10^{-3}. \tag{1.76}$$

The accuracy of the measurements for the top mixings, $|V_{ti}|$, is not as good as the other elements although it is still possible to provide constraints using the unitary nature of the CKM matrix. From the ratio of the production cross section of bottom quarks to the total top decay width, $|V_{tb}|$ can be constrained

$$|V_{tb}| = 0.99 \pm 0.15. \tag{1.77}$$
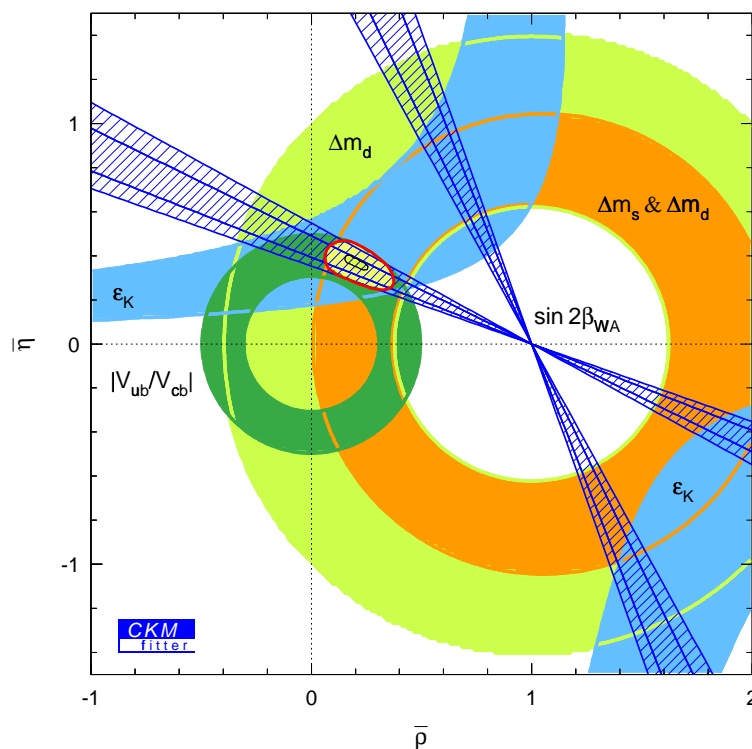
Figure 1.6: The $(\overline{\rho}, \overline{\eta})$ plane showing the allowed region for the apex of the unitarity triangle. The various coloured regions show the constraints applied by different measurements, where the latest measurements of $\sin(2\beta)$ provide the strongest constraint. The plot was generated using [19]

There are several other measurements that provide constraints on the values of $(\overline{\rho}, \overline{\eta})$, the apex of the unitarity triangle. Measuring ϵ_K from K^0 mixing provides a

constraint on the apex, as does Δm_{B_d} from B_d mixing. Limits on the B_s mixing frequency, combined with the values of Δm_{B_d} provide further constraints. The latest combined constraints can be seen in figure 1.6.

In the past year, both the *BABAR* and *Belle* experiments have measured non-zero values for the *CP* violating asymmetry $\sin(2\beta)$. The accuracy of the latest results from the two experiments [20] [21] are providing the greatest constraint on the values of $(\overline{\rho}, \overline{\eta})$ as can clearly be seen in figure 1.6.

With both experiments expecting to further reduce the error on the value of $\sin(2\beta)$ in the coming years, and the possible additon of further constraints by the measurement of $\sin(2\alpha)$ through the $B \rightarrow \pi\pi$ modes, this is a particularly exciting time for *CP* violation physics in the B meson sector.

Chapter 2

The BaBar experiment and the PEP-II storage ring

2.1   Introduction

The primary physics goal of the *BABAR* experiment is the systematic study of CP-violating asymmetries in the decay of neutral B mesons to CP eigenstates. Secondary goals are precision measurements of bottom and charm mesons, and the search for rare processes. The branching fractions for such processes are in the region of 10^{-4} or lower, so requiring very high integrated luminosities. Such physics goals also require the precise measurement of the separation of the two B meson decays, which is best achieved through a boost to the $\Upsilon(4S)$ system and the use of precision vertexing. High quality tracking, calorimetry and particle identification also play a crucial role in extracting the full physics potential.

All of these elements are provided by the *BABAR* detector operating at the PEP-II storage ring. In this chapter I will discuss the key components and performance of the *BABAR* detector, but will begin with an overview of the PEP-II storage ring, its design, performance and impact on the *BABAR* detector. A more detailed description of PEP-II and *BABAR* can be found in [26], [27] and [28].

2.2 The PEP-II Storage Ring
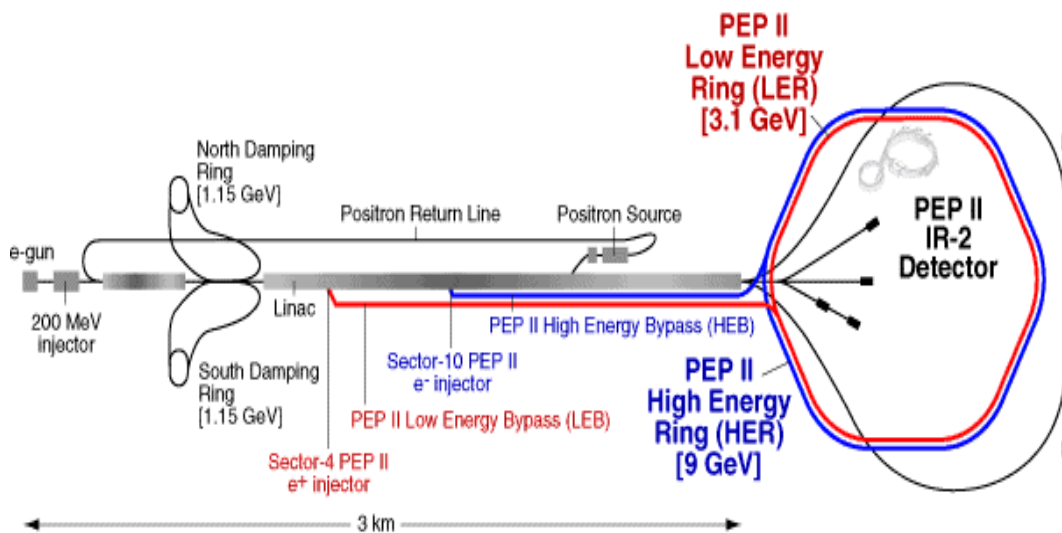
Figure 2.1: Overview of the SLAC linac used to inject electrons and positrons into the PEP-II storage rings.

PEP-II is an e^+e^- storage ring designed to operate at a center of mass (CM) energy of 10.58 GeV, corresponding to the mass of the $\Upsilon(4S)$ resonance. 9 GeV electrons are stored in the high energy ring (HER) and are collided with 3.1 GeV positrons which are stored in the low energy ring (LER). The overall design of the PEP-II system and the SLAC linac that injects into the two rings is shown in figure 2.1. The asymmetric energies provide a boost of $\beta\gamma = 0.55$ to the $\Upsilon(4S)$ system. While at least 96% of $\Upsilon(4S)$ decays are to a $B\overline{B}$ pair [6], there are considerable background rates from lighter quark "continuum" production. The ratio of $\Upsilon(4S)$ to $q\overline{q}$ production is approximately 1:3, with a cross section for $B\overline{B}$ production of around 1.1 nb. To produce the tens of millions of B mesons required means that PEP-II is a very high luminosity machine. Table 2.1 shows the key PEP-II parameters for design, regular running and the best values achieved up to the end of July 2002.

PEP-II has been an enormous success, surpassing design expectations for both instantaneous and integrated luminosity. These have been achieved without a high numbers of bunches, optimal injection from the SLAC linac, or maximum currents in the two rings, giving great optimism that even better performance is possible.

Parameters	Design	Typical	Best achieved
Energy HER (GeV)	9.0	9.0	9.0
Energy LER (GeV)	3.1	3.1	3.1
Current HER (A)	0.75	0.95	1.05
Current LER (A)	2.15	1.7	2.14
# bunches	1658	553-829	1658
bunch spacing (ns)	4.2	8.4	4.2
σ_{L_x} (μm)	110	120	45
σ_{L_y} (μm)	3.3	5.6	3.0
σ_{L_z} (mm)	9	9	9
Fill time (min)	6	10	8
Top off time (min)	3	3	2
Luminosity (10^{33} cm^{-2}s^{-1})	3	4.0	4.6
Luminosity (pb/day)	135	225	309

Table 2.1: Parameters of the PEP-II machine.

2.2.1   The Interaction Region

Producing high luminosities requires both high beam currents and a large number
of bunches in PEP-II. These factors play a major role in the design of the interac-
tion region which is shown in figure 2.2. The bunches are collided head-on and to
avoid secondary interactions the bunches in each ring must be focussed and brought
together close to the interaction point (IP) and separated immediately after. This
is done by a pair of dipole magnets (B1) followed by a series of focussing quadropole
magnets. The B1 magnets are at $\pm$ 21cm of the IP, while the Q1 quadropoles are
permanent magnets placed within the *BABAR* solenoid. The quadropoles Q2, Q4 and
Q5 are standard iron magnets and are located outside of the solenoid's field. The
interaction region is enclosed by a water cooled beam pipe of 27.9 mm outer radius.
The beam pipe, permanent magnets and the silicon vertex tracker are enclosed in a
4.5m long support tube which spans the interaction region.

2.2.2   Machine-related Backgrounds

There are several potential sources of machine-related backgrounds. These back-
grounds cause high occupancy in the various detector subsystems which cause a
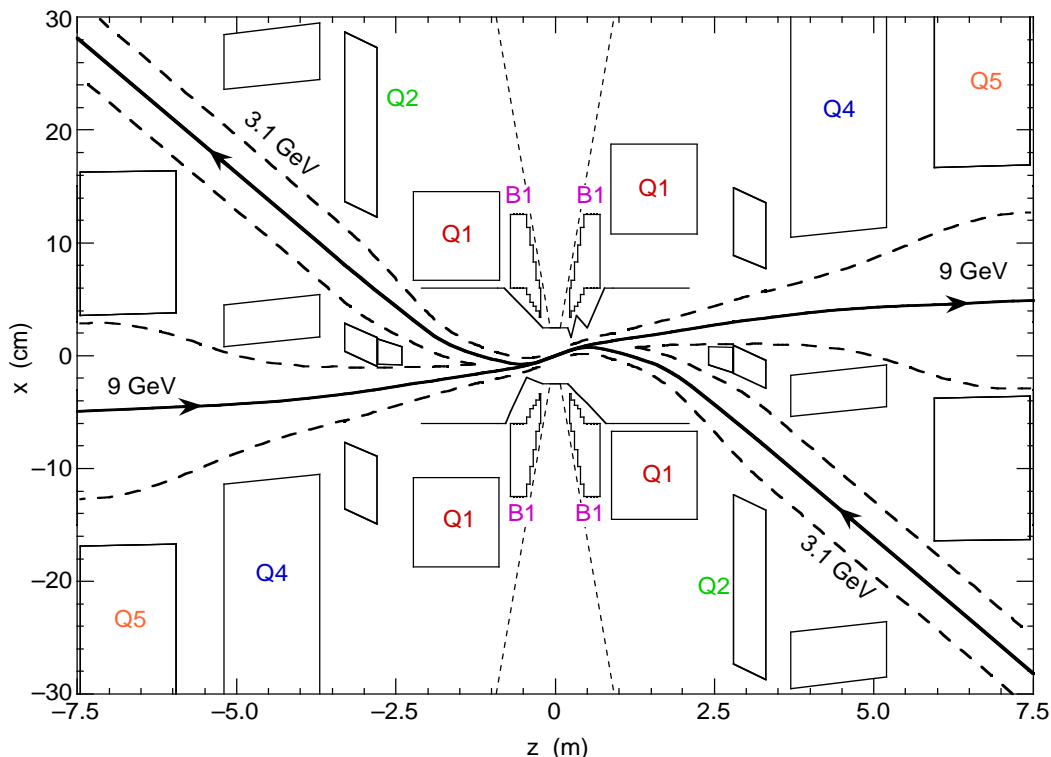
Figure 2.2: Plan view of the interaction region (the vertical scale is highly exaggerated). Focusing quadrupoles are labelled Q1-Q5 and separation dipoles B1.

degradation in performance. Over time significant radiation damage can be accumulated which can permanently effect performance and ultimately may cause failure.

The design of the interaction region to bring the differing beam energies into and out of collision generates many kW of synchrotron radiation which represents the greatest background concern. The design of various components of the interaction region has been modified so that most of the synchrotron photons are channelled and absorbed away from the detector acceptance. There are however x-rays generated at the HER quardropoles that enter the detector. So far during running these backgrounds do not seem to create a significant problem.

Interactions between the beam and residual gas molecules cause scattering of the beam into the detector acceptance. Such sources of background are limited by having an excellent vacuum in the beam pipe region which is the case during standard running. These interactions become important when the gas pressures within the

machine are high, which occurs when the vacuum has been compromised. This typically occurs at the beginning of operations after a prolonged repair period.

It is also possible for radiative Bhabha scattering to cause electrons or positrons to hit material a few metres from the IP causing electromagnetic showers that go into the *BABAR* detector. While this background was not initially considered a problem, it scales with luminosity and it is likely that as upgrades take place and PEP-II delivers higher beam currents so this will be a more significant component.

Beam losses during injection can also contribute significantly to the background radiation seen by *BABAR*. So far during the life of *BABAR* the background levels have remained within design expectations and there have been no significant degradation in performance of the detector components due to these backgrounds.

2.2.3   Performance

The performance of PEP-II has surpassed nearly all design expectations. Peak luminosity is considerably higher than initially expected and the machine's reliability has allowed luminosity to be integrated far above the design goals. Figure 2.3 shows the delivered and recorded luminosity from PEP-II over the course of its running lifetime. Almost 100fb^{-1} of data have been recorded over the past 3 years with ever increasing integration rates. This corresponds to approximately 100 million $B\overline{B}$ events. Currently there are plans to further upgrade PEP-II giving a peak luminosity of $1\times10^{34}\text{cm}^{-2}\text{s}^{-1}$ by the end of 2003 and $4\times10^{34}\text{cm}^{-2}\text{s}^{-1}$ by the end of 2006, which is over 10 times design luminosity.

2.3   The *BABAR* Detector

The *BABAR* detector was designed to maximise the physics potential of PEP-II. To do this with the boosted $\Upsilon(4S)$ decays produced by PEP-II, the detector is offset relative to the IP by 0.37m and the detector is of an asymmetric design to give the
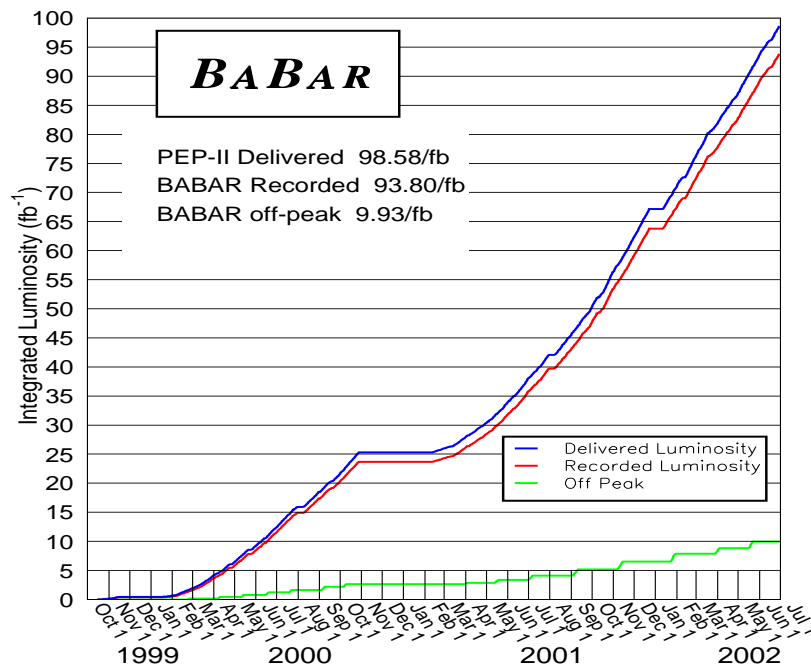
Figure 2.3: Integrated luminosity delivered by PEP-II and recorded by *BABAR*.

maximum possible acceptance in the CM system. The inner detector consists of a silicon vertex tracker, a drift chamber, a ring-imaging Cherenkov detector and a CsI calorimeter. These inner components are housed in a superconducting solenoid providing a uniform magnetic field of 1.5T. The steel flux return is instrumented for muon and neutral hadron identification. Figure 2.4 shows a longitudinal section through the detector highlighting the various sub-detectors. In the following sections I will discuss the physics goals, design and performance of the detector's principal components. Special attention will be given to the calorimeter, as its performance and design are of particular interest for the following chapters.

Before starting the description of the sub-detectors it is important to define the *BABAR* co-ordinate system. A right handed co-ordinate system is employed with the z-axis in the direction of the high energy beam. The y-axis points vertically up, and the x-axis points horizontally, away from the center of the $PEP-II$ ring. The polar (θ) and azimuthal (ϕ) angles are defined as in the standard spherical polar co-ordinate system.
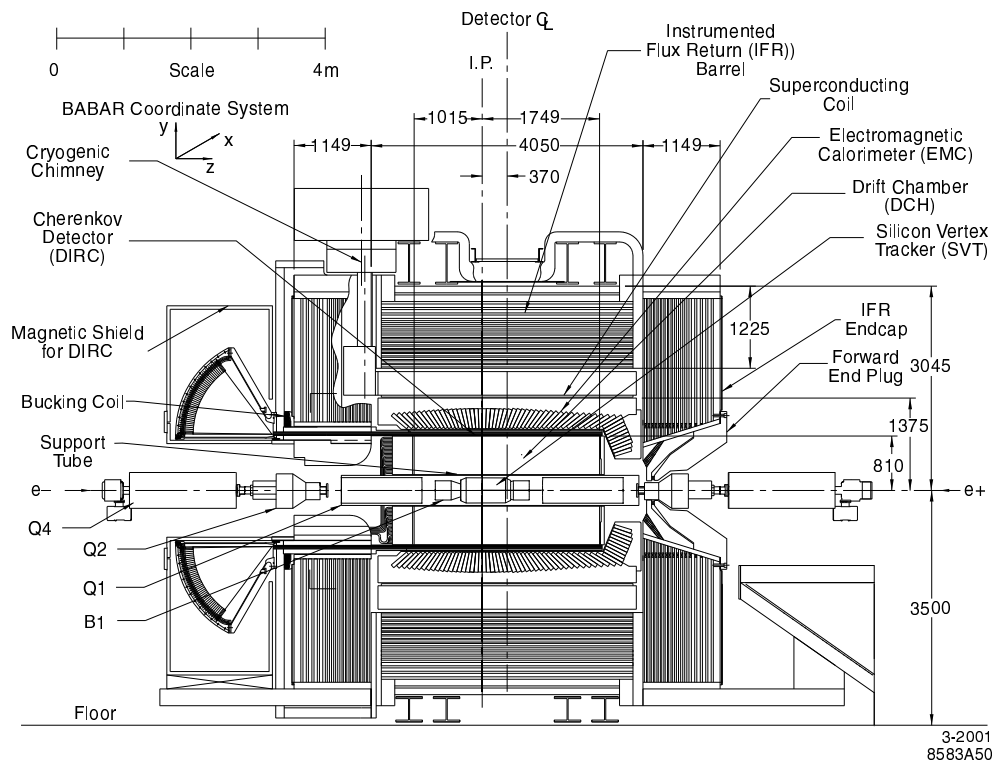
Figure 2.4: A longtitudinal section of the *BABAR* detector longtitudinal section.

2.4   The Silicon Vertex Tracker (SVT)

2.4.1   SVT Physics Requirements

The SVT has been designed to provide precise reconstruction of charged particle trajectories and decay vertices near the interaction region. The SVT is therefore critical for the measurement of time-dependent CP asymmetries. Measuring time dependent CP asymmetries requires the distance between the two B decay vertices to be known to an accuracy of better than 135 μm in the z direction. This value corresponds to half the mean distance between the two B meson vertices, and requires an accuracy of better than 80 μm for each vertex. The requirements in the $x - y$ plane arise from the need to reconstruct τ and charm decays as well as B decays. In decays of the type $B \to D^+ D^-$, separating the two D's is important. The distance between the two D's in the $x - y$ plane for this decay is typically around $275\mu m$, which means the SVT needs to provide resolution of the order $100\mu m$ in the plane

perpendicular to the beam line.

The SVT also provides the only tracking for particles with transverse momentum less than $120\,\mathrm{MeV}/c$, the minimum that can accurately be measured in the drift chamber. This feature is fundamental for the detection of slow pions from D^* decays where a tracking efficiency in excess of 70% is required for tracks with transverse momentum in the range $50-120\,\mathrm{MeV}/c$. Beyond the tracking capability, the SVT also provides the best information regarding track angles, which are crucial for the resolution of the Cherenkov angle for particle identification of tracks with high momentum.

2.4.2   SVT Design

The SVT consists of five layers of double-sided silicon strip sensors, organized in 6, 6, 6, 16 and 18 modules respectively. The strips on the opposite sides of each sensor are orientated orthogonally to each other: the ϕ-measuring strips run parallel to the beam and the z-measuring strips are orientated transversely to the beam axis. The modules of the inner three layers are straight while the outer two layers are arch shaped in the z-R plane so to minimize the amount of silicon required to cover the solid angle. Figure 2.5 shows the layer structure while figure 2.6 shows a schematic of the longtitudinal section highlighting the arch shape of the outer layers.

To aid coverage and alignment, the inner modules are tilted slightly giving overlap between adjacent modules. The outer modules cannot be tilted because of the arch geometry. To avoid gaps and to have suitable overlap in the ϕ coordinate, layers 4 and 5 are divided into two sub-layers (4a, 4b, 5a, 5b) and placed at slightly different radii as shown in figure 2.5.

In all, the *BABAR* SVT has a total active silicon area of $0.96\,\mathrm{m}^2$, consisting of 340 silicon detectors and a total of 150,000 readout channels. The geometrical acceptance is 90% of the solid angle in the CM system.
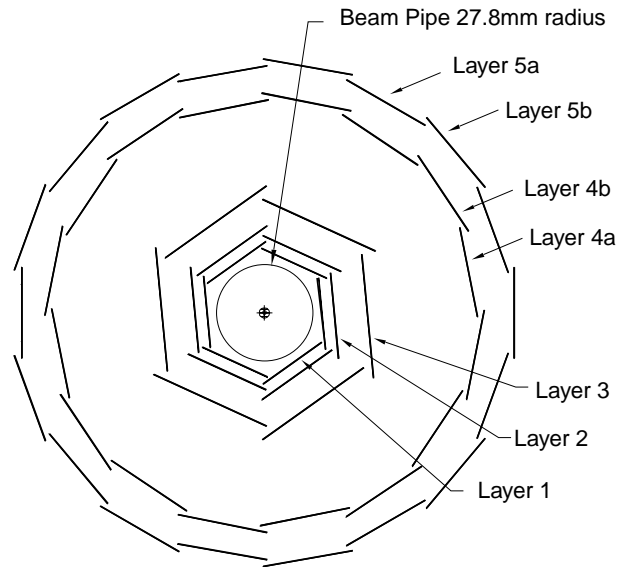
Figure 2.5: Schematic view of SVT: transverse section showing the five layer structure.
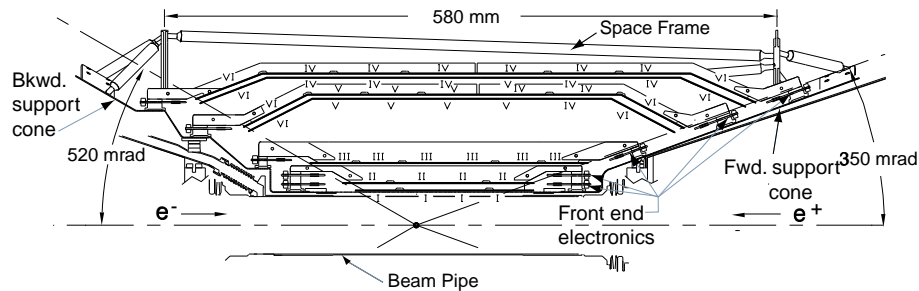
Figure 2.6: Schematic view of SVT: longitudinal section showing the five layers and the arched structure of the outer two layers.

2.4.3 SVT Readout and Reconstruction

Each of the modules is divided electrically into two half modules which are read out at each end. The ϕ strips of sensors in the same half module are electrically connected to form a single readout strip. The signals from the z strips are brought to the readout electronics using fanout circuits. To minimize the material in the acceptance region, the readout electronics are mounted entirely outside the active detector volume.

The signals from the strips are shaped and amplified before being compared to

a threshold which is determined from background conditions during running. A custom made radiation-hard chip is used to perform a time-over-threshold (TOT) measurement of the total deposited charge in a strip. The TOT is approximately logarithmic in response so allowing a large dynamic range to be covered.

SVT clusters are formed by grouping adjacent strips which have consistent timing information. Clusters separated by one strip can be merged together, following which the single clusters and merged clusters are passed to a pattern recognition algorithm which then interprets the data. Hit positions within the SVT are expressed in terms of the physical position of the silicon sensors.

2.4.4   SVT Performance

The resolutions for the five layers of the SVT are shown for z in figure 2.7 and for ϕ in figure 2.8. A resolution of between $10 - 40\mu m$ in ϕ and $15 - 40\mu m$ in z can be obtained in Layer 1. Both the ϕ and z resolutions are in excellent agreement with Monte Carlo expectations.

The internal alignment of the SVT modules, and the alignment of the SVT as a whole with the rest of the detector are of crucial importance to the position and resolution performance of the detector. The SVT is calibrated for both types of alignment through the use of two-prong events where the high energy tracks give the best possible position information.

The radiation limit for the SVT over its lifetime was expected to be 2 Mrad, and to date the accumulated dose is approaching this limit with the horizontal plane receiving the greatest dose. Recent studies have shown that the lifetime of the detector should in fact be 5 Mrad. As the luminosity increases in the coming years the radiation dose may be exceeded. Consequently a replacement for the SVT is currently being built and will be installed in 2004.
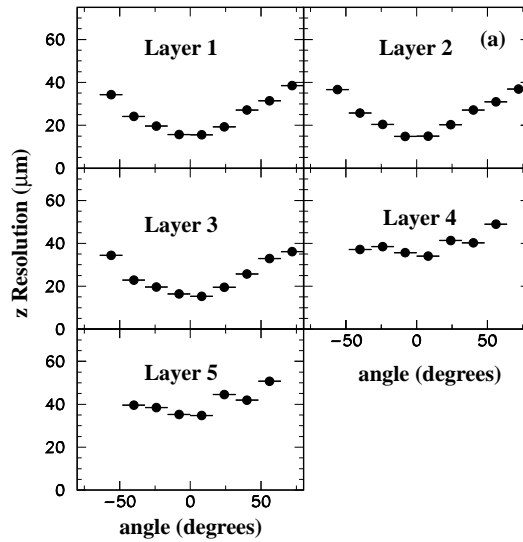
Figure 2.7: z resolution for the five layers of the SVT as a function of incident track angle.
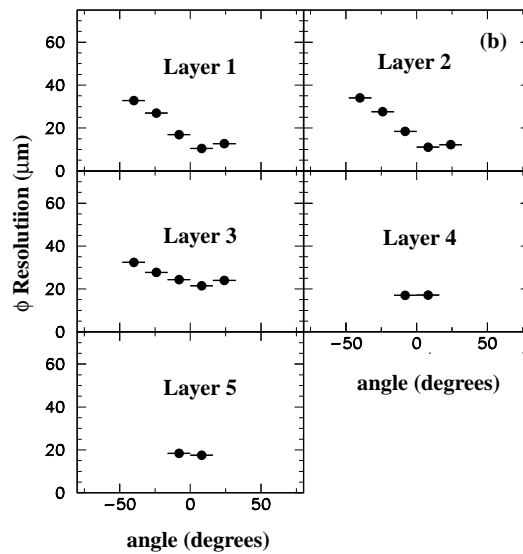
Figure 2.8: ϕ resolution for the five layers of the SVT as a function of incident track angle.

2.5   The Drift Chamber (DCH)

2.5.1   DCH Physics Requirements

The DCH is the principal detector of charged particles at *BABAR*. It is required to provide precise measurements of momenta and track angles with high precision for

all tracks with momentum above 120 MeV/c, and within a transverse momentum range of $0.1 < p_T < 5.0$ GeV/c so enabling the exclusive reconstruction of B and D meson decays. The DCH is key to extrapolation of charged tracks to the DIRC, EMC and IFR. The DCH provides dE/dx measurments for the tracks, allowing particle identification of the tracks, particularly for low momentum tracks with $p < 700$ MeV/c where the DIRC is not effective. The DCH also provides all the information for the reconstruction of K_S^0. The DCH must also provide tracking and timing information to the *BABAR* trigger.

2.5.2   DCH Design

The DCH is a 2.8m long cylinder surrounding the IP as shown in figure 2.9 and is shifted to give greater coverage in the forward region. The inner radius of the detector is 23.6 cm and the outer radius is 80.9 cm. The DCH contains 40 layers of small hexagonal cells giving spatial and ionization loss measurements for the charged tracks. The chamber is filled with a 4:1 mixture of helium:isobutane; this low mass gas mixture helps keep multiple scattering to a minimum.
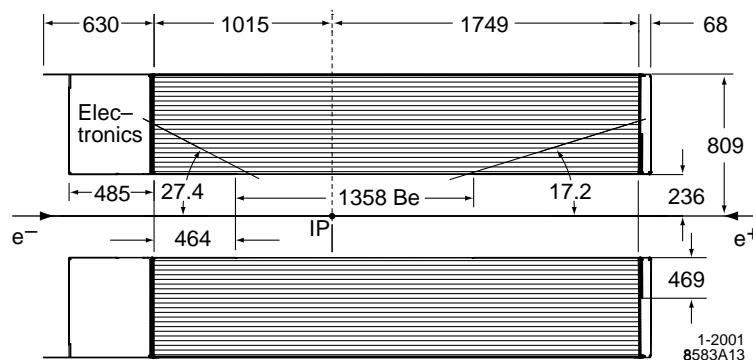
Figure 2.9: DCH longitudinal section. The dimensions are in mm.

The endplates of the chamber are made from aluminium, the backward plate being 24mm thick and the forward being 12mm so to reduce material in front of the calorimeter endcap. Figure 2.10 shows the design of the drift cells for the four innermost superlayers. The sense wires are gold plated tungsten-rhenium and $20\mu m$ in diameter. The field wires are gold plated aluminium with diameters of $120\mu m$

and $80\mu m$. The hexagonal drift cells have a typical size of $1.2 \times 1.8 cm^2$. A nominal running voltage of $+1960V$ is applied to the sense wires.
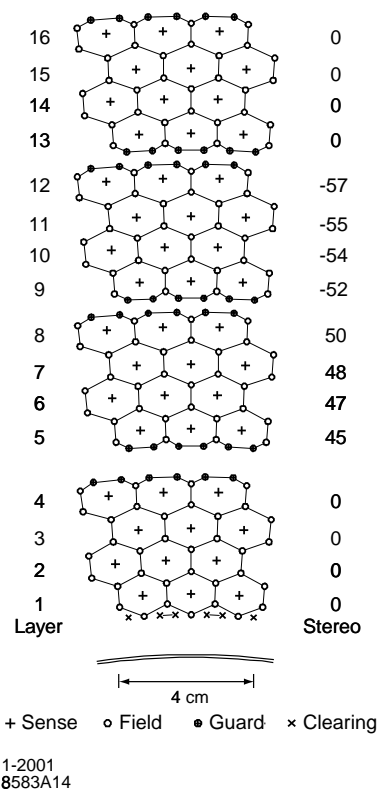
Figure 2.10: DCH cell layout for the first four superlayers. The stereo angle of the layers in mrad is shown in the right hand column.

The 40 layers within the chamber are grouped by 4 into 10 superlayers. The stereo angles of the superlayers alternate between axial (A) and positive and negative stereo angle layers (U,V) and are in the order AUVAUVAUVA. The stereo angles vary between ±45 mrad in the innermost layers, to ±76 mrad in the outermost layers. The superlayer structure is beneficial to the fast local segment finding needed by the Level 1 trigger.

2.5.3   DCH Readout and Reconstruction

The DCH electronics readout provides a measurement of the drift time and the integrated charge. The electronics used for amplification, digitization and trigger interface are housed outside of the detector fiducial volume within 48 aluminium

boxes mounted on the rear end plate of the detector. The drift time is extracted using a TDC from the leading edge of the amplified signal produced from the drifting electrons arriving at the sense wire. The TDC has a precision of 1 ns. The total charge deposited in a cell is measured using a 15 MHz Flash ADC. The data are read out using optical fibre links and are sent for further processing using 4 standard *BABAR* ROM's [30].

Charged tracks are defined by five parameters (d_0, ϕ_0, ω, z_0 and $\tan \lambda$) and are measured at the point of closest approach to the z axis. d_0 and z_0 are the distances of this point from the origin in the $x - y$ plane and the z axis. ϕ_0 is the azimuthal angle of the track, $\omega = 1/p_T$ is the curvature and λ is the dip angle relative to the transverse plane. Values of dE/dx for the charged tracks are derived from the measurements obtained from the sum of pulse heights from each drift cell after calibration corrections have been applied.

2.5.4   DCH Performance

Figure 2.11 shows the track reconstruction efficiency as determined from multi-hadron events where the tracks seen in the SVT are also seen in the DCH. The first plot shows the efficiency as a function of p_T where we can see the efficiency falling off below 250 MeV/c. The lower plot shows the efficiency as a function of polar angle. The plots also show the fall in efficiency when a voltage of 1900V was used during part of Run 1. The overall tracking efficiency is $(98 \pm 1)\%$ for tracks with momentum greater than 200 MeV/c.

Figure 2.12 shows the dE/dx as a function of momentum. The Bethe-Bloch predictions for different particle types are overlayed. Good K/π separation is achieved up to 0.6 GeV/c. The dE/dx resolution for electrons is 7.5% which is very close to the 7.0% estimated during the design process.

Figure 2.13 shows the transverse momentum resolution determined from cosmic ray muons. The data are well described by a function of the form

$$\sigma_{p_t}/p_t = (0.13 \pm 0.01)\% \cdot p_t + (0.45 \pm 0.03)\% \tag{2.1}$$
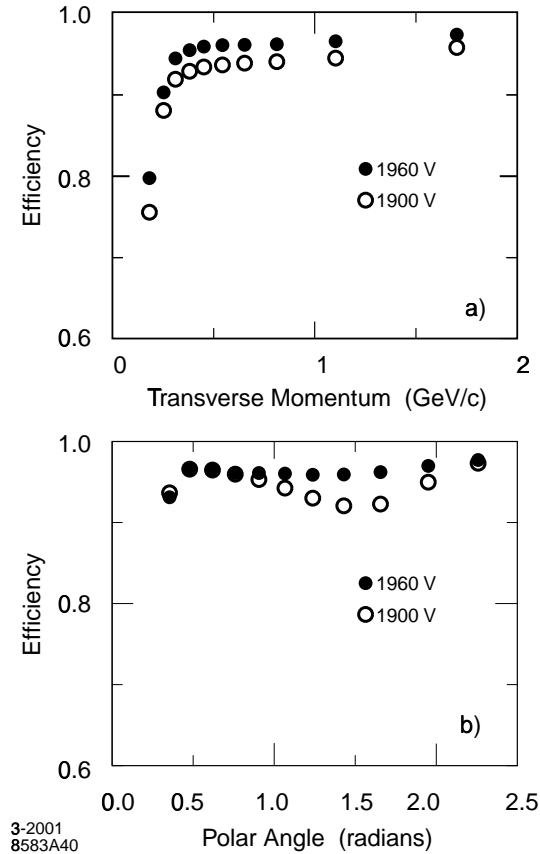
Figure 2.11: Tracking efficiency for the DCH shown as a function of transverse momentum (top) and polar angle (bottom). The plot shows the difference between using a nominal Run 1 voltage of 1960V and a lower voltage of 1900V.

where p_t is in units of GeV/c. These values are in good agreement with design estimates and can be reproduced in Monte Carlo studies.

2.6   The Detector of Internally Reflected Cherenkov radiation (DIRC)

2.6.1   DIRC Physics Requirements

One of the key components of the study of CP violation is the ability to tag the flavour of one of the B mesons. One of the best indicators of the flavour comes from identifying kaons produced in the cascade decay $b \rightarrow c \rightarrow s$. The kaons produced have a momentum of below 2 GeV/c, with most below 1 GeV/c. In addition, for
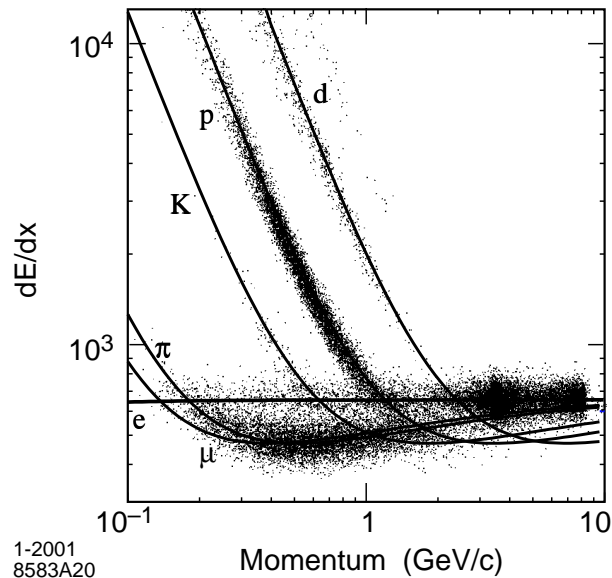
Figure 2.12: DCH dE/dx distribution for data as a function of track
momentum. The expected Bethe-Bloch distributions for $e^{\pm}, \mu^{\pm}, \pi^{\pm}$, and
$K^{\pm}$,p and d are overlayed. The dE/dx units are given by keV/m.

the measurement of $\sin(2\alpha)$ discussed in section 1.5.3, it is necessary to separate
pions from kaons in the momentum range $1.7 - 4.2$ GeV/c. It is therefore a necessity
to have good particle identfication for charged particles across a broad momentum
range.

The DIRC is a ring imaging Cherenkov detector that is designed to provide greater
than 4σ π/K separation in the momentum range 0.7 - 4.2 GeV/c. The DIRC must
also be thin in terms of radiation lengths so as to minimize the impact on the EMC
energy resolution. It should also be small in the radial direction so as to minimize
the size and therefore cost of the EMC.

2.6.2   DIRC Design

The DIRC design provides a novel solution to the particle identification requirements
at *BABAR*. The overall design is given in figure 2.14. A charged particle with $\beta = v/c$
where v is the velocity of the particle and c is the speed of light in a vacuum, leaves
the DCH and enters the DIRC. It passes through a fused silica (quartz) bar having
a refractive index $n = 1.473$. If $\beta \geq 1/n$ then Cherenkov light is produced and a

1-2001
8583A23
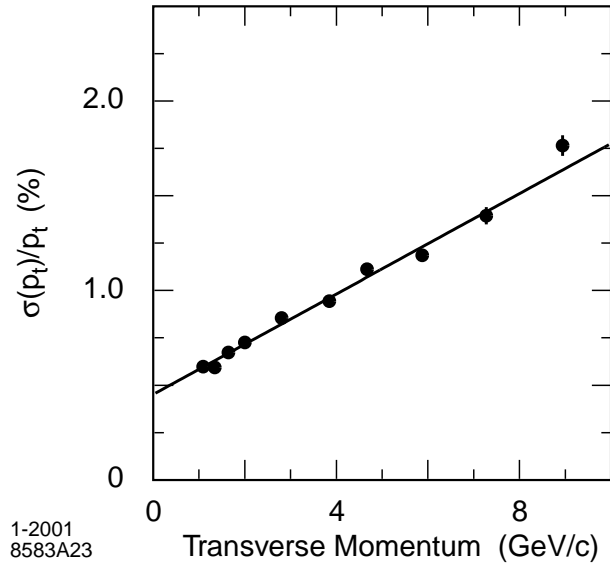
Figure 2.13: The transverse momentum resolution for DCH tracks from data. The overlayed function is a fit to the data as given in equation 2.1.

cone of photons are given off at an angle θ_c where $\cos(\theta_c) = 1/n\beta$.

Depending on the particle incident angle, the photons travel to one of the two ends of the bars. To avoid instrumenting both ends, a mirror is placed at the forward end to reflect the photons towards the backward instrumented end. This helps create space for other sub-detectors in the forward region and reduces the background levels seen by the DIRC photo multiplier tubes (PMT) that make up the DIRC instrumentation. Arriving at the instrumented end the photons pass into a purified water-filled expansion region called the standoff box. The photons are detected by an array of PMT's sitting 1.2 metres away from the quartz bar end.

The DIRC bars are arranged into 12 bar boxes forming a 12 sided polygon. Each bar box contains 12 of the 144 bars making up the DIRC. The bars are 17mm thick, 35mm wide and 4.9m long and consist of four 1.225m pieces which are glued together. The standoff box is made of stainless steel and consists of a cone, cylinder and 12 separate sectors of PMTs. It contains 6,000 litres of purified water which was chosen as it is inexpensive and has a refractive index ($n \approx 1.346$) which is close to that of the quartz bars. A steel shield and a bucking coil surround the standoff box to reduce the magnetic field in the PMT region to below 1 Gauss.
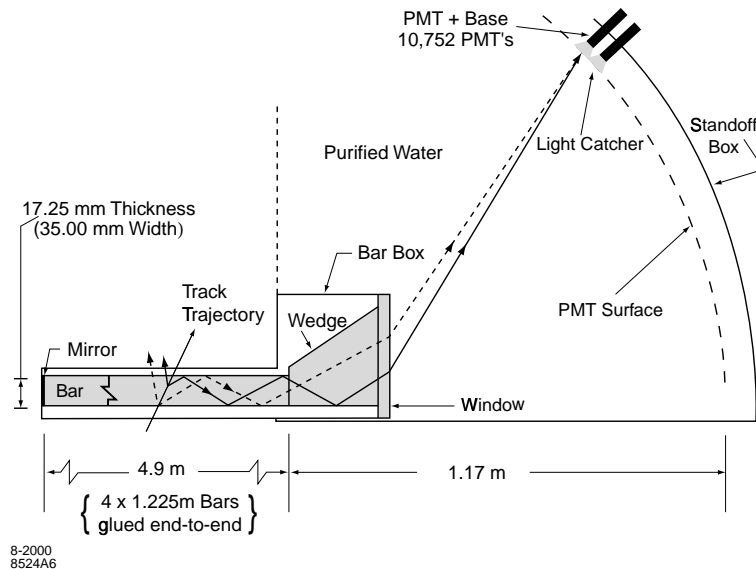
Figure 2.14: DIRC structure and concept. Incident tracks emit Cherenkov photons as they pass through the quartz bars. The photons undergo total internal reflection before passing into the water-filled standoff box and being detected by a PMT array.

Each of the 12 PMT sectors contain 896 PMT's with a 29mm diameter which are closely packed within the water volume. An hexagonal light catcher cone is mounted in front of the photocathode of each PMT giving a total active surface area of approximately 90%. In total the DIRC takes up 8 cm of radial space and a total of approximately 17% of a radiation length. The quartz bars cover a solid angle corresponding to 94% of the azimuth and 83% of the CM polar angle cosine.

2.6.3   DIRC Readout and Reconstruction

The DIRC front-end electronics are designed to measure the arrival of each Cherenkov photon observed by the PMTs. The accuracy of the observed signals is limited by the 1.5ns transit time spread of the PMTs. Each of the 168 Front-end Boards (DFBs) processes 64 PMT inputs and contain 8 custom analogue chips, 4 TDCs and one 8-bit flash ADC. The PMT signals are amplified and pulse shaped. The TDCs have 16 channels with 0.5ns binning and selective readout of the data in time with trigger. The L1 maximum trigger latency of $12\mu s$ and jitter of $1\mu s$ means that the selective readout process extracts data in time with the trigger and has a programmable

window width between 64ns and $2\mu s$. 12 DIRC crate controllers form the interface to the VME front end and are connected to 6 ROMs via 1.2 Gbit/s optical fibres. The data are processed within the ROM by a feature extraction algorithm which reduces the data by roughly 50% under normal background conditions.
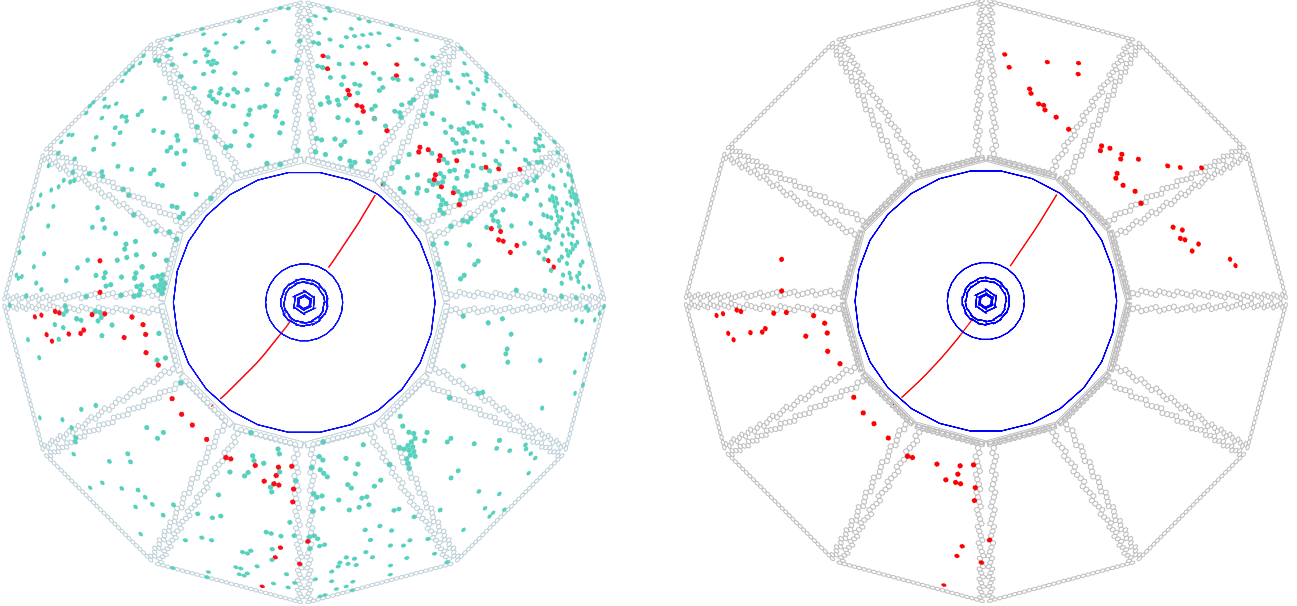
Figure 2.15: The left hand figure shows the DIRC PMT hits from an event containing two muons. The right hand figure shows the PMT hits that arrive within $\pm 8ns$ of the expected time of arrival of the two muon tracks derived from the DCH.

An unbinned maximum likelihood method is used to incorporate all available information into the space and time measurements provided by the DIRC. The emission angle and the arrival time of the Cherenkov photons are reconstructed from the observed space-time coordinates of the PMT signals. The timing measurements are used to suppress background hits and to separate photons produced by different tracks. The effect of the suppression is shown in figure 2.15. The reconstruction routine provides a likelihood for each of the five stable particle types (e, μ, π, K, p) for each track passing through the DIRC. If enough photons are found, a fit to the Cherenkov angle θ_C is also calculated for each track.
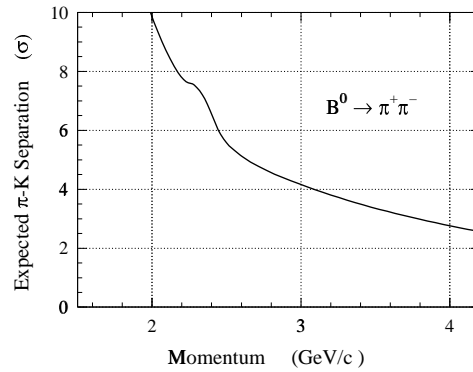
Figure 2.16: Figure showing the pion/kaon separation across the momentum spectrum used for separating two body decays to $B^0 \to \pi^+ K^-$, $B^0 \to \pi^+ \pi^-$.

2.6.4   DIRC Performance

The DIRC has performed remarkably well during the lifetime of *BABAR*. Figure 2.16 shows the K/π separation achievable for tracks coming from the decay $B^0 \to \pi^\pm K^\mp$ with greater than 3σ separation for all but the highest momentum tracks. The effect of this on the ability to perform physics is shown in figure 2.17 where the invariant $K\pi$ mass is shown with and without the DIRC being used for kaon identification. The D^0 mass peak shows using the DIRC greatly reduces the combinatoric background while not significantly effecting the signal.
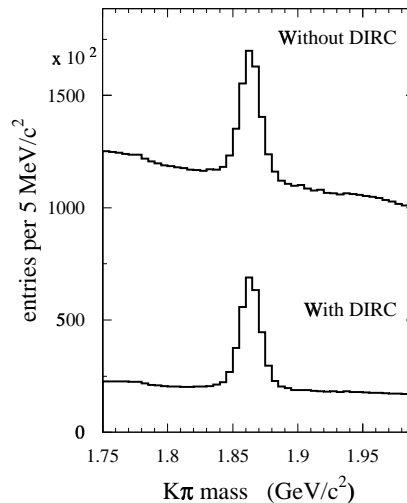
Figure 2.17: The invariant $\pi^\pm K^\mp$ mass spectra with and without using the DIRC for $K^\pm$ identfication.

2.7   The ElectroMagnetic Calorimeter (EMC)

2.7.1   EMC physics requirements

The EMC is designed to measure electromagnetic showers with high efficiency and excellent energy and angular resolution over an energy range of 20 MeV to 9 GeV. This allows the reconstruction of π^0 and η decays to photons, and the detection of photons from electromagnetic and radiative processes. The EMC also plays the key role in identifying electrons which contribute significantly to *CP* violation measurements through *B* meson flavour determination and through the reconstruction of the J/ψ.

The upper bound on the energy range comes from the need to reconstruct QED processes such as Bhabha and radiative Bhabha scattering, which are used for luminosity and energy calibrations. The lower energy limit is from the need to fully reconstruct decays of *B* and *D* mesons containing several π^0's and η's. High reconstruction efficiency is needed so that very rare processes such as the decay $B \rightarrow \pi^0 \pi^0$ can be efficiently reconstructed. This decay also requires an energy resolution $\mathcal{O}(1\%)$ for the decay to be effectively separated from backgrounds.

2.7.2   EMC Design

The EMC is designed to be a total absorption calorimeter and is composed of a finely segmented array of thallium-doped cesium iodide (CsI(Tl)) crystals. The properties of CsI(Tl) are shown in table 2.2. CsI(Tl) was chosen as the scintillating material because of its high light yield and small Moliere radius which allows for excellent energy and angular resolution. Additionally the short radiation length and the energy range at *BABAR* allows for a compact design.

The EMC consists of 6580 crystals arranged in a barrel and forward endcap. Figure 2.18 shows a longitudinal cross sectional view of the detector layout. It has full coverage in the azimuthal angle and extends from 15.8^o to 141.8^o corresponding

Parameter	Value
Radiation Length (cm)	1.85
Moliere Radius (cm)	3.8
Density (g/cm^3)	4.53
Light Yield ($\gamma/$ MeV)	50,000
Peak Emission λ_{max} (nm)	565
Refractive Index (λ_{max})	1.80
Signal Decay Time (ns)	680(64%), 3340(36%)
Radiation hardness (rad)	$10^3 - 10^4$

Table 2.2: The properties of CsI(Tl).
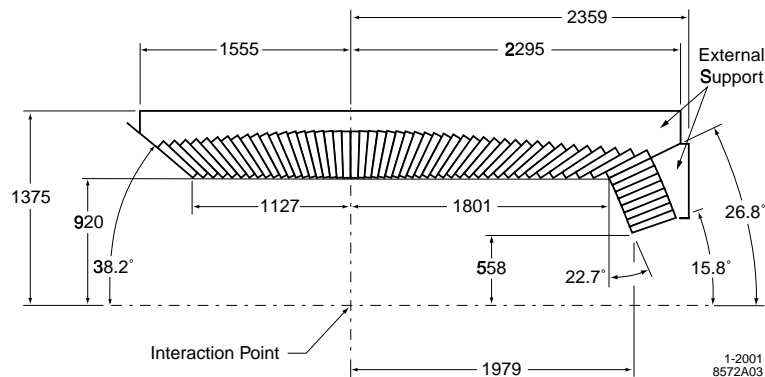
Figure 2.18: A longitudinal cross section of the top half of the EMC. The detector is axially symmetric around the z-axis. All dimensions are in mm.

to 90% of the solid angle in the CM system. The barrel contains 5,760 crystals arranged in 48 rings of 120 crystals each. The endcap has 820 crystals arranged in 8 rings. The length of the crystals increases from 29.6cm ($16X_0$) in the backward to 32.4cm ($17.5X_0$) in the forward direction to limit shower leakage from higher energy particles. To limit the possibility of pre-showering, the crystals are supported at the outer radius. The barrel and outer rings of the endcap have less than $0.3 - 0.6X_0$ of material in front of them. The inner three rings of the endcap have the SVT support structure and electronics, and B1 magnets shadowing them which gives up to $3.0X_0$ of material for these rings.

A schematic of the crystal set up is shown in figure 2.19. The crystals act as a total-absorption scintillating material, but also as a light guide to collect light at the photodiodes mounted at the rear surface. At the polished crystal surfaces light is reflected and a small amount transmitted. The crystals are covered with two
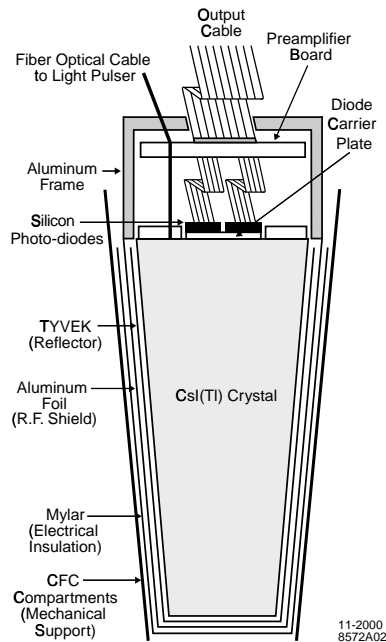
Figure 2.19: EMC crystal layout, showing crystal lining, photo-diodes and electronics layout.

layers of white reflector. The crystals are further wrapped in thin aluminium foil which is electrically connected to the photodiode-preamplifier assembly to provide a Faraday shield. Finally the crystals are covered on the outside with a layer of mylar to assure electrical isolation from the external support structure.

2.7.3   EMC Electronics and Readout

Each CsI(Tl) crystal is instrumented with a series of electronics. Two silicon photodiodes are glued to the rear of the crystal to collect scintillation light. Using two diodes allows redundancy and the averaged signal readout limits noise. The signal from each diode undergoes initial amplification by preamplifiers mounted close to the photodiode to limit noise due to extra capacitance. The preamplifiers and calibration circuitry are housed within the crystal cannister as shown in figure 2.19. A full schematic of the readout electronics chain is shown in figure 2.20.

Signals are taken from the preamplifiers through shielded ribbon cable to the rest of the electronics chain which are housed outside the active detector volume. In the barrel the ribbon cables run along the θ direction to mini-crates housed on both ends

of the barrel. The forward 24 rings of crystals are read out at the front face, while the backward 24 rings are read out at the backward face. In the forward endcap the mini-crates are mounted immediately adjacent to each section of crystals. Barrel mini-crates take cables from 72 crystals which connect via a Fan-Out Board (FOB), while for the endcap 48 crystals are read out.
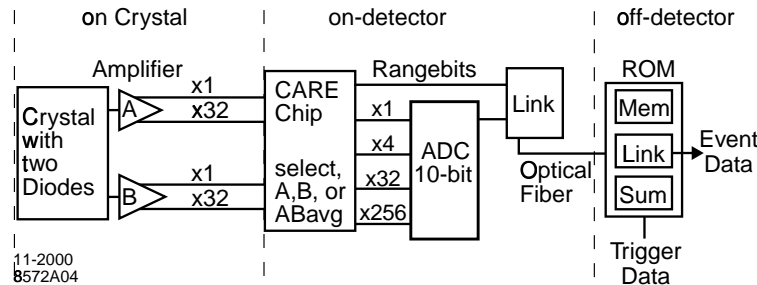
Figure 2.20: EMC read out design

Each mini-crate houses 6 Analogue-to-Digital Boards (ADB), while endcap mini-crates have 4 ADBs with each ADB serving 12 crystals. Each ADB contains 3 Custom AutoRange Encoding (CARE) chips and some Analogue-to-Digital Converter (ADC) circuitry. Each CARE chip serves 4 crystals and provides dynamic amplification of the signal. The pre-amplifier splits the ouput signal into $\times 1$ and $\times 32$ amplification ranges. Upon reaching the CARE the signals are split into 2 more ranges which provide further amplification. This gives four different amplification ranges corresponding to $\times 1$, $\times 4$, $\times 32$ and $\times 256$. The ADC circuitry compares the output of each range and selects the highest voltage output, which is not above range saturation. The selected output signal is then digitised and sent for further processing along with the selected range.

The output of each ADB is passed to one Input-Output-Board (IOB) which serves the mini-crate. The output of 24 channels (2 ADBs) is sent through an optical fibre to the ROMs housed in the electronics house for further processing and feature extraction.

2.7.4 EMC Electronics Calibration

Each channel within the EMC requires its electronics to be calibrated so to accurately characterise the response across the dynamic range. During normal running charge is created by the photodiodes as they accept scintillator light from the crystals. During an electronics calibration the charge pulses are produced by calibration circuitry built into the preamplifier and CARE chip.

The calibration circuitry injects the charge directly into the pre-amplifier input. The pre-amplifier contains circuitry that shapes the pulse so that it is similar to that produced from the photodiode. The charge pulses are created by discharging one of two capacitors. One capacitor is *small* with a capacitance of 220fF and the other *large* with a capacitance of 1.8pF. The voltage across the capacitors can be varied between $0 - 2V$. The small capacitor covers the full $\times 256$ and $\times 32$ energy range. The large capacitor is designed to cover the $\times 1$ and $\times 4$ range as well as enough of the $\times 32$ so that the calibration across all ranges can be matched. The capacitor and voltages can be selected in software and are controlled by commands sent through the IOB.

Unlike data taking mode where the range selection is based upon the input signal, during the electronics calibration each range is systematically selected and calibrated. The calibration consists of pulsing a well defined amount of charge (represented by a Digital Analogue Converter (DAC) value) into the pre-amplifier circuit and measuring the response in terms of the ADC output. For each gain range 100 charge injection pulses are made covering the entirety of its dynamic range.

The output data from all the gain ranges are then used to perform a global linear fit. Some data points are not suitable for fitting as they may be taken once the ADC had saturated or they might be in a region where a linear response is not expected such as the lowest charge injection values for the large capacitor. These data points are removed from the fit by a series of pre-defined selection criteria.

The fit is performed assuming a linear response in each gain range. The fit extracts the gain for each range, the initial pedestal value for each range, the ratio of the

capacitor values and initial offsets. The χ^2 of each crystal fit is used to define whether the crystal shows an acceptable response. Additionally the residuals of the data from the fit parameterisation are stored and used to correct for regions of non-linearity in the electronics response. The results of the electronics calibration and direct energy calibrations using a radioactive source with known energy are used to form Look Up Tables (LUT) which define the energy seen by crystals during data taking.

2.7.5   EMC Reconstruction

A particle showering in the EMC typically deposits energy over several crystals. The individual crystals are grouped into clusters. Local maxima, known as *bumps*, are searched for within the cluster. Bumps allow the separation of particles that have entered and showered close to one another, so forming one larger cluster. Correction factors are applied to the cluster and bump energies to take account of energy lost through leakage and from particles showering before entering the calorimeter. A track matching algorithm is also applied to determine whether the cluster is associated with a neutral or charged candidate.

2.7.6   EMC Performance

The energy resolution of a homogeneous crystal calorimeter can be described empirically by the sum of two terms added in quadrature

$$\frac{\sigma_E}{E} = \frac{a}{E(\,\mathrm{GeV})^{1/4}} \oplus b \tag{2.2}$$

where E and σ_E refer to the energy of a photon and its rms error measured in GeV. The energy dependent term a arises mainly from the fluctuations in photon statistics, but is also a function of the electronics noise. Additional beam related background photons add to the noise. The constant term b is dominant at high energies ($> 1\,\mathrm{GeV}$) and arises from non-uniformity in the light collection, leakage and absorption.
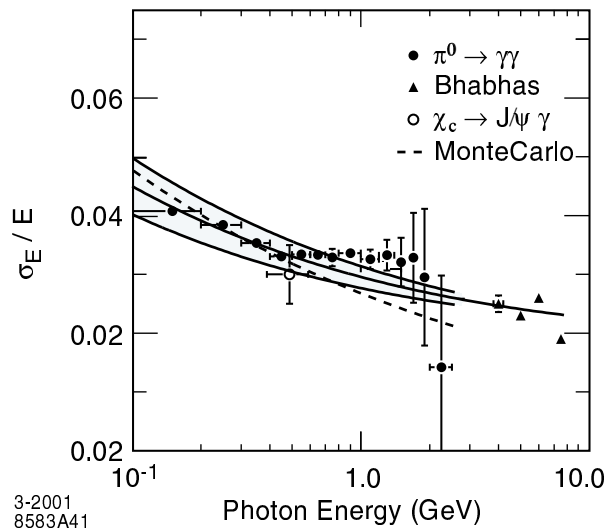
Figure 2.21: The energy resolution for the EMC measured for photons and electrons. The solid curve represents a fit to equation 2.2 and the shaded area denotes the rms error on the fit.

At low energy the energy resolution is measured directly with a radioactive source giving $\sigma_E/E = 5.0 \pm 0.8\%$ at 6.13 MeV. At high energy the resolution is derived from Bhabha scattering where the energy can be predicted by the polar angle of the $e^{\pm}$. The measured resolution is $\sigma_E/E = 1.90 \pm 0.07\%$ at 7.5 GeV. Figure 2.21 shows the measured energy resolution for the EMC derived from different physics processes. A fit to the energy resolution below 2 GeV is performed using these data and yields

$$\frac{\sigma E}{E} = \frac{(2.32 \pm 0.30)\%}{E(\,\mathrm{GeV})^{1/4}} \oplus (1.85 \pm 0.12)\%. \tag{2.3}$$

These values are slightly worse than the original design expectations, but agree relatively well with detailed Monte Carlo studies including the impact of electronics noise and beam backgrounds.

The angular resolution is determined by the transverse crystal size and the distance from the interaction point. It can be parameterised as a sum of an energy dependent and a constant term

$$\sigma_\theta = \sigma_\phi = \frac{c}{\sqrt{E(\,\mathrm{GeV})}} + d, \tag{2.4}$$

where E is measured in GeV. The measurement of the angular resolution is based on the analysis of π^0 and η decays to two photons of approximately the same energy.
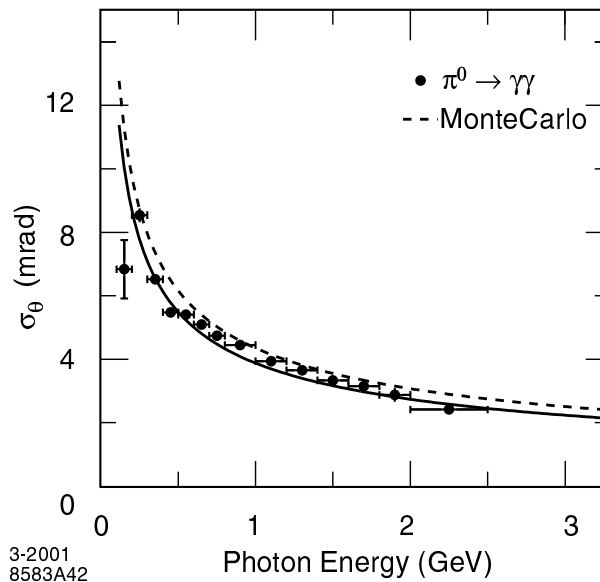
Figure 2.22: The angular resolution of the EMC for photons from π^0 decays. The solid curve is a fit to equation 2.4.

Figure 2.22 shows the measured angular resolutions from π^0 decays. The resolution varies between 12mrad at low energies to 3mrad at high energies. Fitting to the empirical parameterisation in equation 2.4 gives

$$\sigma_\theta = \sigma_\phi = \left(\frac{3.87 \pm 0.07}{\sqrt{(E\,\mathrm{GeV})}} + 0.00 \pm 0.04 \right) \mathrm{mrad}. \qquad (2.5)$$

The values obtained are slightly better than those predicted from detailed Monte Carlo studies.

The separation of electrons from hadrons comes from the calorimeter shower energies, shower shapes and track momentum. The most important variable is E/p the ratio of the calorimeter energy (E) to the track momentum (p). Figure 2.23 shows the electron efficiency and pion misidentification probabilities derived using radiative Bhabha and $e^+e^- \to e^+e^-e^+e^-$ events. The misidentification efficiency is derived from reconstructed K_s^0 and τ decays. An electron efficiency of 88.1% in the momentum range $0.5 < p < 2.0\,\mathrm{GeV}/c$ is achieved with a misidentification rate of 0.15%.
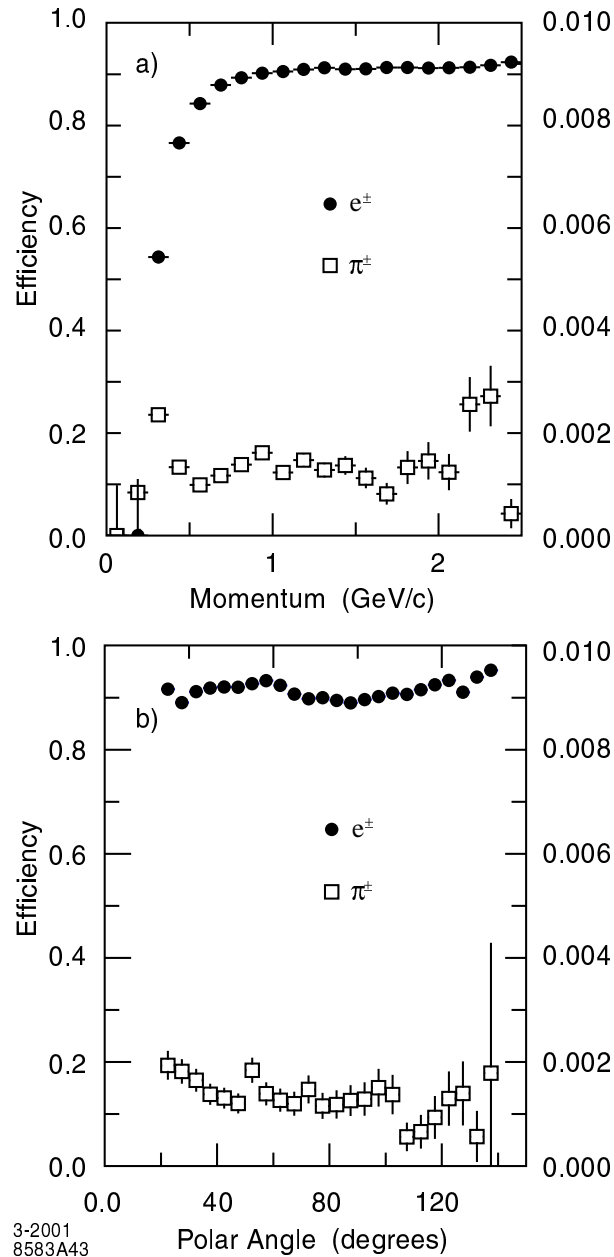
Figure 2.23: The electron efficiency and pion misidentification probability as a function of a) the particle momentum and b) the polar angle, measured in the laboratory system.

2.8   The Instrumented Flux Return (IFR)

2.8.1   IFR Physics Requirements

The IFR was designed to identify muons with good efficiency and high purity, and to detect neutral hadrons (primarily K_L^0) over a wide range of momenta and angles.

Muons play a key role in the measurement of CP violation. The decay of the J/ψ is reconstructed at $BABAR$ through its decay to either e^+e^- or $\mu^+\mu^-$. The flavour of the B candidate is often derived from its semi-leptonic decay. Both play a critical role in the measurement of $\sin(2\beta)$, as does the K_L^0 through the decay $B^0 \to J/\psi K_L^0$.

The major requirements of the IFR are that it provide large solid angle coverage, good efficiency and high background rejection for muons down to momenta below $1\,\text{GeV}/c$. For neutral hadrons, good efficiency and angular resolution are required. Due to the size and inaccessibility of the detector, high reliability and extensive monitoring of the detector and associated electronics are required.

2.8.2   IFR Design
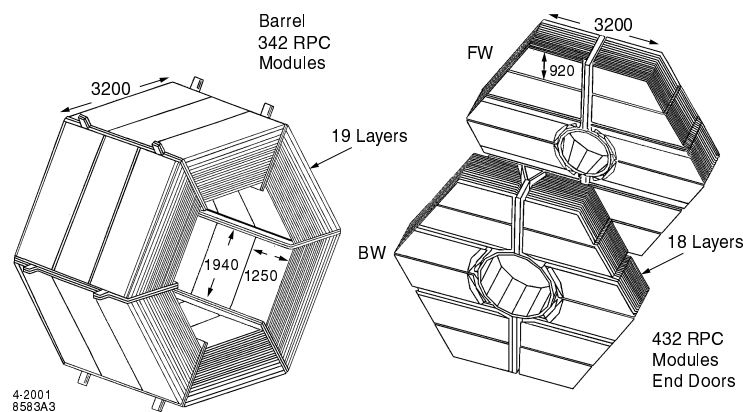
Figure 2.24: Mechanical structure of the IFR, showing the barrel sector (left) and the forward (FW) and backward (BW) end doors. The shape of the RPC modules and dimensions are given.

The IFR acts as both the flux return for the central 1.5T superconducting magnet and as a support structure for the rest of the $BABAR$ detector. The IFR acts as a muon filter and hadron absorber with Resistive Plate Chambers (RPC) installed in finely segemented steel of the barrel and end doors. The overall mechanical structure is shown in figure 2.24. The steel segmentation has been chosen on the basis of Monte Carlo studies of muon penetration and hadron interactions. The steel is segmented into 18 plates, increasing in thickness from 2cm for the inner plates to 10cm for the outermost plates. The nominal gaps between the plates is

3.5cm in the inner layers of the barrel and 3.2cm elsewhere. There are 19 RPC layers in the barrel and 18 in the endcaps. There are an additional two layers of cylindrical RPC's installed between the EMC and the magnet cryostat to detect low momentum particles exiting the EMC.
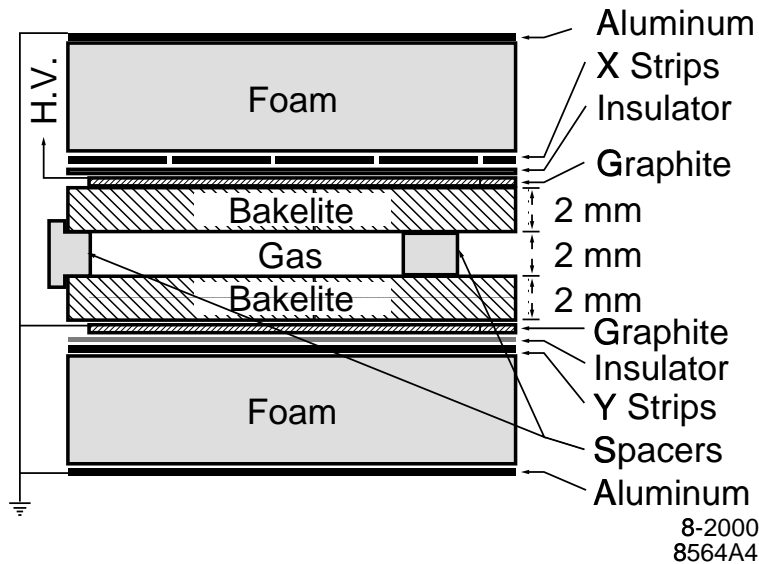
Figure 2.25: Cross section of an RPC showing the dimensions and the high voltage connection.

RPC's detect streamers from ionizing particles via capacitive readout strips. They are the prefered detection option as they are simple, have low construction costs and can cover complex shapes with minimal dead space. Additionally they provide large signals and good time resolution while position resolution depends on the segmentation. A cross section of an RPC is shown in figure 2.25. The RPC's consist of two bakelite (phenolic polymer) sheets, 2 mm thick and separated by a 2 mm gap. The gap is filled with a non-flammable gas mixture of 57% argon, 39% Freon134a, and 4.5% isobutane. The external surfaces of the bakelite are coated with graphite and connected to a high voltage of approximately 8 kV and ground. Signals are read out capacitively on both sides of the gap by external electrodes.

The IFR detectors cover a total active area of about $2,000 \text{m}^2$ and consists of 806 RPC modules. The barrel sectors have a readout pitch of 3.85cm in the z direction and between 1.97 - 3.28cm in ϕ. In the endcap the vertical has a pitch of 2.83cm and the horizontal has 3.8cm.

2.8.3   IFR Readout and Reconstruction

Charged particles travelling through the IFR lose energy via ionisation, producing a spark as they travel across each RPC. The electrical discharge is picked up by the electrodes, and the orthogonal strips on each side of the RPC chamber allow three dimensional positional information to be extracted. Data from the strips are sent to the Front End Card (FEC), which shapes and discriminates the signal and registers each strip which is above a predefined threshold. Each FEC serves 16 input strips. A fast OR of all FEC input signals provides time information. Signals from the 3,300 FEC's are transmitted to eight custom front end crates, housed close to the detector. The crates contain cards which buffer the data, extract timing information and then send the data through an optical fibre link to the DAQ system upon receiving a signal from the trigger system.

One dimensional clusters are formed by a group of adjacent hits in one of the two readout coordinates, with the position given by the centroid of the strips in the cluster. The clusters are then matched to tracks reconstructed in the DCH, and clusters within 12cm of the track are combined to form two or three dimensional clusters. A number of different factors are then used to determine the nature of the particle type such as the number of interaction lengths that have been passed through by the track, the track matching to the RPC clusters and the distribution of the RPC strips in the IFR layers.

2.8.4   IFR Performance

Figure 2.26 shows the muon efficiency and pion misidentification achieved by the IFR during Run 1 at *BABAR*. A muon efficiency of close to 90% has been achieved for momenta between $1.5 < p < 3.0\,\mathrm{GeV}/c$ with a fake rate for pions of less than 10%. The K_L^0 efficiency is significantly lower and varies between $20 - 40\%$ in the momentum range $1 - 4\,\mathrm{GeV}/c$.
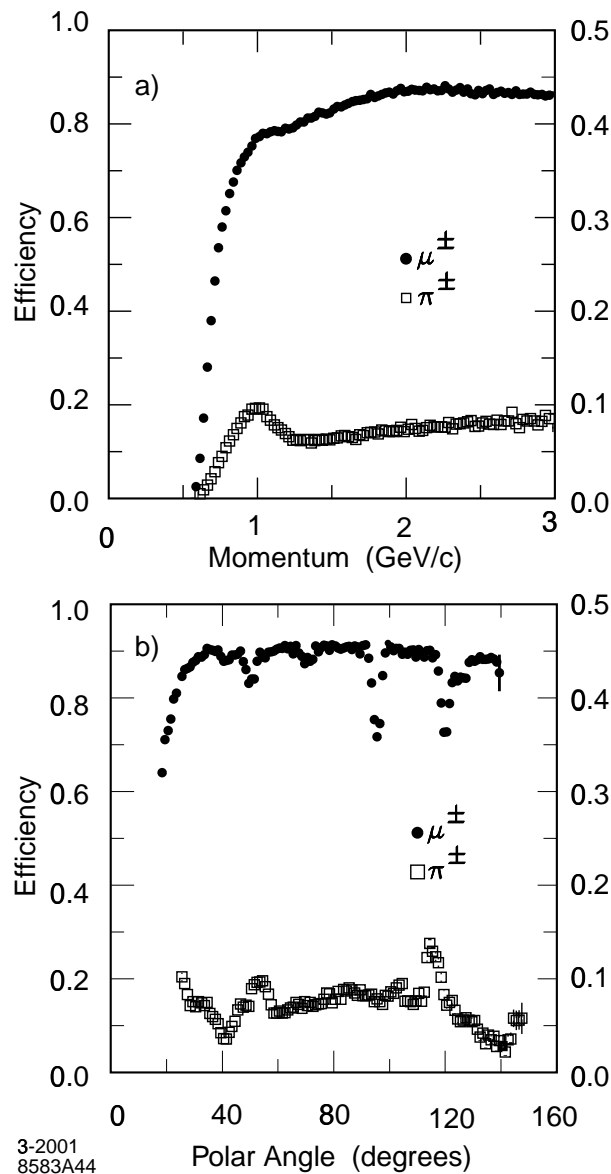
Figure 2.26: The muon efficiency and pion misidentification rates as a function of momentum (top) and of polar angle (bottom). These measurments are performed using clean muon and pion control samples gathered from data.

During the first years running at *BABAR* it was found that the RPC efficiency was deteriorating at an unsustainable rate. Initially the problem was traced to overheating which lead to dark currents within the RPCs increasing to levels which exceeded the HV system. The heating lead to 50% of RPC's showing a reduction in efficiency. Some RPC's had to be temporarily disconnected before additional cooling was installed on the detector. Since then a high number of the RPC's have shown a continued reduction in efficiency while some have remained stable.

During the shutdown between Run 1 and Run 2, the worst effected chambers in the forward endcap were replaced. Close inspection of the chambers that were removed showed signs that some of the treatment applied to the surface of the bakelite may have caused the problems, creating shorts across the chamber although a full understanding of the problem has not been achieved. Efficiency has continued to deteriorate with the muon efficiency down to $\approx 65\%$ by the end of Run 2. It is planned to replace the RPCs in the entire forward endcap region during the summer of 2002. Plans to replace the RPCs in the barrel region are currently being discussed, as are different detector technologies. The barrel region will probably be changed during the summer of 2005.

2.9   The Trigger System

2.9.1   Overview

The *BABAR* trigger system is designed to select events of interest while rejecting background events with a high, stable and well understood efficiency. The system is split into two levels, the Level 1 hardware based trigger and the Level 3 software based trigger. The Level 1 trigger is primarily designed to retain all physics events while greatly reducing background levels. The Level 3 trigger then selects the physics events of interest from those passing the Level 1 selection. For the study of CP violation the efficiency for $B\overline{B}$ events is required to be greater than 99% and the efficiency for lighter quark continuum events to be greater than 95%. It is also required that events such as Bhabha scattering which are used for luminosity measurements should have an efficiency which is known with an error of less than 0.5%. The trigger system is designed to accomodate up to 10 times the projected PEP-II background rates at design luminosity and to degrade slowly after this point. Triggers are produced within a fixed latency window of $11 - 12\,\mu$s after the bunch crossing.

2.9.2   Level-1 Trigger

The Level 1 trigger consists of a drift chamber trigger (DCT), an electromagnetic trigger (EMT), and an instrumented flux return trigger (IFT). These are connected to a global level trigger (GLT). The DCT and EMT are primarily used to select events while the IFT is used mostly for diagnostic purposes. Each of the L1 components produce *primitives*, which summarise data on the position and energy of particles. Primitives are sent to the GLT and are combined to form trigger lines. If the primitives satisfy trigger criteria a Level 1 accept is issued.

The DCT primitive objects consist of short and long tracks reaching different layers of the DCH, and high p_t tracks. The EMT primitive objects consist of towers, which correspond to the summed energy of rows of calorimeter crystals at the same ϕ angle. The towers then have different energy thresholds which correspond to different primitive objects.

The DCT and EMT are designed to act as two independent systems, each with over 99% efficiency for $B\overline{B}$ events. This allows the individual efficiency for each system to be clearly understood and it gives a combined efficiency of $\approx 99.9\%$ for selecting $B\overline{B}$ events. The overall level 1 trigger rate for a typical luminosity of $4 \times 10^{33} cm^{-2} s^{-1}$ is 1100 Hz, while the combined trigger/DAQ system was designed with an initial upper limit of 2 kHz.

2.9.3   Level-3 Trigger

The Level 3 trigger is a software based system designed to flexibly select the events of interest at a rate compatible with the overall reconstruction and data storage system. The Level 3 system was designed to store events at a rate of $\approx$100Hz at design luminosity. The Level 3 trigger has access to the complete event data including timing information and builds on the track and calorimeter cluster information used in the Level 1 trigger to generate more detailed information before selecting events.

Rather than attempting to reconstruct events, Level 3 develops and classifies the key event parameters such as track parameters, cluster energies and event topologies. The event parameters can then be combined in greater complexity to define different physics processes of interest and then select or reject events. The processes can also be pre-scaled so that certain types of events which might be useful for luminosity measurements, such as Bhabhas, can be accepted at a certain rate. Trigger rates are therefore kept under control while the necessary and interesting physics is recorded.

The Level 3 system is embedded in the Online Event Processing (OEP) framework (section 2.10) and runs on a 64 node farm. Events passing Level 3 are recorded and passed to the Online Prompt Reconstruction (OPR) system for full reconstruction.

2.10   The Data Acquisition and Online Computing System

2.10.1   The Data Acquisition System
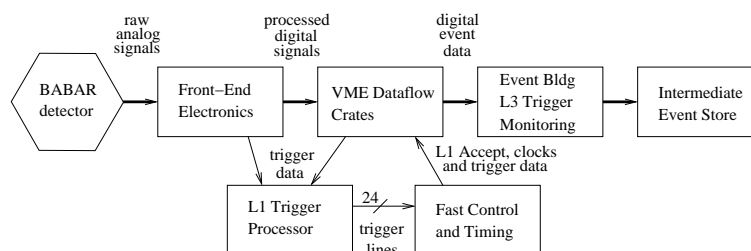
Figure 2.27: Schematic diagram of the *BABAR* DAQ system.

Figure 2.27 shows a schematic diagram of the *BABAR* data acquisition (DAQ) system. Each detector sub-system has front end electronics (FEE) which perform initial processing before passing the data via 1 Gbyte/s optical fibres to the Readout Modules (ROM's) contained in the Dataflow crates. Most sub-detectors use Triggered Personality Cards (TPC) within the ROM's which, upon receipt of a Level 1 accept trigger, collect the data from the front end. The EMC uses untriggered personality cards (UPC) which means that the data are continuously sent from the front end to the ROM's before being separated in software within the ROM depending on whether they correspond to an accepted event.

The ROM's perform sub-system dependent feature extraction (FEX) upon the data to extract signals from backgrounds before passing the data on to the OEP farm nodes which apply the level 3 selection algorithms. Events passing the level 3 selection are written to disk before being passed to the OPR system for full reconstruction. Data quality is continously monitored from the output of the nodes while the detector envirement indicators such as temperature, voltages, gas supplies, and humidity are extracted from the ROMs.

2.10.2   Online Prompt Reconstruction (OPR) System

The OPR system converts the stored data into an object orientated format which are written to the object database for physics analysis. The OPR system applies the full physics reconstruction to the stored data, creating all the physics quantities from the individual and combined sub-detector information. The OPR system also applies and derives continuous *rolling calibrations* for certain physics quantities which are then also stored in the database and used in the reconstruction. Key physics quantities derived from OPR are continuously monitored to maintain data quality. Presently the OPR system, processing an average of $200pb^{-1}$ of data a day, requires 200 computer nodes. An additional requirement of the system is that in any given year, the complete *BABAR* data set should be able to be reprocessed with improved reconstruction.

Chapter 3

Crosstalk in the EMC front-end electronics

3.1 Introduction

This chapter documents work that was undertaken to characterise and correct for crosstalk between readout channels within the EMC. The work was undertaken during the shutdown between Run 1 and Run 2. The chapter begins by describing how the crosstalk effect was first identified and the theories for its existence. The measurement process on the *BABAR* detector to characterise the effect is discussed, and the nature of the crosstalk in different areas of the detector is extensively examined. The chapter concludes by discussing the correction applied to the EMC electronics calibration and the effect the corrections had on data taken by the EMC. Full documentation for this effect and the subsequent measurements is available in [29].

3.2 Observation of Crosstalk in the EMC

3.2.1 Non linearities in the calorimeter energy spectra

The first year of running for the EMC within *BABAR* saw the diagnosis of two unrelated problems with the electronics used to read out the data from the Caesium

Iodide crystals making up the detector. Both problems effected the calibration of the detector and lead to significantly distorted calibration constants. As a consequence the look up tables (LUT) created by the calibration lead to a non-linear response in real data taking which manifested itself as gaps in the single crystal energy spectrum. Indeed it was this effect that led to the first diagnosis of the calibration problems.

While a correction was applied to the data taken during Run 1 [31] the ideal solution was to directly correct the problems effecting the electronics calibration. Studies of the electronics response highlighted two different problems. The first, and most severe, was an induced "ringing" in the electronics. An input pulse would cause a baseline oscillation in the electronics output. This effect, shown in figure 3.1, caused severe gaps and dips in the energy spectrum of crystals, most noticeably at energies characteristic of switches between the $\times 256$, $\times 32$, $\times 4$ and $\times 1$ read-out ranges. This effect was overcome by the addition of extra capacitance to the Analogue-Digital electronics boards (ADB) situated on the detector and was implemented at the end of Run 1 data taking.
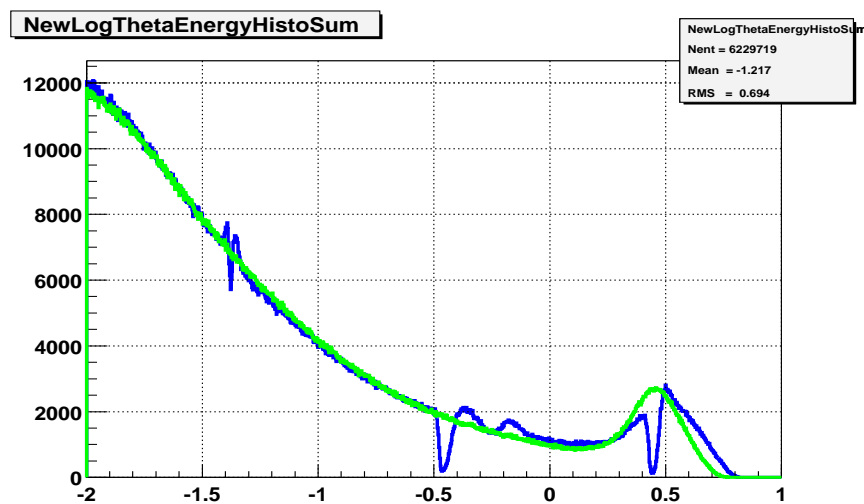
Figure 3.1: EMC crystal energy spectrum from Run 1 data showing gaps at energies consistent with range switches in the front end electronics. The x-axis units are $\text{Log}_{10}[\text{GeV}]$. The overlayed function shows the correction function applied for the Run 1 data.

The second effect can also be seen in figure 3.1 as an oscillatory behaviour in the region between 400MeV and 800MeV corresponding to the lower part of the $\times 4$

range. Studies indicated that this effect was caused by crosstalk between neighbouring channels which was seen to begin once the $\times 32$ range became saturated. In data taking this corresponds to an energy of 400MeV and it is rare that more than one or two neighbouring channels will reach this threshold energy. However, during the electronics calibration all channels simultaneously saturate in the $\times 32$ range so the crosstalk between channels is maximised. Consequently the results of the calibration will not accurately reflect the situation during data taking.

3.2.2   Observation of crosstalk in the electronics calibration

The observation of non-linearities in the energy spectra of individual crystals led to a series of tests being performed that first brought to light the existence of crosstalk in the EMC's front end electronics. Confirmation that crosstalk between the individual crystal readouts was a component of the non-linearity problem came by performing a modified electronics calibration. The standard electronics calibration injects charge into the diodes of every crystal in the calorimeter and reads back the response given by the front end. The known charge injected and the readout are then used to create the energy-readout lookup table (LUT) used during data taking. The modified calibration pulsed only half the crystals, those with "odd" or "even" numbering, but read out the whole calorimeter in the normal way. This meant that for two neighbouring crystals, one would be pulsed while the other would not.

Figure 3.2 shows the standard output of the GUI used to monitor the electronics calibration for a channel that has been pulsed. The eight regions of the GUI correspond to the four different ranges coupled to two different capacitors for charge injection. The x-axis corresponds to the amount of charge injected, while the y-axis represents the read out of the front end electronics. While not all combinations of range and capacitor are used (Range 1 and Range 3) we expect to see a linear response to charge injection from the front end readout as shown.

Figure 3.3 shows the corresponding output for a non-pulsed channel during a modified odd-even electronics calibration. While we expect to see no response from the
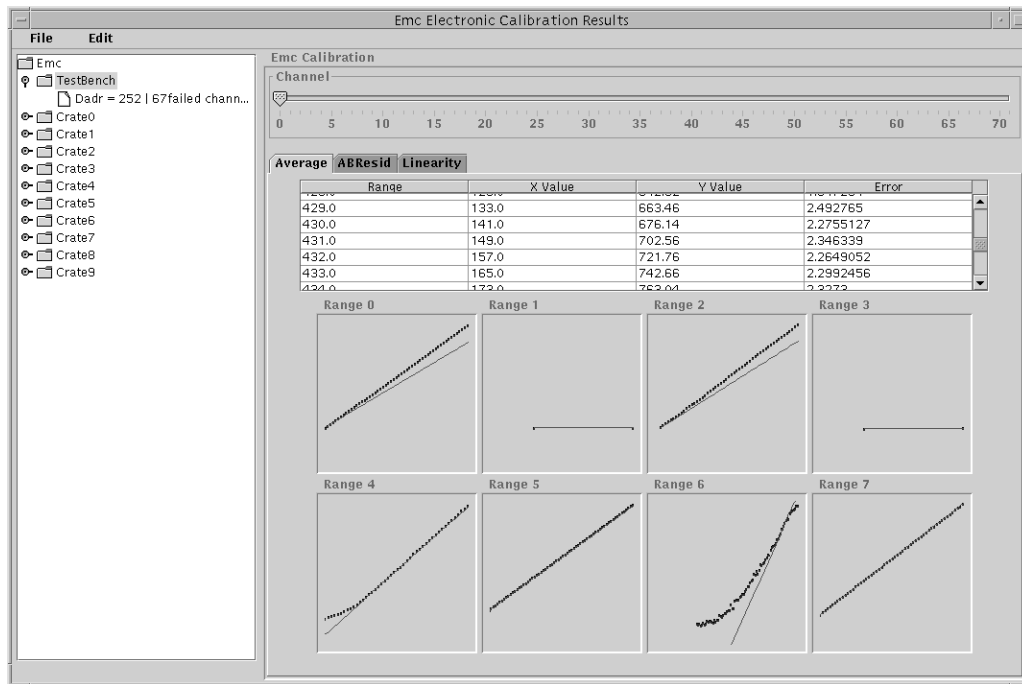
Figure 3.2: Standard output of the electronics calibration GUI for a pulsed channel. The 8 ranges correspond to the ×1 (0&1), ×4 (2&3), ×32 (4&5), and ×256 (6&7) electronics ranges using the large and small capacitors for charge injection.
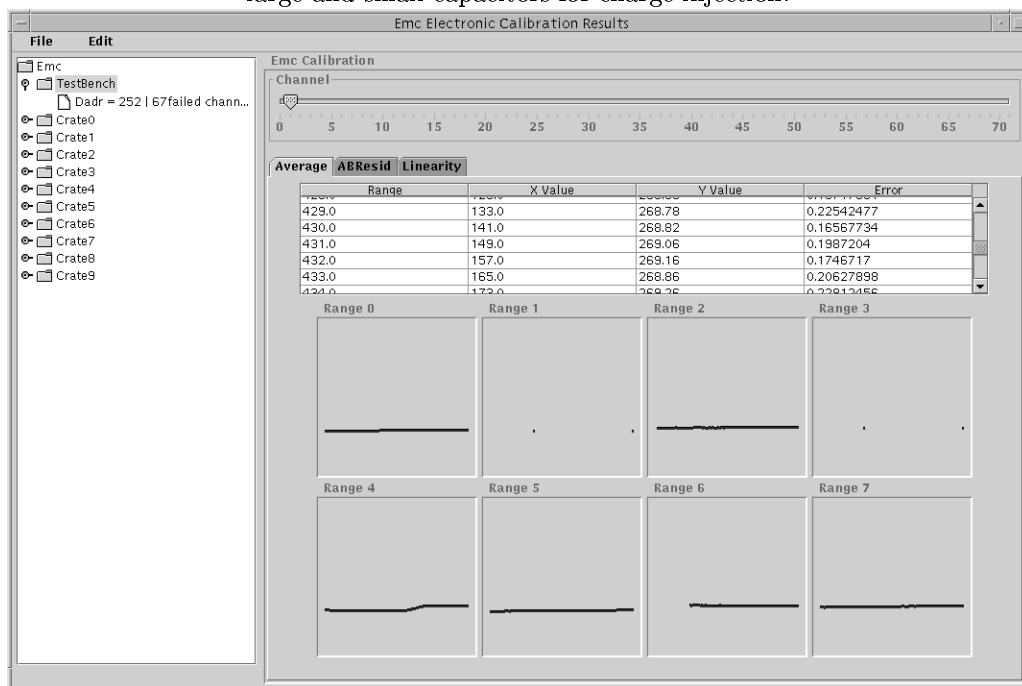
Figure 3.3: Output of the modified odd-even electronics calibration GUI for a non-pulsed channel. The 8 ranges correspond to the ×1 (0&1), ×4 (2&3), ×32 (4&5), and ×256 (6&7) electronics ranges using the large and small capacitors for charge injection.

front end, the GUI output for "Range 4" shows a noticeable pedestal shift. This corresponds to the point at which the ×32 range saturates in the pulsed channel and would be caused by a pulse energy of approximately 400 MeV. Detailed study of the readout numbers showed pedestal shifts of a few MeV in the nearest neighbouring channels to the pulsed channel. Summing the pedestal shifts induced in all the non-pulsed channels gave a 10 MeV effect, which is sizeable when compared to the 400 MeV pulse which induced it.

The data provided by the modified electronics calibration highlighted the problem but was insufficient to draw any definite conclusions. To examine the problem further required probing the effect on a crystal by crystal basis.

3.2.3   Possible origin of crosstalk within the EMC

Further lab tests were undertaken using an EMC test stand consisting of 21 crystals, configured to be similar to the barrel EMC setup. The tests were performed in conjunction with the electronics engineers at SLAC to try and understand the origin of the crosstalk problem. They concluded that the crosstalk propagates by capacitive (AC-)coupling. Essentially any nonconductive medium separating two shields (conductors) acts as a capacitor. This includes the interfaces between

- two preamplifier cables,

- two crystals,

- preamplifier box and preamplifier-diode cable.

A signal present on any of these can induce a signal on the other. The crystals, preamplifier box, and pre-amplifier cable all have common shielding for a given channel. Once a signal has been induced it will feed into the preamplifer by coupling from the preamplifier box into the diode-preamplifier cable. While grounding the shield closer to the preamplifier would probably have avoided this problem, however

then the DC noise pickup could be worse [32]. While the tests that were performed by the engineers ultimately proved inconclusive in terms of the exact cause of the crosstalk, they did confirm that no hardware fix for the grounding problem would be possible due to the limited access available to the effected areas of the detector. A software based fix for the problem would be necessary.

While the test stand was useful for diagnosing the nature of the crosstalk it was of little use in actually making quantitive measurements of the size of the effect. The limited number of channels, rudimentary setup and the often inconsistent response of the system lead to the conclusion that the crosstalk was best measured directly on the detector during the shutdown between Run 1 and Run 2 data taking during the winter of 2000 - 2001.

3.3   Crosstalk measurement procedure on the detector

The basic aim of measuring the crosstalk on the detector was to characterise the effect in such a way that a correction could be applied to the electronics calibration so limiting the crosstalk's impact on the quality of *BABAR* data. To achieve these goals it was decided that the best approach was to attempt to measure the crosstalk generated across the detector by single crystal pulses.

3.3.1   ADB extender boards

While the electronics calibration provided a solid platform for pulsing channels across all ranges, several modifications were required so it could be used to measure the crosstalk generated by single crystals. The calibration circuit situated on the ADB(Analogue-Digital Board) was designed to pulse all channels simultaneously. While the software related to the calibration contained methods for selecting only one channel, this only referred to the readout of the calibration and not the pulsing

itself. Therefore selecting one channel in software would generate as much crosstalk as before, because all the channels were being pulsed and read out.

Allowing single crystals to be pulsed required an adjustment to the calibration circuitry. Extender boards were designed and built, which attached to each ADB. The boards intercepted the calibration pulse for each of the 12 crystals served by the ADB, switches then allowed individual channels to receive the pulse. Six such boards were attached to the ADB's in selected barrel minicrates corresponding to 72 individual channels. Minicrates in the endcap were also studied. These contain 4 ADB's corresponding to 48 channels of which only 41 are instrumented. This allowed single channels to be pulsed within the minicrate.

3.3.2   Adjustments to the electronics calibration

One of the main considerations when planning the measurement procedure was time. During the shutdown, time with an operational EMC was at a premium due to having to fix the hardware fault which caused the major source of non-linearities outlined in section 3.2.1. To maximise the number of channels and minicrates that could be measured, a revised electronics calibration was prepared.

The full electronics calibration pulses all four ranges, using two different capacitors and three different diode combinations. The revised version pulsed the $\times 1$ and $\times 4$ ranges using the large capacitor, the $\times 32$ using the large and small capacitor and the $\times 256$ range using the small capacitor. All of these were done reading out the average of both diodes on the crystals. These changes meant the single crystal calibration was approximately 4 times quicker than the full calibration.

While the calibration circuit on each ADB was designed to pulse all channels simultaneously, the calibration code itself was designed to pulse all minicrates on the detector simultaneously. This meant that even with the extender boards attached to the minicrate of interest, running the calibration would pulse all the channels in all other minicrates. While there was not expected to be crosstalk between minicrates,

we adjusted the calibration so that individual minicrates could be addressed while still reading out the results from all other channels. This meant that an individual channel could be pulsed while the rest of the calorimeter was read out.

3.3.3   Overview of the measurements taken

During the course of the shutdown it was possible to take single crystal calibrations for one full minicrate in the forward and one in the backward barrel, and one in the endcap. We had originally intended to make more measurements for different hardware configurations but various teething troubles with the extender boards and the exact configuration of the measurements restricted this. Additionally much of the EMC was unavailable during the shutdown period due to work being done on the hardware fix for ringing described in section 3.2.1.

The data collected consisted of the single crystal electronics calibrations through the $\times 256$, $\times 32$, $\times 4$ and $\times 1$ ranges as described earlier and the response of the unpulsed channel readout in the $\times 256$ range where the response to the relatively small crosstalk pulse would be most sensitive.

3.4   Characterisation of the Crosstalk

The main objective of the crosstalk measurements was to develop a correction that could be applied to the electronics calibration. The data taken during the measurement process allowed this to be completed because

1. The single crystal electronics calibration provided the first data showing the genuine response of the front end diodes with all other crosstalk between channels removed

2. The single crystal data could be compared with the results from the full calibration allowing a correction to be developed and applied for all future electronics calibrations

While it is relatively rare that a single crystal goes above the 400 MeV ×32 threshold during regular data taking, all crystals go above this threshold during the electronics calibration. Previous measurements showed that the effect set in as the ×32 range saturated and remained constant throughout the ×4 and ×1 ranges. This particularly effected the ×4 range for two reasons. Firstly the distortion to the calibration occurs at the range switch between the ×32 and ×4 ranges which is a particularly sensitive region as the electronics calibration attempts to link these two ranges in seamless fashion. Additionally the crosstalk effectively turns on in the low energy region of the x4 as the range switch from ×32 to ×4 occurs prior to the ×32 saturating so creating the greatest distortion in the calibration of the ×4 range.

Secondly, the crosstalk effect is at its largest in comparison to the genuine electronics calibration pulse in the lowest energy region of the ×4. In the ×1 range the crosstalk pulse is constant and small in comparison to the electronics calibration pulse so minimizing its impact on the calibration. This meant that the calibration for much of the ×4 range was not representative of the real performance of the system which in turn has a large impact on the quality of data taken.

The first step in developing a correction was to characterise the exact nature of the crosstalk across the different regions of the detector.

3.4.1   Fitting the Crosstalk Pulse

While work using the EMC test stand and the odd-even calibrations had highlighted some of the crosstalk features, the single channel detector measurements allowed the effect to be studied on a channel by channel basis for the first time. Figure 3.4 shows the size of the crosstalk relative to the charge deposited in the pulsed diode measured on a non-pulsed crystal which wasn't an immediate neighbour to the pulsed channel.

The first thing to note is the shape of the induced crosstalk. The crosstalk can be broken into 3 distinct linear sections. Initially the induced crosstalk is small and rises slowly with the pulsed channel's energy. At approximately 400 DAC counts

there is a sudden sharp rise in the crosstalk magnitude before a plateau is reached at approximately 500 DAC counts. At higher energies the crosstalk magnitude appears to be unchanged, remaining at the plateaued value. Examination of many single channel measurements confirmed that this was the standard behaviour observed for channels that weren't nearest neighbours to the pulsed channel. The point at which the sharp rise occured in the crosstalk magnitude (400 DAC counts) corresponded directly to the point at which the x32 range in the pulsed channel began to saturate in the high gain pre-amps.
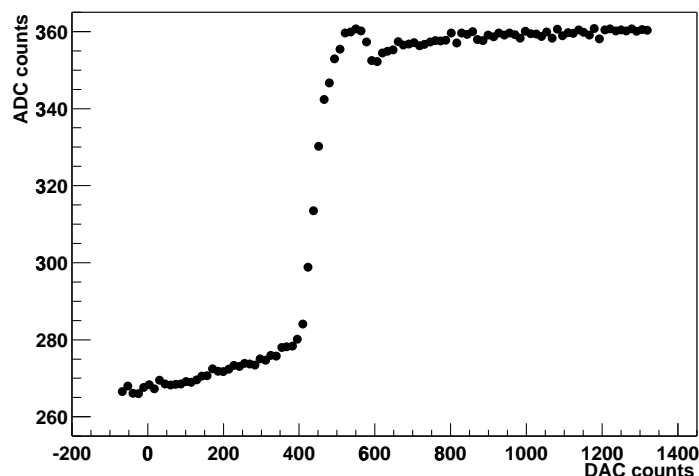
Figure 3.4: The induced crosstalk in a channel due to a single pulsed channel in the same ADB. The pulsed channel is not an immediate neighbour to the readout channel. The x-axis is the DAC or charge injected into the pulsed channel during the modified electronics calibration. The y-axis is the ADC counts read out from the non-pulsed crystal without pedestals subtracted.

While the magnitude of the induced crosstalk appeared to follow the pattern highlighted above there were some anomalies. The most obvious occured in channels immediately surrounding the pulsed channel, the nearest neighbour channels. Figure 3.5 shows such a pulse; the striking difference is the region prior to saturation which shows a much sharper relative rise in the induced crosstalk, indeed the magnitude of the crosstalk prior to saturation is comparable to that induced during saturation. This seemed to appear in all channels immediately next to the pulsed channel and gave a hint that there was perhaps more than one crosstalk generating process taking place.
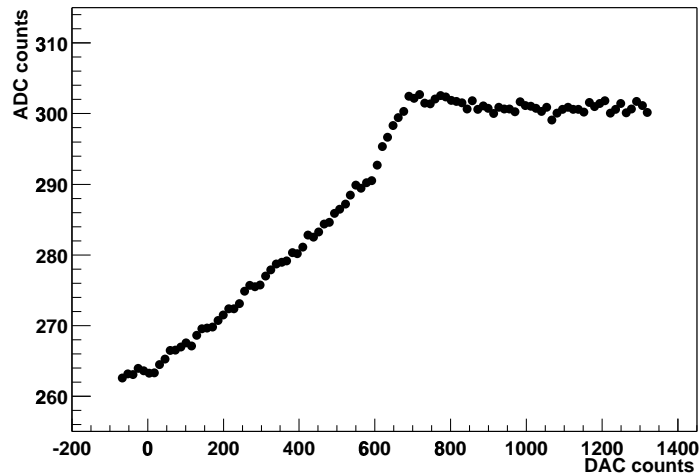
Figure 3.5: The induced crosstalk in a channel due to a single pulsed channel in the same ADB where the pulsed and readout channels are immediate neighbours. The x-axis is the DAC or charge injected into the pulsed channel during the modified electronics calibration. The y-axis is the ADC counts read out from the non-pulsed crystal without pedestals subtracted.

Further investigation of individual channel crosstalk lead to the conclusion that all effects could be characterised by a combination of 3 linear processes dependent on the pulse energy. The first step was a linear rise prior to saturation, the second was the main pedestal shift observed during saturation and the final linear section characterised the final observed pedestal shift at energies above saturation. As the crosstalk seemed to vary from channel to channel and with varying magnitudes dependent on which ADB contained the pulsed channel and which ADB contained the observed crosstalk channel, the best method of characterising the effect was to fit each individual crosstalk spectrum. Figure 3.6 shows an example of a fit to the crosstalk spectrum using 3 straight lines.

The fit was performed for each possible configuration, that is to say that in one barrel IOB there are 72 channels which were pulsed individually, for each channel pulsed there were 71 crosstalk measurements for the other channels, and each of these were fitted. The fit was performed using data taken in the x256 range for the unpulsed channel as this is the range where crosstalk is most easily observed during data taking and is the most sensitive to the low energy crosstalk pulse. During the fit process the pedestal of the unpulsed channel was removed and 4 effective pairs
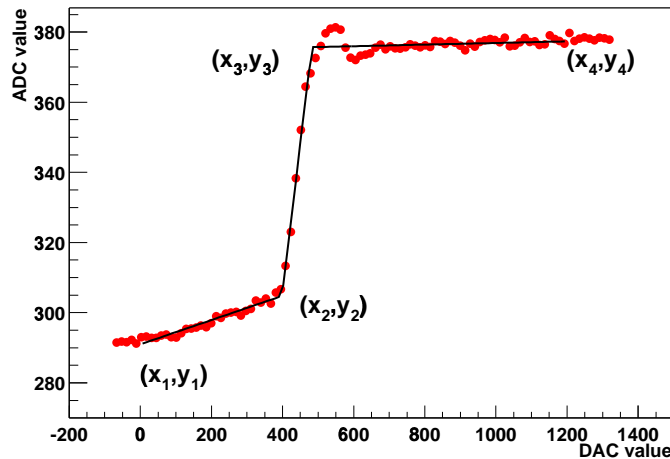
Figure 3.6: An example of the fit used to characterise the crosstalk. Three straight lines are used to represent the main features of the crosstalk spectrum and are put together into one continuous fit. The x-axis is the DAC or charge injected into the pulsed channel during the modified electronics calibration. The y-axis is the ADC counts read out from the non-pulsed crystal without pedestals subtracted. The four co-ordinates extracted from the fit, $(x_1, y_1), (x_2, y_2), (x_3, y_3)$ and (x_4, y_4) are shown on the plot.

of coordinates were extracted with the x coordinate representing the energy of the pulsed channel creating the crosstalk and the y coordinate representing the energy magnitude of the induced crosstalk pulse. The four pairs of coordinates refered to the (x_1, y_1) starting point where $x_1 = 0$, the (x_2, y_2) point where the x32 range begins to saturate, the (x_3, y_3) point characterising the end of the main pedestal shift in the unpulsed channel, and the final (x_4, y_4) end point representing the end energy of the crystal spectrum where $x_4 = 1200$. The four co-ordinates are shown on figure 3.6.

This formalism allows the crosstalk induced by a particular channel to be studied across the IOB, and to be split into 3 distinct sections:

1. **Δ_1: Magnitude of crosstalk induced prior to the $\times 32$ saturating, given by $(y_2 - y_1)$**

2. **Δ_2: Magnitude of main crosstalk pedestal shift, given by $(y_3 - y_2)$**

3. **Δ_3: Any post-pedestal shift correction, given by $(y_4 - y_3)$.**

It is important to state that the analysis presented beyond this point leans heavily on this formalism and the comparison of crosstalk across the detector is done in terms of the magnitudes of Δ_1, Δ_2, and Δ_3. Using this methodology it was then necessary to compare the magnitude of the induced crosstalk between the barrel and endcap regions and to see how stable the crosstalk seen in the different regions might be. The following section highlights the results for the different regions we did measure.

3.5   Crosstalk across the detector

In this section we examine the magnitude of the induced crosstalk in the two main sections of the detector, the barrel and the endcap. Having examined the data and fitted for the crosstalk pulses induced by the single crystal electronics calibration we then set about characterising the behaviour. Firstly we examine the barrel region.

3.5.1   Crosstalk in the Calorimeter barrel
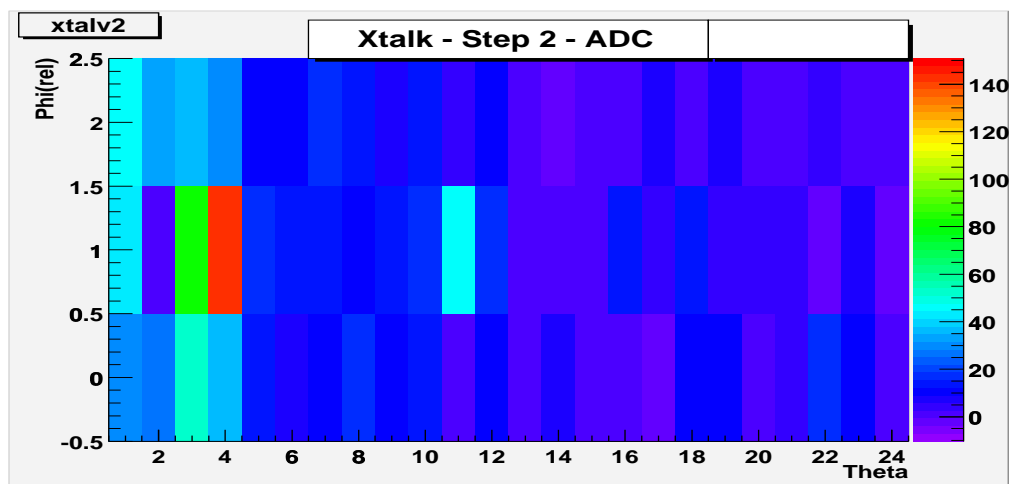
Figure 3.7: Magnitude of measured Δ_2 in the barrel mini crate channels due to a pulsed channel within the minicrate. The pulsed channel is situated at (2,1) in (θ,ϕ) coordinate space and has been set to zero for the purposes of this plot.

Figure 3.7 shows the magnitude of Δ_2 induced in a backward barrel minicrate module from a crystal pulsed at one end of the module. In analysing these plots it is important to remind ourselves of the structure of the barrel module. The module consists of 6 ADB's of 12 channels each, these are organised into blocks linearly in θ and consist of 3 channels in ϕ and 4 channels in θ.

We can see from this figure that the measured Δ_2 values appear to be largely contained within the channels served by the pulsed channel's ADB, and is maximal along the same ϕ strip as the pulsed channel. There are additional channels in different ADB's along the same ϕ strip that show induced signals also. The highest pulse is approximately 140 ADC counts, with each ADC count in the $\times 256$ range corresponding to 0.03 MeV, so the highest pulse registers several MeV in energy and approximately 10 MeV within the pulsed ADB.

While such a plot gives some indication of the structure of induced crosstalk signals throughout the barrel module, the best way to analyse the data is to see how all the pulsed channel measurements compare for Δ_1, Δ_2 and Δ_3. Figure 3.8 shows the magnitude of Δ_1 across the barrel module.
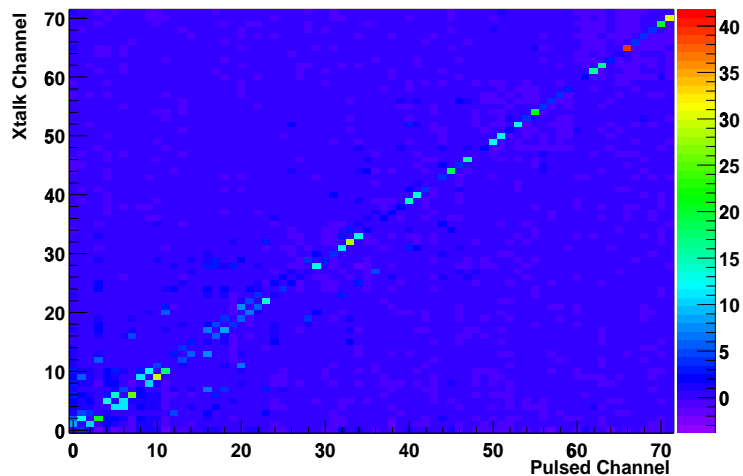
Figure 3.8: Measured Δ_1 in the barrel minicrate channels for different pulsed channels within the minicrate. The pulsed and readout channel are numbered between 0-71, and are grouped in sets of 12 representing each ADB within the minicrate. The crosstalk is measured in ADC counts. The values for the pulsed channel have been set to zero.

The magnitude of Δ_1 appears to be negligible for nearly the entire minicrate module, except for the channel immediately next to the pulsed channel where a significant signal can be recorded. Typically the measured pulse size is only 10-15 ADC counts in the effected channels, but there are exceptions. This represents a small overall effect of a fraction of an MeV in terms of energy. It is noticeable that for low numbered pulsed channels, there appear to be more than one channel affected by crosstalk while for the higher numbered channels there seems to be only one channel affected. The lower numbered channels represent those that are deepest within the detector, furthest away from the front end electronics and with the longest cable length between the crystals and the front end electronics. The higher numbered channels are closer to the front end electronics.
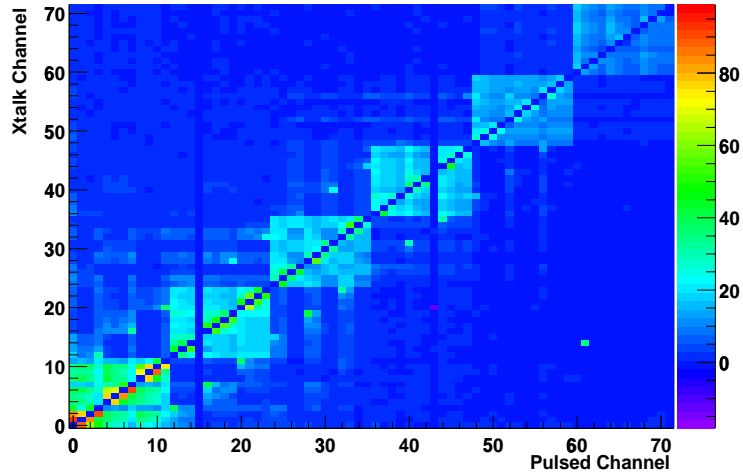
Figure 3.9: Measured Δ_2 in the barrel minicrate channels for different pulsed channels within the minicrate. The pulsed and readout channel are numbered between 0-71, and are grouped in sets of 12 representing each ADB within the minicrate. The crosstalk is measured in ADC counts. The values for the pulsed channel have been set to zero.

Figure 3.9 shows the magnitude of Δ_2 induced across the barrel minicrate module. This represents the main crosstalk effect. It is clear that Δ_2 is largely contained within the ADB of the pulsed channel. Δ_2 is substantially greater than Δ_1 and effects far more channels for a particular pulsed channel. The Δ_2 size also gets progressively smaller in the ADB's as they get closer to the front end electronics, or as the channel number increases. As with Δ_1, Δ_2 shows the greatest values in

the channels immediately surrounding the pulsed channel. Unlike Δ_1, Δ_2 shows measureable signals in channels outside of the ADB containing the pulsed channel. These channels tend to run along the same ϕ strip as the pulsed channel, as we saw in figure 3.7.
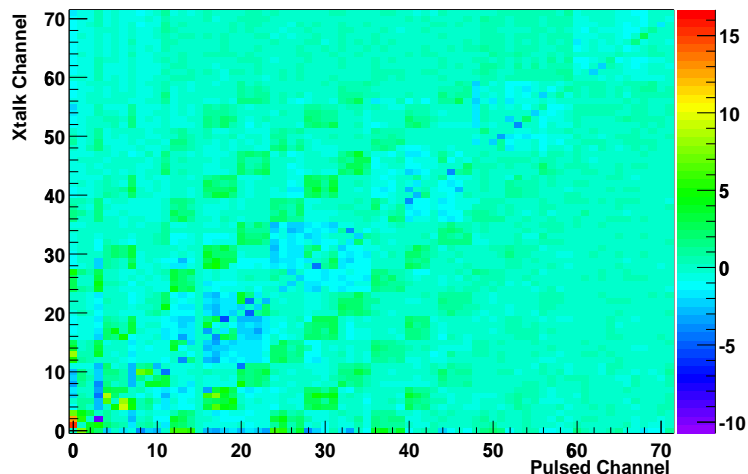
Figure 3.10: Measured Δ_3 induced in the barrel minicrate channels for different pulsed channels within the minicrate. The pulsed and readout channel are numbered between 0-71, and are grouped in sets of 12 representing each ADB within the minicrate. The crosstalk is measured in ADC counts. The values for the pulsed channel have been set to zero.

Figure 3.10 shows the magnitude of Δ_3 induced across the barrel minicrate module. As we can see Δ_3 is small, with very little change from the pedestal reached after Δ_2. There are a few channels showing small ± 5 ADC count changes but there is no clear pattern. One pattern that can be faintly seen is a chequered box structure of channels showing a positive ADC count change. These channels once again seem to lie on the same ϕ strip as the pulsed channel.

The general trends for the barrel can therefore be summarised:

1. The maximum induced crosstalk is seen in the crystals immediately surrounding the pulsed channel.

2. The crosstalk is primarily contained within the channels read out by the same ADB as the pulsed channel but there is some residual crosstalk seen throughout the IOB.

3. The maximum crosstalk seen in any channel corresponds to an energy of approximately 5 MeV.

4. The magnitude of the induced crosstalk is proportional to the cable length connecting the crystals and the ADB,

5. The crosstalk is maximised along the ϕ strip of the pulsed channel.

6. Δ_1 shows significant signals in the immediate neighbours to the pulsed channel.

7. The maximum values of Δ_2 are approximately 5-10 times greater than those of Δ_1.

8. The magnitude of Δ_3 is negligible in comparison to Δ_1 and Δ_2.

The fact that the crosstalk was maximised along the ϕ strip of the pulsed channel, and that the crosstalk was greater the further away from the front end electronics the pulsed channel's ADB was, gives an indication as to one source of the crosstalk. The key difference between the different sets of 12 crystals read out by each ADB is the cable length between the crystal and the readout. The deeper they are into the EMC, the longer the cable length. It therefore appears that the induced crosstalk is proportional to the cable length. Additionally each ADB has 3 cables, one for each set of 4 channels in a ϕ strip. Each ϕ strip cable lies on top of the others from the other ADB's so providing a hint as to why the crosstalk is maximised in the ϕ direction.

3.5.2   Crosstalk in the Endcap

Figure 3.11 shows the size of Δ_2 induced in an endcap minicrate. The endcap minicrate structure is substantially different to the barrel, with only 4 ADB's and not all of the channels instrumented. Figure 3.11 shows the 4 ADB's and effectively represents a section of the overall circular structure of the endcap. The first thing to note is that the magnitude of Δ_2 is substantially smaller in the endcap than the barrel(see figure 3.7), roughly 1/10 the size of the peak barrel measurements.
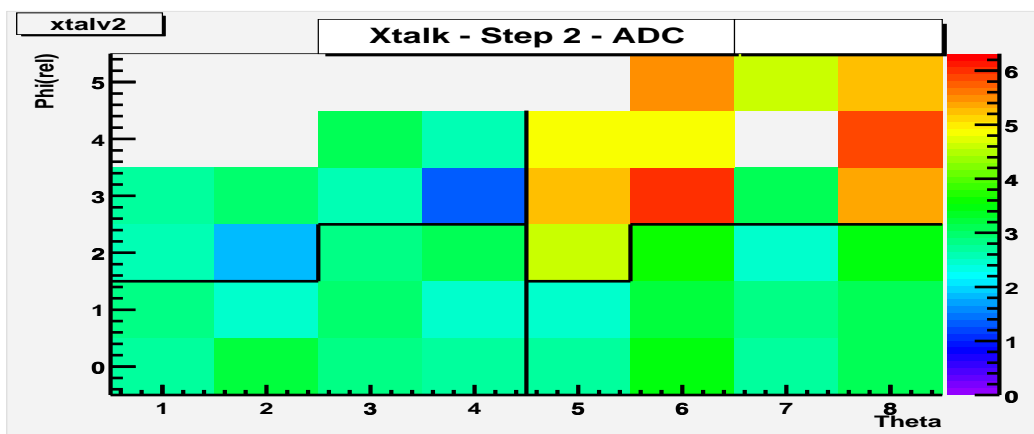
Figure 3.11: Magnitude of Δ_2 induced in the endcap minicrate channels due to a pulsed channel within the minicrate. The pulsed channel is situated at (7,4) in (θ,ϕ) coordinate space and has its readout value set to zero. The channels along the ϕ strip between (1,5) to (5,5) and (1,4) to (2,4) are not present in the endcap minicrate.

As with the barrel the measured values are maximal within the pulsed channel's ADB but is also seen across all the ADB's at a reduced level. Of course figure 3.11 represents one particular pulsed channel, we should look at all the channels across the endcap to make further conclusions.
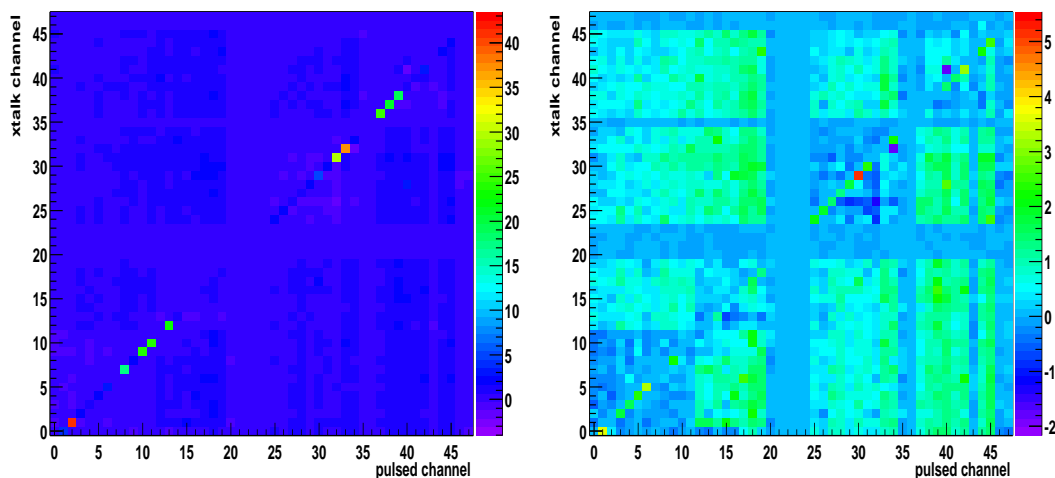
Figure 3.12: Measured Δ_1 in the endcap minicrate channels for different pulsed channels within the minicrate. The left hand plot shows the full results, while the right hand plot shows the results with magnitudes below 6 ADC counts. The pulsed and readout channel are numbered between 0-47, and are grouped in sets of 12 representing each ADB within the minicrate. Only 41 of the channels are instrumented. The crosstalk is measured in ADC counts and the pulsed channel's value has been set to zero.

Figure 3.12 shows the magnitude of Δ_1 for different pulsed channels across the endcap. The left hand plot shows that there are, like the barrel, a series of neighbour channels to the pulsed channel that show significant Δ_1 signals. While in the barrel every pulsed channel had a nearest neighbour that showed significant signals, the same is not true in the endcap with only a few showing the effect. The right hand plot shows the induced signals below 6 ADC counts and shows more structure than the left hand plot. We can see that once again the nearest neighbours do tend to have higher values, while there is also smaller signals seen across the whole endcap module. The uninstrumented channels (20 - 23, 35, 46 - 47) are clearly visible.

The pattern is far more complex than the barrel. In the first ADB (channels 0 - 11) and the third ADB (channels 24 - 35) we see Δ_1 signals only in the nearest neighbours when a channel is pulsed within the ADB, but we also see signals in all the other ADB's. In the second (channels 12 - 23) and fourth (channels 36 - 47) ADB's we see reduced signals in the pulsed ADB, and significant signals in all the other ADB's. For reference in figure 3.11 ADB 1 and 3 are situated at high θ, while ADB 2 and 4 are at low θ.
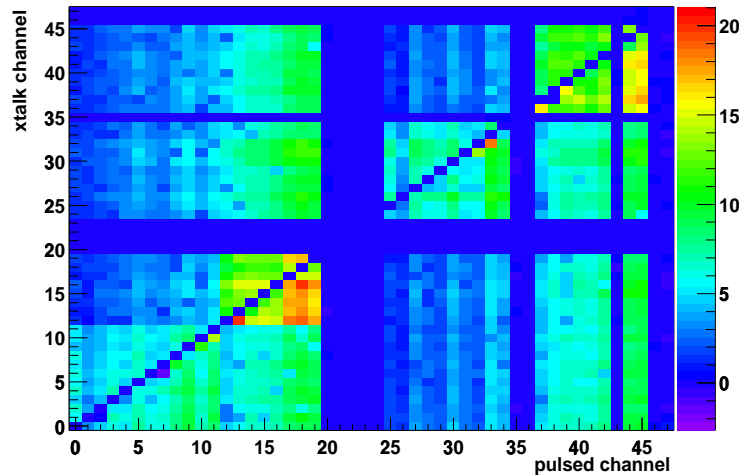
Figure 3.13: Measured Δ_2 in the endcap minicrate channels for different pulsed channels within the minicrate. The pulsed and readout channels are numbered between 0-47, and are grouped in sets of 12 representing each ADB within the minicrate. Only 41 of the channels are instrumented. The crosstalk is measured in ADC counts and the pulsed channel's value has been set to zero.

Figure 3.13 shows the magnitude of Δ_2 induced in the endcap minicrate by different

pulsed channels. Once again we see that the largest signals are seen within the pulsed ADB, but that Δ_2 is typically far smaller than that seen in the barrel. ADB 2 and 4 show the largest signals and a channel pulsed within one of these ADB's generates significant Δ_2 signals in all the other ADB's. Pulsed channels in ADB 1 and 3 generate smaller Δ_2 signals both in their own ADB's and in the other ADB's of the minicrate module. While it was certainly true that the signals were largely contained within the pulsed channel's ADB for the barrel module, it is not true for the endcap. As with the Δ_1, the maximum effect is seen in the low θ ADB's (2 and 4).
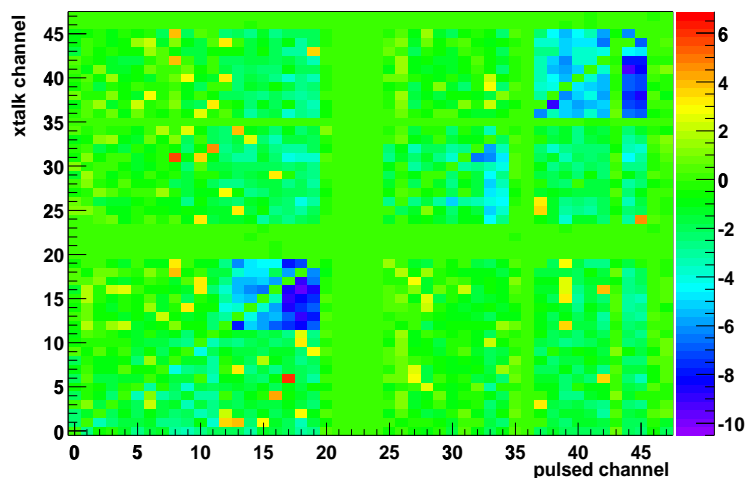
Figure 3.14: Magnitude of Δ_3 in the endcap minicrate channels for different pulsed channels within the minicrate. The pulsed and readout channel are numbered between 0-47, and are grouped in sets of 12 representing each ADB within the minicrate. Only 41 of the channels are instrumented. The crosstalk is measured in ADC counts and the pulsed channel's value has been set to zero.

Figure 3.14 shows the magnitude of Δ_3 within the endcap minicrate. As with the barrel Δ_3 is much smaller than Δ_1 or Δ_2. Most channels show no measurable induced signals, but in ADB 2 and 4 we see negative effects when a channel in these ADB's is pulsed. Again these are the ADB's that have shown the largest signals in Δ_1 and Δ_2 and are situated at low θ. Apart from that effect the rest of the Δ_3 signals are negligible.

From the endcap measurements, it is possible to pick out the following general trends:

1. Peak induced crosstalk within the endcap is significantly smaller than that seen within the barrel

2. Crosstalk within the endcap effects all channels

3. The crosstalk appears to be bigger for crystals pulsed within ADB's serving low θ sections of the endcap

4. Crosstalk is maximal in the crystals read out by the same ADB as the pulsed channel

5. Δ_1 signals are maximum in the nearest neighbours to the pulsed channel, but are negligible in the other channels within the same ADB

6. Significant, and almost constant, signals are seen in the channels of the unpulsed ADB's both in Δ_1 and Δ_2.

7. There is no coherent structure to the signal seen within the pulsed ADB for Δ_2, the nearest neighbour channel does not necessarily see the greatest effect

8. For Δ_3, the ADB's at low θ show negative induced crosstalk pulses for channels within their ADB.

It is clear from these findings that the endcap measurements show a significantly more complicated structure than those of the barrel. As we did not have the opportunity to take further measurements on the endcap it is difficult to make definite statements about the nature of the crosstalk. One of the reasons for this complexity could be related to the cabling structure. Just as the barrel crosstalk seemed related to the neat and definite cabling so might that seen in the endcap. Because of the geometrical structure of the endcap, the cabling is far less regular in pattern than the barrel. The crosstalk seen in the barrel points to the cabling playing a significant role in the generation of crosstalk. The consensus from people involved in the construction of the endcap was that there was no regular pattern or structure to the cabling within the endcap modules, and that each one was likely to give different effects.

As the crosstalk within the endcap was significantly smaller than that of the barrel, and the endcap crosstalk was likely to vary significantly from minicrate to minicrate, it was decided to ignore the endcap and concentrate on the barrel corrections.

3.5.3   Consistency of the data across the detector

We managed to take two full sets of measurements for barrel minicrates, one for the forward barrel and one for the backward barrel. There are several key differences between the measurements, the most notable being that the forward barrel contains predominately low gain preamplifiers while the backward barrel contains high gain preamplifiers. The different gains for the preamplifiers means they saturate in the $\times 32$ range at different energies. Additionally the ADC pulse heights of the crosstalk seen in the unpulsed channels cannot be compared directly, but the ratio of the two preamplifier gains must be factored in. To make any comparison between the measurements it is therefore necessary to take all these factors into account.

To make the comparison between the measurements we analyse the stability of each individual crosstalk measurement between the two sets of minicrate module measurements. Each pulsed channel in each module produces 71 crosstalk measurements in the other channels of the module. These measurements can then be compared on a crystal by crystal basis. As with the previous section we can make these comparisons for Δ_1, Δ_2 and Δ_3. We determine at this stage that Δ_3 is negligible in comparison to Δ_1 and Δ_2 so we choose to ignore it.

There are also two aspects to the crosstalk pulse that must be considered. Firstly the magnitudes of Δ_1 and Δ_2 need to be compared, but also the energy at which the pulsed channel produces the crosstalk pulse must be consistent between the two measurements so that any correction can be consistent across the detector. In terms of the description of Δ_1 and Δ_2 given in section 3.4.1 and in figure 3.6 we can define two variables to describe the energy at which the pulsed channel causes the effect seen in Δ_1 and Δ_2. We define:

1. **Pulse 1: The DAC value at which the $\times 32$ range begins to saturate, given by coordinate x_2 in figure 3.6.**

2. **Pulse 2: The DAC value at which the $\times 32$ has fully saturated, given by coordinate $x_3 - x_2$ in figure 3.6.**

As was the case with Δ_1, Δ_2 and Δ_3, the following analysis uses the definitions of Pulse 1 and Pulse 2 extensively. To make the formal comparison of the stability of the data we did the following:

1. Taking each corresponding pulsed channel in the two barrel minicrates, we find the average of Δ_1 from the two sets of measurements. We do the same for Δ_2 also.

2. We follow the same procedure for the values of Pulse 1 and Pulse 2.

3. The stability comparison is made by forming the ratio of the measurements made in the forward barrel, to the average of the forward and backward barrel measurements. This is done for the measurements of Δ_1, Pulse 1, Δ_2 and Pulse 2.

While we could have compared the ratio of the two measurements directly, rather than comparing the forward barrel measurements to the averaged barrel results, we went with the averaged methodology as it was hoped that we might obtain more measurements with which to make the comparison. In the event this wasn't possible. In making the comparison between the two sets of minicrate measurments, it was important to only include genuine crosstalk pulses. The studies of the magnitudes of Δ_1 and Δ_2 show that each pulsed channel only produces crosstalk in channels within its ADB and in a few other channels within the minicrate. The majority of the channels in the minicrate register nothing except electronics noise fluctuations. These spurious readings should not be compared, so a minimum ADC count is applied to both Δ_1 and Δ_2 to remove these and so leave genuine pulses.
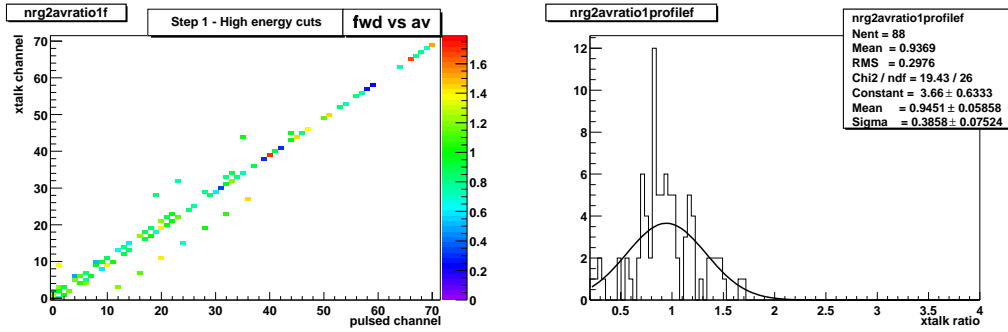
Figure 3.15: The ratio of the forward barrel Δ_1 measurements to the averaged barrel Δ_1 measurements. The left plot shows which readout channels see induced signals from the different pulsed channels within the minicrate, while the right hand plot shows the raw distribution of the ratios with a Gaussian fit overlayed. A minimum Δ_1 threshold is applied to get rid of fake signals due to noise and individual failed calibrations.

Figure 3.15 shows the compatibility of the Δ_1 measurements between the forward barrel and the averaged barrel measurements. A minimum Δ_1 value cut is applied to remove possible signals from electronics noise. There appears to be relatively good agreement between the respective measurements for low numbered pulsed channels, while the agreement gets worse for the higher numbered channels. The lower numbered channels are in the ADB's furthest away from the electronics, which have the greatest values for Δ_1. It makes sense that these measurements are not as affected by noise as the lower Δ_1 measurements from the ADB's close to the front end electronics. The profile of the ratios shows that while the respective measurements are compatible, the agreement is not very good for some of the channels.

Figure 3.16 shows the ratio of the measured Pulse 1 between the forward barrel and the averaged barrel measurements for signals that pass the minimum Δ_1 value discussed above. We can see from both plots that while the magnitude of Δ_1 does not agree too well between the different barrel minicrate measurements, the value of Pulse 1 measured shows very good agreement. The profile plot is centered on 1 and has a very good resolution. This means that although we do not fully understand the nature of the crosstalk before the $\times 32$ saturates, the point at which the $\times 32$ begins to saturate is very well understood.

Figure 3.17 shows the compatibility of the Δ_2 forward barrel and the averaged
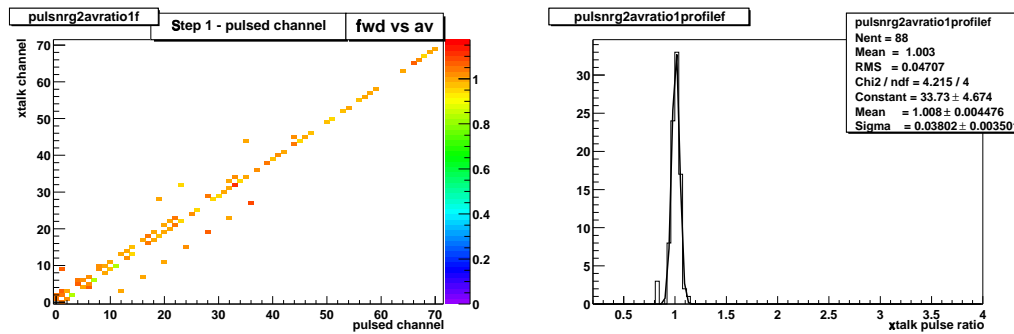
Figure 3.16: The ratio of the forward barrel Pulse 1 measurements to the averaged barrel Pulse 1 measurement. The left plot shows which readout channels see induced Δ_1 signals from the different pulsed channels within the minicrate, while the right hand plot shows the raw distribution of the ratios with a Gaussian fit overlayed. A minimum Δ_1 threshold is applied to get rid of fake signals due to noise and individual failed calibrations.
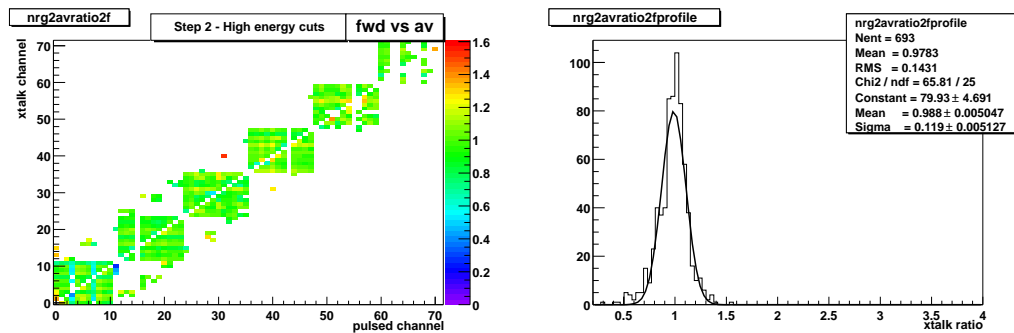
Figure 3.17: The ratio of the forward barrel Δ_2 measurements to the averaged barrel Δ_2 measurements. The plot shows which minicrate readout channels see induced signals from the different pulsed channels within the minicrate. A minimum Δ_2 cut is applied to get rid of fake signals due to noise and individual failed calibrations.

barrel Δ_2 measurements. A minimum Δ_2 cut is applied to remove possible fake background measurements and we can see that this preferentially selects the highest Δ_2 measurements within the pulsed channels ADB. The agreement between the two barrel measurements is significantly better than for Δ_1 and we see the raw profile plot of the ratios shows a well behaved Gaussian distribution with a reasonable width. This is encouraging as it shows that there is relatively good agreement between the forward and backward barrel modules.

Figure 3.18 shows the ratio of the measured Pulse 2 for the forward barrel mea-
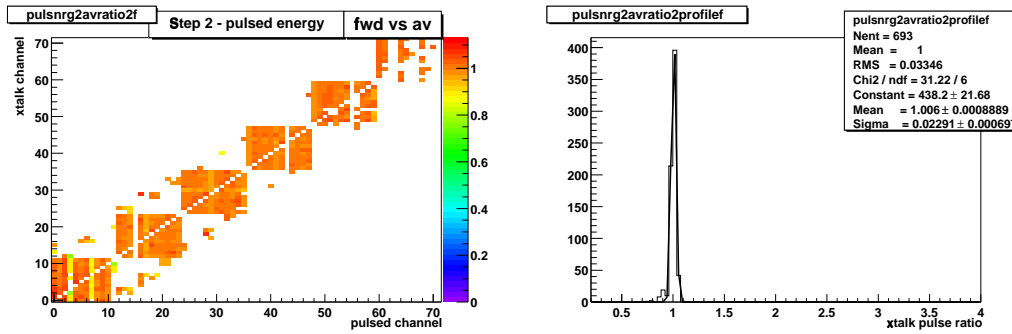
Figure 3.18: The ratio of the forward barrel Pulse 2 measurements to the averaged barrel Pulse 2 measurements. The plot shows shows which minicrate readout channels see induced signals from the different pulsed channels within the minicrate. A minimum Δ_2 energy cut is applied to get rid of fake signals due to noise and individual failed calibrations.

surements and the measured Pulse 2 for the averaged barrel measurements. This effectively marks the end point of the energy required to fully saturate the $\times 32$ range. We can see from both plots that as with Pulse 1, there is very good agreeement between the two barrel sets of measurements. This means that to a good precision we understand what pulse energy is required to begin saturating the $\times 32$ range and what pulse energy is required to fully saturate the $\times 32$ range.

The validation of the measured crosstalk for the barrel measurements produced mixed results. For the dominant Δ_2 effect we see good agreement from the validation process, while for the smaller Δ_1 it is not possible to confidently say that the effect is well understood. We therefore focus the correction to the electronics calibration on the dominant Δ_2 effect generated when the $\times 32$ range begins to saturate in the pulsed channel.

3.6   Correction to the Electronics calibration

The full electronics calibration pulses all channels simultaneously. Consequently all the channels reach the $\times 32$ saturation point at the same time, and so create maximal crosstalk in all other channels. To avoid crosstalk in the calibration, one would ideally pulse each channel separately so the response was uniquely known.

calibration curve for one channel (gain 4)
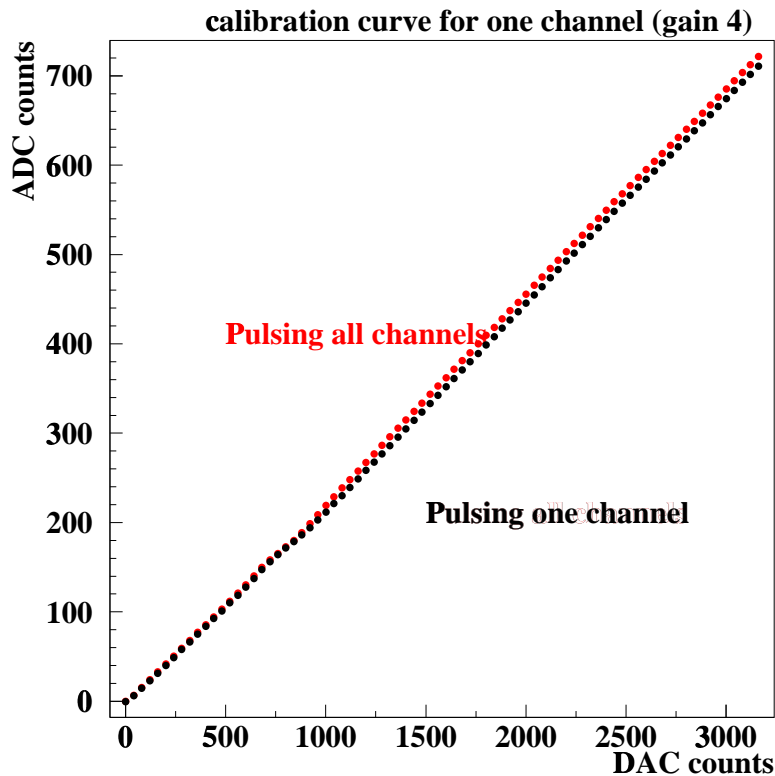
Figure 3.19: The red points show the electronics response for a single channel when a full electronics calibration is performed. The black points show the response of the same channel when only it is pulsed, during the single crystal crosstalk measurements. The data were recorded in the ×4 range and the DAC (x-axis) gives a measure of the injected charge, while the ADC (y-axis) measures the response of the system.

Figure 3.19 shows the response of the same channel during the standard electronics calibration, and from the single crystal measurements taken for the crosstalk study. We can see that at a certain point where the ×32 saturates and crosstalk is created across the system so adding extra ADC counts to the pulsed channels readings. This difference distorts the electronics linearity and so deteriorates the EMC energy resolution.

The key to any calibration correction is that we need to be able to recalibrate the system often, and so take account of the changes that inevitably occur in the system over time. Additionally we need to try and take account of the variation of the crosstalk across the detector.

The correction that was developed for the electronics calibration uses the response of the pulsed crystal from the single crystal measurements, the response from the

odd-even calibrations and the response from the full calibration to build a correction that can be applied to remove the crosstalk from the calibration procedure. The advantage of using the odd-even calibration to derive the correction, instead of a fixed correction, is that the crosstalk varies between individual crystals. The correction was developed for the barrel minicrates and covered the $\times 4$ and $\times 1$ ranges as these were the ones affected by the crosstalk. The range change between the $\times 32$ and $\times 4$ occurs before the $\times 32$ saturates, so the crosstalk is seen in the low energy region of the $\times 4$.

The correction is implemented in the following way:

1. Determine the size of the step induced by the crosstalk for each crystal from the full calibration by subtracting the single crystal measurement from the full calibration measurement. This gives an $all - single$ step.

2. Determine the difference in the step size between the full calibration and the odd-even calibration by subtracting the odd-even calibration from the full calibration for each channel. This gives an $all - odd/even$ step.

3. Linearly transform the measured $all - odd/even$ step size with a factor and an offset so that the $all - odd/even$ step matches the $all - single$ step.

4. Upon performing an electronics calibration, a full and an odd-even calibration are performed. The derived transformation is then applied to the step difference between the full and the odd-even calibration, and then this is subtracted from the full calibration so correcting the electronics response.

The left hand plot in figure 3.20 shows the difference in the crosstalk step for $all - single$ and for $all - odd/even$. The linear transformation is applied to $all - odd/even$ so that good agreement is achieved between the two steps sizes. The right hand plot in figure 3.20 shows the transformed $all - odd/even$ crosstalk pulse which shows good agreement with the $all - single$ crosstalk correction.
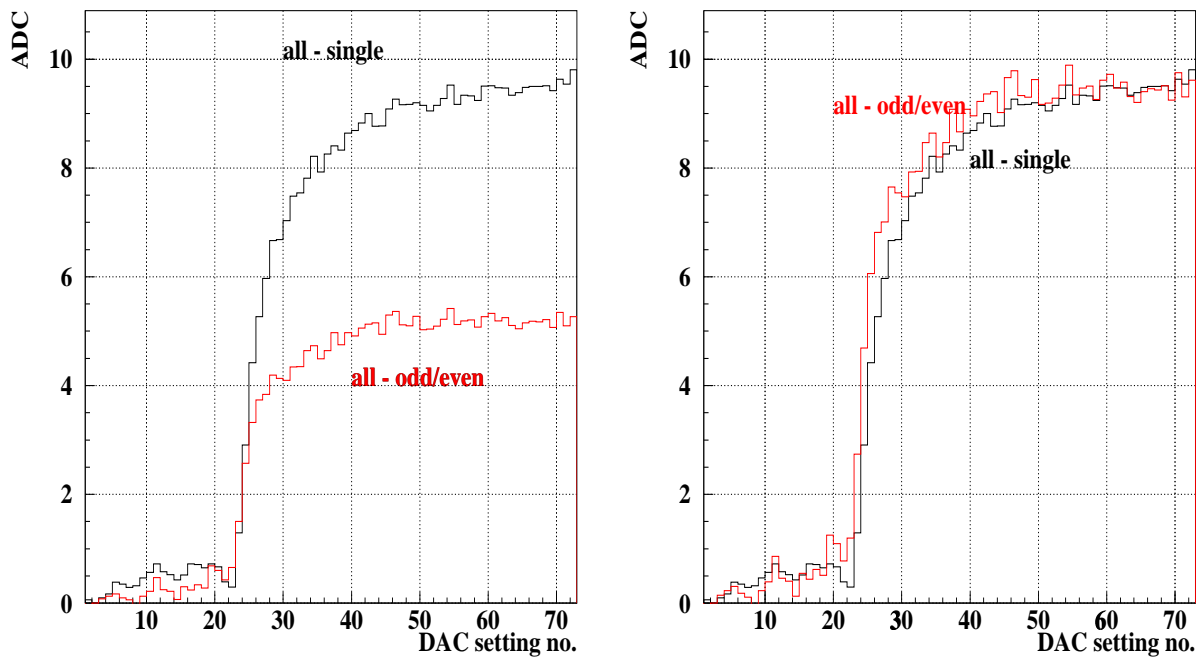
Figure 3.20: The left hand plot shows the raw ADC readout difference for a single channel between an electronics calibration with all channels pulsed and the single crystal measurements (black histogram ($all - single$)), and for all the channels pulsed and an odd-even calibration (red histogram ($all - odd/even$)). The right hand plot shows the difference again once the ($all - odd/even$) measurement has been linearly scaled to match the ($all - single$) response.

Having prepared the transformations for the individual channels within the barrel minicrates, the correction can be applied whenever an electronics calibration is required. The corrected calibration therefore involved taking a full calibration and an odd-even calibration. The difference between the full and the odd-even calibrations is derived for the individual measurements, before scaling is applied. The scaled difference between the full and odd-even calibration is then subtracted from the full calibration to give the corrected calibration.

3.7 Results

The results of the crosstalk correction can be seen in figure 3.21 which shows the single crystal energy spectrum with the non-linearity correction function overlayed. This to be compared with figure 3.1 which shows far greater non-linearities prior to
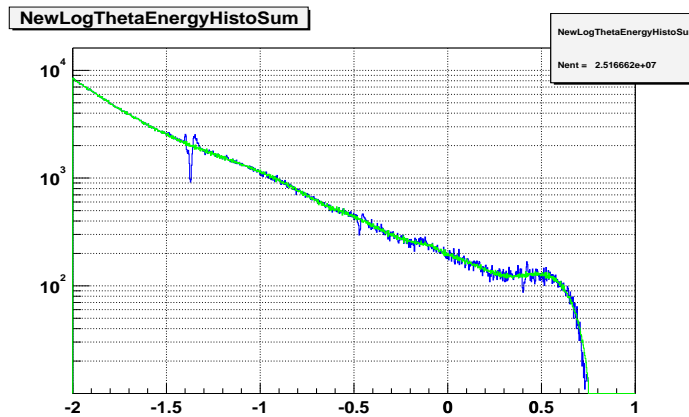
Figure 3.21: The EMC crystal energy spectrum in Run 2 data, a smoothed correction function is overlayed. The x-axis scale is in $\text{Log}_{10}[\text{GeV}]$.

the hardware "ringing" fix and the implementation of the crosstalk correction for the electronics calibration. The ringing correction fixed the largest non-linearities seen in figure 3.1 at -0.45 and 0.45 on the x-axis. The crosstalk correction is effective in limiting the oscillation seen between $(-0.4 - -0.1)$ in figure 3.1 which corresponds to the beginning of the $\times 4$ range.
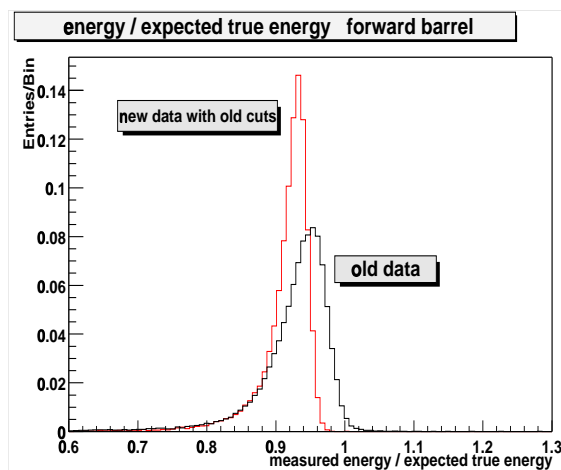
Figure 3.22: The ratio of the measured energy to the expected energy for electrons coming from Bhabha events where the expected energy is well known. The black histogram represents Run 1 data, while the red histogram is Run 2 data. Both are labelled.

The crosstalk correction contributed significantly to improved physics performance

from the EMC in Run 2. The E/p resolution for electrons showed significant improvement also. The reason for this can be seen in figure 3.22 where the ratio of the measured energy to expected energy from Bhabha electrons is shown for Run 1 and Run 2. This shows a great improvement in the energy resolution in the EMC for these electrons shown by the reduced width of the E/p distribution for new data. The figure also shows that the mean of the E/p distribution is shifted for the new data, but this was derived before other calibrations were performed to correct the energy scale.

The π^0 mass resolution in Run 1 and Run 2 is shown in figure 3.23. In Run 1 the resolution was typically 7.0 MeV while in Run 2 this improved to 6.5 MeV. The η mass resolution also improved, going from a typical 18 MeV in Run 1 to 14 MeV in Run 2.

There were many improvements to the EMC between Run 1 and Run 2 so it is impossible to fully quantify the effect of the improved crosstalk-electronics calibration, but it is clear that it helped to significantly improve the performance of the EMC.
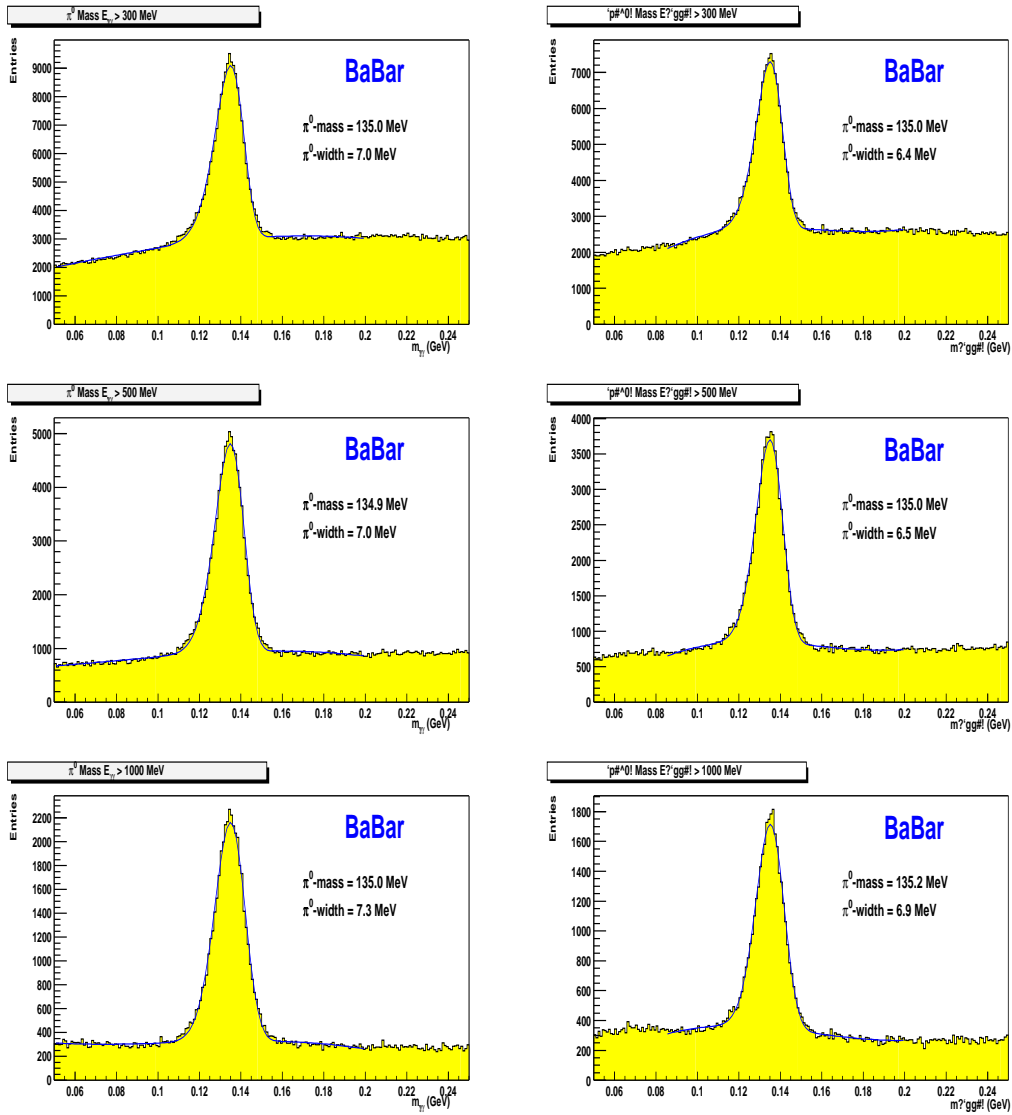
Figure 3.23: The π^0 mass distribution in Run 1 data (left figures) and Run 2 data (right figures) where different cuts on the energy ($E_{\gamma\gamma}$) of the π^0 candidate have been applied. The top figures are for $E_{\gamma\gamma} > 300$ MeV, the central figures are for $E_{\gamma\gamma} > 500$ MeV and the final figure is for $E_{\gamma\gamma} > 1000$ MeV. In each case the π^0 mass distribution has been fitted with a polynomial to represent the background and a Novosibirsk function [33] for the signal π^0's. An improvement of between $(0.4 - 0.6)$ MeV is seen in the π^0 mass resolution between Run 1 and Run 2 data.

Chapter 4

Cut based analysis of $B^0 \to \pi^0\pi^0$

4.1   Introduction

The following three chapters describe an analysis of the decay $B^0 \to \pi^0\pi^0$ at *BABAR*. This chapter begins by describing the initial selection employed to obtain the events of interest for the analysis. The remainder of the chapter describes a simple "cut and count" analysis to extract the branching fraction for $B^0 \to \pi^0\pi^0$. Chapter 5 describes a more sophisticated maximum likelihood analysis which is used to extract the main results of the analysis. Chapter 6 presents the results of the cut and count and the maximum likelihood analysis.

The main challenges for this analysis come from the fact that the expected branching fraction for $B^0 \to \pi^0\pi^0$ is extremely small, $\mathcal{O}(10^{-6})$, and the final state consists of four photons which makes the reconstruction efficiency lower than in related two pion charged modes. Additionally, 2-body charmless decays such as $B^0 \to \pi^0\pi^0$ suffer from significant backgrounds from jet-like light quark (u, d, s, c) production.

The general strategy for the analysis is to use the distinct kinematics of the 2-body decay and the differences in the event shapes for light quark and b-quark production to efficiently reconstruct the $\pi^0\pi^0$ final state while greatly reducing the backgrounds.

Finally the energy constraints on the reconstructed B mesons from production at the $\Upsilon(4S)$ are used to extract the signal decays of interest.

A fuller discussion of the theoretical aspects of the decay and the latest results from *BABAR*, BELLE and CLEO are given in section 1.5.3.

4.2   Data Samples

The data samples used in this analysis represent all that was available at the end of *BABAR* Run 2 and the same data samples as were used for the ICHEP 2002 conference results for $\sin(2\beta)$ [20]. The data were collected from the beginning of *BABAR* running in October 1999 up to the finish of Run 2 in July 2002. The data samples represent "good" runs taken at *BABAR*, where every sub-detector was considered to be performing efficiently and where the data taken could be well understood. While the majority of data collected at *BABAR* were taken at the $\Upsilon(4S)$ resonance, approximately 12.5% are taken at 40 MeV below the resonance, at an energy which is below the threshold for $b\bar{b}$ production. The data samples are summarised below.

- (87.9 ± 1.4) million B^0 decays ($81\,\mathrm{fb}^{-1}$ on-resonance)

- $9.6 \pm 0.2\,\mathrm{fb}^{-1}$ off-resonance

This analysis also uses large samples of Monte Carlo events to simulate backgrounds and, more importantly, the B decay modes that contribute to the analysis. The simulated events are generated using a full GEANT4-based simulation of the detector. The simulations are generated using running conditions and configurations taken from the *BABAR* detector on a monthly basis so as to accurately reflect the changing running conditions. The level of accuracy of the Monte Carlo simulation has been measured by comparing key physics quantities and decay modes that can be accurately validated using the actual data.

The largest sample of Monte Carlo events models the light quark (u, d, s, c) background as well as that from τ production. These samples are combined to form one "continuum" sample which approximately matches the full data sample in terms of the effective luminosity. The cross sections for production of the various quark and lepton types at *BABAR* [35] are listed in table 4.1. The effective luminosities of the Monte Carlo samples are determined using the cross sections shown in this table. The table highlights the fact that although the $b\bar{b}$ cross section is high, there are considerable backgrounds to take into account. Bhabha e^+e^- scattering, which represents the largest cross section, is not simulated as this background is relatively easy to remove within the analysis.

$e^+e^- \rightarrow$	Cross section (nb)
$b\bar{b}$	1.05
$c\bar{c}$	1.30
$s\bar{s}$	0.35
$u\bar{u}$	1.39
$d\bar{d}$	0.35
$\tau^+\tau^-$	0.94
$\mu^+\mu^-$	1.16
e^+e^-	$\approx$40

Table 4.1: Production cross sections at the $\Upsilon(4S)$. The e^+e^- cross section is the effective cross-section within the experimental acceptance.

There are also possible backgrounds from other B decays. To model these, a large sample of simulated B decays are generated which only include decays which do not contain any charm quarks, as these are more likely to provide backgrounds to $B^0 \rightarrow \pi^0\pi^0$. Using this sample it is possible to highlight which B decay modes could provide contributions to the analysis so they can be studied in greater detail. Consequently we also use large Monte Carlo samples of specific charmless B decay modes such as $B^\pm \rightarrow K^\pm\pi^0$, $B^\pm \rightarrow \pi^\pm\pi^0$, $B^\pm \rightarrow \pi^\pm\pi^0\pi^0$ and $B \rightarrow K^*\pi^0$ where the decays contain at least one high energy π^0.

The greatest source of background for the analysis comes from $B^\pm \rightarrow \rho^\pm\pi^0$ as we will see in the coming sections. Consequently we use large Monte Carlo samples for the signal decay $B^0 \rightarrow \pi^0\pi^0$ and for $B^\pm \rightarrow \rho^\pm\pi^0$. These two samples use a

Monte Carlo simulation that has corrections applied to the photon reconstruction so that it better models the neutral reconstruction seen in the data samples. These corrections are documented in section 4.4. The Monte Carlo samples used in the analysis are summarised below.

- $\sim 85\,\mathrm{fb}^{-1}$ each of $u\bar{u}, d\bar{d}, s\bar{s}, c\bar{c}$, and $\tau^+\tau^-$ forming a continuum Monte Carlo sample

- 9.5 million $(180\,\mathrm{fb}^{-1})$ rare charmless $B\overline{B}$ Monte Carlo events

- 145k of signal $B^0 \to \pi^0\pi^0$ Monte Carlo events

- 510k of signal $B^\pm \to \rho^\pm\pi^0$ Monte Carlo events

- 237k of signal $B^\pm \to K^\pm\pi^0$ Monte Carlo events

- 230k of signal $B^\pm \to \pi^\pm\pi^0$ Monte Carlo events

- 38k of signal $B^\pm \to \pi^\pm\pi^0\pi^0$ Monte Carlo events

- 38k of signal $B \to K^*\pi^0$ Monte Carlo events

4.3   Initial Event Selection

The following sections outline the selection procedure that is used to preferentially select $B^0 \to \pi^0\pi^0$ events and to reduce the various backgrounds to reasonable levels prior to the final analysis.

4.3.1   Multi-hadron selection

A series of tags are set within the data reconstruction to define the type of event that has been recorded. Two are used within this analysis and we accept events that pass either of the tags. The first tag is designed to select multi-hadronic events and is primarily designed to remove Bhabha scattering events by requiring more than

two charged tracks in the event. In a decay such as $B^0 \to \pi^0\pi^0$ where one of the B mesons produced contains only neutral particles, there can be a significant number of events where the other B decays to two charged tracks or less. The second tag is used to select multi-neutral events, so that interesting physics events that would be lost by the multi-hadronic selection are retrieved. The details of the two tags are given in table 4.2.

Tag Selector	Selection Criteria applied
Multi-Hadronic	> 2 tracks in the event
Neutral-Hadronic	cluster $= E_{LAB} > 100\,\text{MeV}$ photon $=$ cluster $+ E_{CM} > 500\,\text{MeV}$ tight photon $=$ photon $+ (-0.75 < \|cos\theta_\gamma\| < 0.96)$ 2 tracks: ≥ 3 clusters and ≥ 2 photons 1 tracks: ≥ 4 clusters and ≥ 2 tight photons 0 tracks: ≥ 6 clusters and ≥ 3 photons

Table 4.2: Definitions of the tags used to select hadronic events of interest. The neutral hadronic section begins by defining clusters, photons and tight photons for the purpose of the selector and then following this with the definition of the selection criteria for different numbers of tracks within the event.

An additional tag which is designed to select events that come from 2-body like decays is also used. In the case of $B^0 \to \pi^0\pi^0$, the tag takes combinations of bumps within EMC clusters to form π^0 candidates. The π^0 candidates must have an invariant mass $M_{\gamma\gamma}$ in the range $0.09 < M_{\gamma\gamma} < 0.18\,\text{GeV}$. The π^0 candidates are then combined to create B candidates and are selected if the π^0 momenta in the CM frame are approximately equal and back-to-back, and if the B candidate formed has a mass within $\pm600\,\text{MeV}$ of the actual B mass.

4.3.2 π^0 reconstruction

π^0 candidates are formed by combining pairs of photon candidates which are constrained to originate from the primary vertex of the event. Typically each π^0 forms a cluster within the EMC with two resolved bumps representing each photon from the decay $\pi^0 \to \gamma\gamma$. Clusters with only one bump are considered photons as long as they have an energy less than $1.8\,\text{GeV}$. All clusters with only one bump and

an energy greater than 1.8 GeV are considered to be merged π^0's (high energy π^0's where the decay produces two co-linear photons which cannot be resolved within the EMC). For this analysis only composite π^0's, those that are formed by combinations of resolved photon pairs, are used and the merged π^0 candidates are ignored. The primary reason for this is the uncertainty in the merged π^0 reconstruction efficiency. This is not a large loss as the $B^0 \to \pi^0\pi^0$ Monte Carlo shows that less than 10% of signal events have one or more merged π^0's. Additionally each photon must have an energy greater than 30 MeV so as to remove the possibility of using spurious low energy background photons in the π^0 reconstruction.
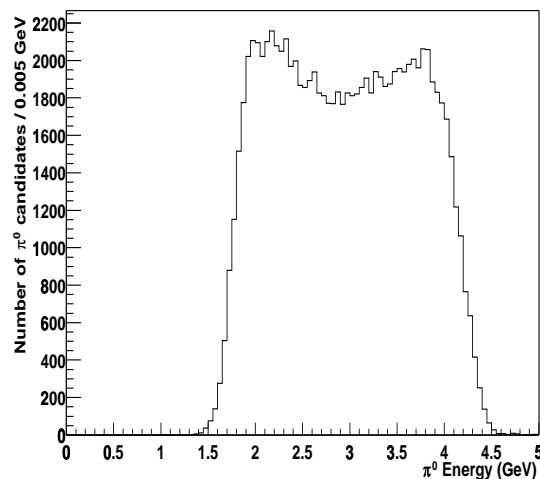
Figure 4.1: The Monte Carlo π^0 energy spectrum in the laboratory frame for π^0's coming from $B^0 \to \pi^0\pi^0$ signal events.

As $B^0 \to \pi^0\pi^0$ is a 2-body decay, the π^0's are of high energy when compared to those produced in more common high multiplicity decay modes. Figure 4.1 shows the energy spectrum in the laboratory of the π^0's seen in signal Monte Carlo events. We select candidates with $E_{\pi^0} > 1.0$ GeV which removes the vast majority of all π^0 candidates whilst retaining all those from $B^0 \to \pi^0\pi^0$ decays. We use two variables to reject fake π^0's. Firstly the cluster's lateral moment (LAT) which is defined as:

$$LAT = \frac{\displaystyle\sum_{i=3}^{M} E_i r_i^2}{\displaystyle\sum_{i=3}^{N} E_i r_i^2 + E_1 r_0^2 + E_2 r_0^2} \tag{4.1}$$

where N is the number of crystals associated with the EMC shower, E_i is the energy deposited in the i-th crystal, where they are numbered such that $E_1 > E_2 > ... > E_N$, r_i and ϕ_i are the polar coordinates in the plane perpendicularr to the line pointing from the interaction point to the shower centre and r_0 is the average distance between two crystals. The LAT varies between 0-1 and tends to very low or very high values for fake photon candidates within the calorimeter. We therefore select photons which satisfy $0.01 <$ LAT < 0.60 which is almost 100% efficient for true photons.
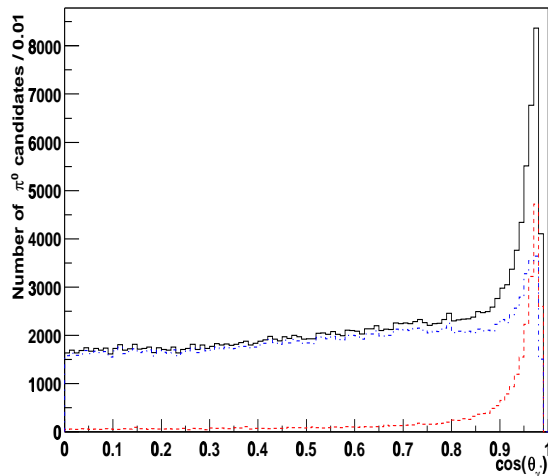
Figure 4.2: Angular distribution for π^0's from continuum Monte Carlo events. The solid histogram represents the distribution for all reconstructed π^0's while the red (dashed) histogram is for those within the sample without a π^0 truth match, and the blue (dashed-dot) histogram is for those with a truth match.

The second variable useful for removing fake π^0 candidates is $\cos(\theta_{\gamma^*})$, the angle between the photon momentum in the π^0 rest frame and the π^0 momentum in the laboratory frame. This angle is relatively flat for true π^0 candidates but is strongly peaked at one for fake candidates as is shown in figure 4.2. We select
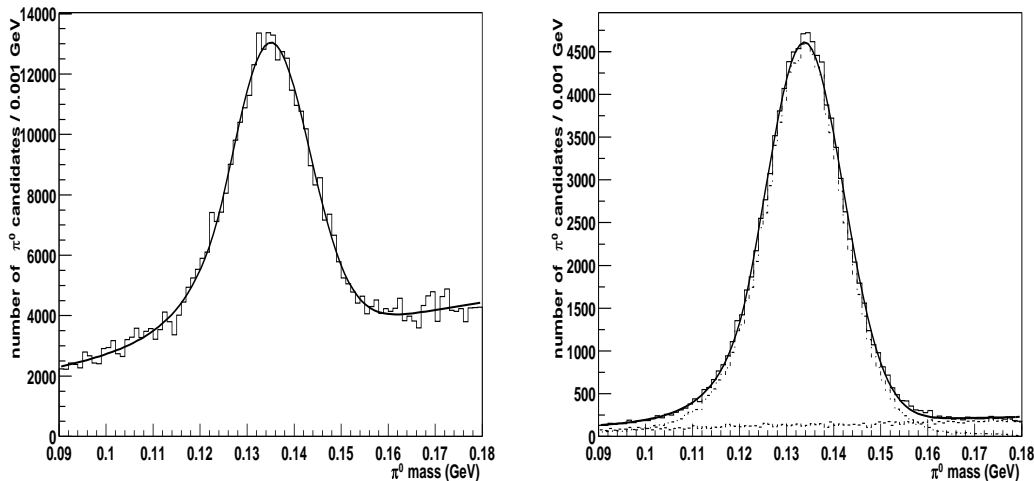
Figure 4.3: The π^0 mass distribution for data (left) and signal Monte Carlo events (right). Both distributions are fitted with a Crystal Ball function [34] for signal and a polynomial describing the background. The Monte Carlo event distribution additionally shows the contribution from truth-matched π^0's (dotted histogram) and combinatorics (dashed histogram). The fitted resolution for data is 8.5 MeV and for the signal Monte Carlo it is 8.4 MeV. The Crystal Ball function is used as it combines a central Gaussian with an exponential describing the radiative tail of the distribution.

$|\cos(\theta_{\gamma*})| < 0.95$ to remove the majority of the combinatoric fake π^0 candidates while retaining good signal efficiency.

Figure 4.3 shows the π^0 mass distributions in data and $B^0 \to \pi^0\pi^0$ Monte Carlo events for π^0's matching the kinematic selections already outlined in this section ($E_{\pi^0} > 1.0\,\mathrm{GeV}, E_\gamma > 30.0\,\mathrm{MeV}$). As the π^0 candidates are higher energy than typical π^0's at *BABAR* the mass resolution is slightly greater also. In data we have a π^0 mass resolution of 8.5 MeV while in the Monte Carlo the resolution is 8.4 MeV. We use a wide mass window to select good π^0 candidates with $0.11 < M_{\gamma\gamma} < 0.16\,\mathrm{GeV}$. A summary of the π^0 selection criteria is given below:

- Two Resolved photons (i.e not merged π^0)

- $E_\gamma > 30.0\,\mathrm{MeV}$ for both photons

- $0.01 < \mathrm{LAT} < 0.60$ for both photons

- $E_{\pi^0} > 1.0\,\mathrm{GeV}$

- $|\cos(\theta_{\gamma^*})| < 0.95$

- $0.11 < M_{\gamma\gamma} < 0.16\,\mathrm{GeV}$.

4.3.3 Event shape variable selection

Further initial selection is given by using event shape variables to select multi-hadronic events and to suppress the backgrounds. As B mesons from the $\Upsilon(4S)$ are produced at the kinematic limit, the B's are almost at rest in the CM frame. Their subsequent decays tend to be isotropic in nature, compared to the more jet-like shape of lighter quark production. There are several variables that can be employed to characterise these event shapes. The first variables used are the Fox-Wolfram [36] moments which are defined as

$$F_l = \sum_{i,j} \frac{|\mathbf{p_i}||\mathbf{p_j}|}{E_{vis}^2} P_l(\cos\theta_{ij}) \qquad (4.2)$$

where P_l are the Legendre polynomials, $\mathbf{p_i}$ is the momentum for particle i, θ_{ij} is the opening angle between particles i and j, and E_{vis} is the total visible energy of the event. The Legendre polynomials of interest here ($l = 0$ or 2) are given by

$$P_0 = \frac{1}{2}, \qquad P_2 = \frac{1}{2}[3\cos^2(\theta_{ij}) - 1] \qquad (4.3)$$

so that the second Fox-Wolfram moment ratio is effectively given by

$$R_2 = \frac{F_2}{F_0} = 3\sum_{i,j} \frac{|\mathbf{p_i}||\mathbf{p_j}|}{E_{vis}^2}[\cos^2(\theta_{ij}) - 1]. \qquad (4.4)$$

R_2 as defined here varies between (0-1); R_2 is 0 for a perfectly spherical event, while R_2 is 1 for an event completely collimated about the jet axis. Our initial selection requires that $R_2 < 0.95$ for the whole event.

The second variable used is the sphericity [37] which is defined as:

$$S = \frac{3}{2}(\lambda_2 + \lambda_3) \qquad (4.5)$$

where λ_2 and λ_3 are the two minor eigenvalues of the diagonalised sphericity tensor

$$S^{\alpha\beta} = \frac{\sum_i p_i^\alpha p_i^\beta}{\sum_i \mathbf{p_i^2}} \tag{4.6}$$

where $\alpha, \beta = 1, 2, 3$ corresponding to the x, y, z components of the momentum $\mathbf{p_i}$ of particle i in the event sample. The range of the sphericity variable is (0-1) and events that are highly directional such as jet-like light quark production have low values of sphericity, while more isotropic events such as B decays have higher values of sphericity. Initial selection is given by selecting events with $S > 0.01$. The sphericity axis of this system is defined by the direction of the eigenvector corresponding to the largest eigenvalue. A fuller description of both the Fox-Wolfram moments and sphericity in relation to B event selection at *BABAR* is given in [35].

Using the sphericity axis we can form a very effective variable to distinguish signal events from light quark continuum production. For decays involving true B candidates, each B decay within the event should be uncorrelated from the other. Therefore if we correctly reconstruct the signal $B^0 \to \pi^0\pi^0$ decay, its sphericity axis should be uncorrelated with the sphericity axis of the rest of the event. Candidates formed from jet-like light quark events should show a high correlation to the rest of the event as they are part of the same fragmentation procedure and the momentum of the decay products tend to sit along a common axis.

In the CM, we therefore take the two π^0 particles used to reconstruct the B and form their sphericity axis. We also form the sphericity axis for all the other tracks and neutral particles in the event. Taking the dot product of the two axes gives the variable $\cos(\theta_S)$. Figure 4.4 shows the distribution of $|\cos(\theta_S)|$ for signal and continuum. Signal events show a flat uncorrelated distribution as we would expect for the two B mesons. Continuum events show a sharp peak at small angles showing a high degree of correlation between the reconstructed B and the rest of the event. We apply an initial selection cut at $|\cos(\theta_S)| < 0.9$ to reduce the levels of continuum background.

We use one more event shape based variable in the final stages of the analysis. We form a Fisher discriminant [38] ($\mathcal{F}$) based on the Legendre polynomials given by
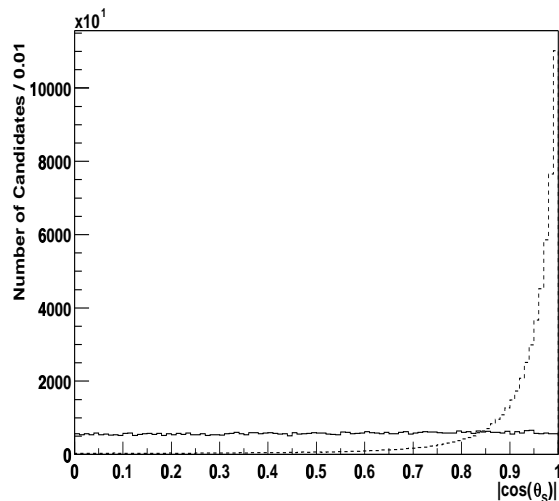
Figure 4.4: The distributions for $B^0 \to \pi^0 \pi^0$ (solid) and continuum (dashed) Monte-Carlo events for the angle between the sphericity axis of the reconstructed B and the sphericity axis of the rest of the event in the CM. Each sample is normalised to the same number of events.

equation 4.3 which are defined using only the tracks and clusters in the rest of the event, so excluding the two π^0's forming the B. The discriminant is optimised to provide separation between signal B events and continuum. The process by which the discriminant was developed and tested is described in detail elsewhere [39]. The final form of the Fisher discriminant is given by

$$\mathcal{F} = 0.5319 - 0.1790 L_0 + 0.8465 L_2 \tag{4.7}$$

where L_0 and L_2 are variables similar to the Legendre polynomials and defined as:

$$L_0 = \sum_i^{roe} p_i, \qquad L_2 = \sum_i^{roe} p_i \times \frac{1}{2}(3\cos^2(\theta_i) - 1) \tag{4.8}$$

where p_i and θ_i are the momentum and polar angle of tracks and clusters summed over candidates in the rest of the event(roe), those not associated with signal π^0 decays. Figure 4.5 shows the $\mathcal{F}$ distributions for Monte Carlo signal and background data events. The discriminating power of $\mathcal{F}$ comes from the difference between the spherical nature of true B decays as compared to the jet-like continuum production. No cut on the $\mathcal{F}$ discriminant is made at this stage of the analysis, but $\mathcal{F}$ is used extensively for final selection in both the cut and count and maximum likelihood based analyses.
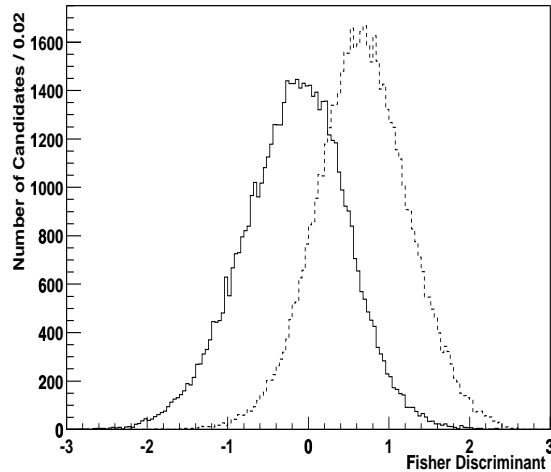
Figure 4.5: The distributions for $B^0 \rightarrow \pi^0\pi^0$ (solid) Monte Carlo events and on-resonance (dashed) events for the Fisher discriminant. The on-resonance sample is selected from regions in the reconstucted B mass that contain few signal events and the two samples are normalised to the same number of events.

4.3.4   Reconstructed B kinematics

Two kinematic variables are used for the final selection of events. Both make use of the fact that for genuine B events, the reconstructed energy in the CM frame of the candidate should be the same as the beam energy. While reconstructing the energy of the candidate from the measured energies within the detector gives a poor resolution, we have a very good energy resolution for the beam energies. The two variables are the *beam energy substituted mass* (m_{ES}), and the energy difference (ΔE). The variables are defined as

$$m_{ES} = \sqrt{\frac{(s/2 + \mathbf{p_0} \cdot \mathbf{p_B})^2}{E_0^2 - p_B^2}}, \qquad \Delta E = E_B^* - \sqrt{s/2} \qquad (4.9)$$

where E_B^* is the B meson candidate energy in the CM system, E_0 and $\sqrt{s}$ are the total energies of the e^+e^- system in the laboratory and CM systems respectively and $\mathbf{p_0}$ and $\mathbf{p_B}$ are the three-momenta of the e^+e^- and the B candidate in the laboratory frame. m_{ES} effectively reconstructs the B mass using the beam energy instead of the reconstructed B candidate energy, while ΔE represents the difference

between the beam energy and the reconstructed B energy. Further details regarding the derivations and physical principles which make m_{ES} and ΔE useful variables can be found elsewhere [40].
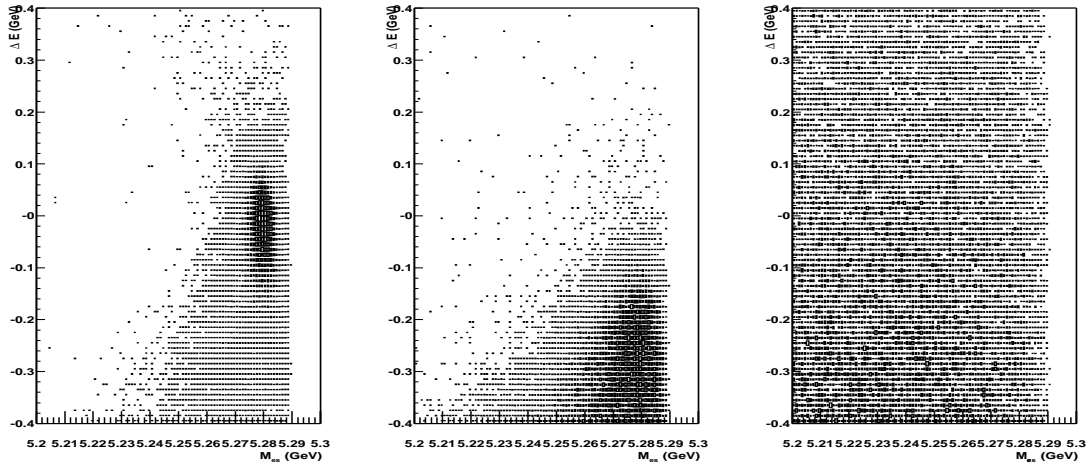
Figure 4.6: The $m_{ES} : \Delta E$ plane for $B^0 \to \pi^0 \pi^0$ (left), $B^\pm \to \rho^\pm \pi^0$ (centre) and continuum Monte Carlo events (right).

Figure 4.6 shows the m_{ES}:ΔE plane for $B^0 \to \pi^0 \pi^0$, $B^\pm \to \rho^\pm \pi^0$ and continuum Monte Carlo background events. For the signal $B^0 \to \pi^0 \pi^0$ mode we see that m_{ES} is centred around the B mass and at $\Delta E = 0$. There are significant tails in the m_{ES} and ΔE distributions corresponding to missing energy in the reconstruction which is primarily due to reconstructing a fully neutral final state. The calorimeter tends to lose energy in the reconstruction due to leakage of showers or light through the back of the crystals or through showering in the material immediately in front of the EMC. The $B^\pm \to \rho^\pm \pi^0$ distribution is shifted to lower values of ΔE and has a greater spread in both m_{ES} and ΔE than for the $B^0 \to \pi^0 \pi^0$ mode. This is due to missing a soft $\pi^\pm$ in the reconstruction. For continuum events we see a relatively flat distribution across both m_{ES} and ΔE. The CM kinematic limit of $5.29\,\mathrm{GeV}$ is evident in the m_{ES} distribution. Initial cuts of $5.20 < m_{ES} < 5.29\,\mathrm{GeV}$ and $|\Delta E| < 0.4\,\mathrm{GeV}$ are used to select events of interest. Both m_{ES} and ΔE are used extensively in final signal selection in both the cut and count and maximum likelihood based analyses.

4.3.5   Final cuts and efficiency summary

Data	Selection Criteria					
Sample	Original	Hadronic	π^0 quality	$|\cos(\theta_S)|$	m_{ES} & ΔE	Efficiency
$\pi^0\pi^0$ MC	145K	213,757	45,471	40,484	38,742	26.7%
$\rho^\pm\pi^0$ MC	510K	222,276	52,375	46,379	27,087	5.3%
$K^\pm\pi^0$ MC	237K	136	69	37	18	0.008%
$K^*\pi^0$ MC	38K	21	4	0	0	0%
$\pi^\pm\pi^0\pi^0$ MC	38K	730	522	467	210	0.5%
$\pi^\pm\pi^0$ MC	230K	145	62	23	7	0.005%
Charmless MC	9.5M	3,082	1,293	1,024	505	0.005%
Continuum MC	300M	781,542	299,896	76,374	24,104	0.008%
Off-resonance	-	86,455	31,122	10,347	2,426	-
On-resonance	-	767,119	257,037	81,252	24,534	-

Table 4.3: The efficiencies for the different Monte Carlo and data samples with the pre-selection cuts described in the text applied.

Table 4.3 shows the efficiencies for the different data samples as each set of selection criteria are applied. It is worth noting how effective the π^0 and event shape selection are in reducing combinatorics and background events. The final $B^0 \to \pi^0\pi^0$ efficiency having applied these pre-selection cuts is 26.7% and the final data sample contains 24,534 events. While most of the potential backgrounds from other B decay modes have a negligible efficiency, $B^\pm \to \rho^\pm\pi^0$ presents a significant background. As a significant fraction of the $B^\pm \to \rho^\pm\pi^0$ events have two high energy π^0's these events can form good $B^0 \to \pi^0\pi^0$ candidates. The efficiency of 5.3% coupled with an expected branching fraction of $\mathcal{B}(B^\pm \to \rho^\pm\pi^0) = 2 \times 10^{-5}$ means that we could expect a large number of these events in our sample. From the charmless Monte Carlo sample, this was found to represent the only significant B related background and is the only one we take into account in the rest of the analysis.

4.4   Neutrals Correction

The Monte Carlo samples used for $B^0 \to \pi^0\pi^0$ and $B^\pm \to \rho^\pm\pi^0$ have had a "neutrals correction" applied to them in the reconstruction. It has been found that the

standard *BABAR* Monte Carlo simulation shows discrepancies in the reconstruction of all the neutral particles when compared to actual data. The Monte Carlo simulation effectively performs too well, with better resolutions and efficiencies than can actually be achieved. The derivation and implementation of the correction is outlined below and is discussed in detail elsewhere [41].

The correction factor is obtained from the study of tagged τ decays from $e^+e^- \rightarrow \tau^+\tau^-$ where one of the τ's decays into a lepton and two neutrinos (the tagged side). The other τ can decay to $h(N\pi^0)\nu$ where h is a charged pion or kaon, and we can have N as either one or two π^0's. The ratio of Data/MC for the $2\pi^0/1\pi^0$ final states gives an overall correction factor, which is applied by randomly killing photons in the Monte Carlo events so the efficiencies match. Only clusters that contain more than one bump have the killing factor applied. Additional photon energy smearing is also applied so that the π^0 mass resolution and photon energy spectrum match between data and Monte Carlo events. The effect of the smearing can be seen by the good agreeement in π^0 mass resolution for data and $B^0 \rightarrow \pi^0\pi^0$ Monte Carlo events shown in figure 4.3. The validity of the corrections has been tested by various comparisons between data and corrected Monte Carlo events.
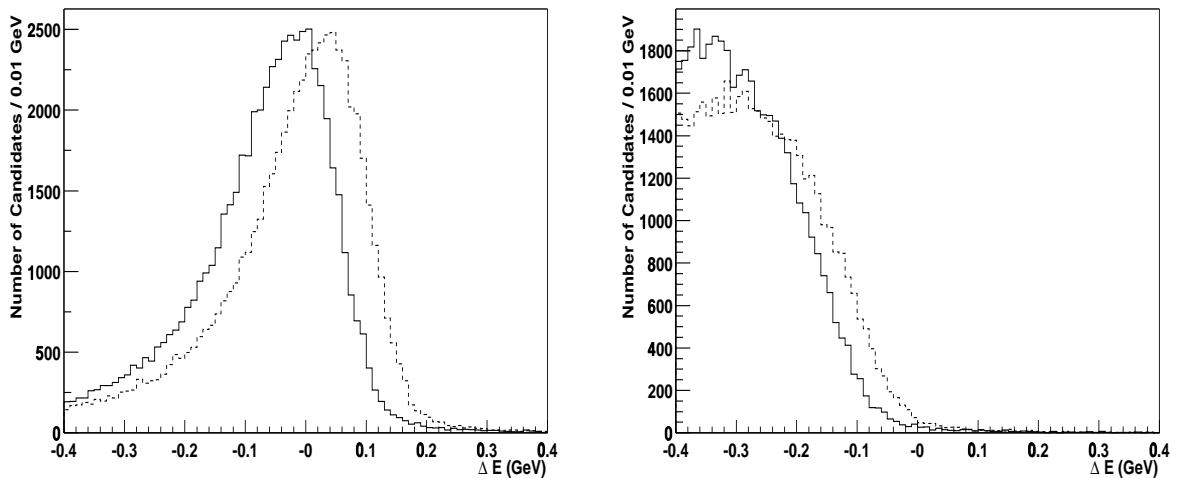
Figure 4.7: The effect of the neutral correction recipe on the ΔE distribution for $B^0 \rightarrow \pi^0\pi^0$ (left) and $B^\pm \rightarrow \rho^\pm\pi^0$ (right). The solid histogram represents the corrected distribution, while the uncorrected is shown in the dashed histogram. The distributions have been normalised to the same number of events.

The killing and smearing has a large effect on the signal and $B^{\pm} \to \rho^{\pm}\pi^0$ efficiency with just 70% of the original Monte Carlo events surviving. Once again it must be noted that the corrected Monte Carlo events were used for all the numbers and efficiencies given in table 4.3 for $B^0 \to \pi^0\pi^0$ and $B^{\pm} \to \rho^{\pm}\pi^0$ and throughout this analysis. While the smearing and killing decreases the final selection efficiency for $B^0 \to \pi^0\pi^0$ and $B^{\pm} \to \rho^{\pm}\pi^0$ Monte Carlo events, it initially increases the number of events seen from the "Hadronic" selection in table 4.3. This is due to the smearing of low energy photons which increases the number of candidates that are initially reconstructed. The neutrals correction is not well tested at low energies but his effect is removed by the π^0 quality requirements that are then applied.

The effect of the smearing can most clearly be seen in the ΔE distributions for $B^0 \to \pi^0\pi^0$ and $B^{\pm} \to \rho^{\pm}\pi^0$. Figure 4.7 shows the corrected and uncorrected Monte Carlo ΔE distributions for these two B decay modes. For $B^0 \to \pi^0\pi^0$ the mean of ΔE is shifted by approximately $50\,\mathrm{MeV}$ to lower values so that it is no longer centred on zero. The same can be seen in the $B^{\pm} \to \rho^{\pm}\pi^0$ distributions.

4.5   Cut-based Optimisation

4.5.1   Optimisation procedure

While a maximum likelihood (ML) analysis typically gives results that are statistically more significant, a cut-based analysis provides a simple way to confirm any interesting results we see in the fit.

Before optimising, an initial signal region was defined as $-0.20 \leq \Delta E \leq 0.10\,\mathrm{GeV}$ and $5.265 \leq m_{ES} \leq 5.290\,\mathrm{GeV}$. The initial values for ΔE are asymmetric as the $B^0 \to \pi^0\pi^0$ ΔE distribution has a lower energy tail and is centred below zero. Using this starting point, the selection cuts for the upper and lower ΔE values, upper and lower m_{ES} values, $\mathcal{F}$ and $|\cos(\theta_S)|$ variables are simultaneously optimised to maximise the significance of any signal given by $N_S/\sqrt{N_S + N_B}$, where N_S is

the number of signal events and N_B is the number of background events. Even though $\mathcal{F}$ and $|\cos(\theta_S)|$ are highly correlated (see Table 5.1 later), cutting on both variables gives more discrimination of signal over continuum background than just using $\mathcal{F}$. The ranges and step sizes over which each variable was optimised are given in table 4.4.

Variable	Range	Step Size
Upper ΔE value	(0.01 - 0.10) GeV	0.01 GeV
Lower ΔE value	$(-0.20 - -0.05)$ GeV	0.01 GeV
Upper m_{ES} value	(5.283 - 5.290) GeV	0.001 GeV
Lower m_{ES} value	(5.265 - 5.275) GeV	0.001 GeV
$|\cos(\theta_S)|$ value	(0.50 - 0.85)	0.05
$\mathcal{F}$ value	$(-0.8 - 0.8)$	0.1

Table 4.4: The ranges and step sizes for each of the variables used in the optimisation procedure

Continuum background is estimated using an on-resonance[1] 'grand sideband' (GSB) defined by $5.20 \leq m_{ES} \leq 5.25$ GeV and the appropriate cuts in ΔE, $\mathcal{F}$ and $|\cos(\theta_S)|$ for the particular cut configuration. The number of events in the GSB is converted into a number in the signal region using a scaling factor calculated from fitting an Argus function [42][2] to the on-resonance m_{ES} distribution. The Argus shape parameter is determined from the on-resonance data with a cut of $\mathcal{F} > 0.5$ applied so to remove possible $B^0 \to \pi^0 \pi^0$ and $B^\pm \to \rho^\pm \pi^0$ events. The ratio of the integral of the fitted Argus function in the defined signal region and the GSB region is then taken as the scaling ratio R. R is then multiplied by the number of events in the GSB to give the predicted number of continuum events in the signal region. As m_{ES} shows no significant correlation to ΔE, $\mathcal{F}$ or $\cos(\theta_S)$ (Table 5.1) for continuum events, R is only dependent on the cuts applied to m_{ES} and not on the other cuts applied.

The $B^\pm \to \rho^\pm \pi^0$ component in the defined signal region is estimated by assuming a branching fraction of 2.0×10^{-5} (approximately the central value based on a limit of $< 4.3 \times 10^{-5}$ obtained by CLEO [43]). The efficiency is calculated from the

---

[1]On-resonance refers to data taken at the $\Upsilon(4S)$ resoanance
[2]The Argus function is further discussed and defined in section 5.3.2

$B^{\pm} \to \rho^{\pm}\pi^{0}$ Monte Carlo sample with the full set of defined cuts applied. The expected number of $B^{\pm} \to \rho^{\pm}\pi^{0}$ events is then calculated using the efficiency, the expected branching fraction and the number of B mesons that are in our final data sample. The $B^{\pm} \to \rho^{\pm}\pi^{0}$ branching fraction is systematically varied by $\pm 1 \times 10^{-5}$ to reflect our lack of knowledge of this figure. The total background contribution N_B is taken as the sum of the calculated continuum and $B^{\pm} \to \rho^{\pm}\pi^{0}$ components.

The significance $N_S/\sqrt{N_S + N_B}$ is optimised assuming $\mathcal{B}(B^0 \to \pi^0\pi^0) = 2 \times 10^{-6}$, but the stability of the result is checked by also performing the optimisation for $\mathcal{B}(B^0 \to \pi^0\pi^0) = 1, 3$ and 4×10^{-6}. The number of signal events is estimated in the same way as $B^{\pm} \to \rho^{\pm}\pi^{0}$ events; all the selection cuts are applied to the signal Monte Carlo events to obtain the efficiency. The number of events is then calculated using the efficiency, the number of B mesons in the final data sample and the various expected $\mathcal{B}(B^0 \to \pi^0\pi^0)$.

4.5.2   Optimisation results

Selection	Presumed $\mathcal{B}(B^0 \to \pi^0\pi^0)$			
/Details	1×10^{-6}	2×10^{-6}	3×10^{-6}	4×10^{-6}
$m_{ES}(\,\text{GeV})$	5.274 - 5.286	**5.274 - 5.286**	5.273 - 5.285	5.273 - 5.286
$\Delta E(\,\text{GeV})$	-0.16 - 0.08	**-0.16 - 0.08**	-0.16 - 0.10	-0.16 - 0.10
$\mathcal{F}$	< -0.5	$\mathbf{< -0.1}$	< -0.1	< -0.1
$\|\cos(\theta_S)\|$	< 0.5	$\mathbf{< 0.55}$	< 0.55	< 0.65
ϵ_{sig}	5.0%	$\mathbf{(8.20 \pm 0.08)\%}$	8.8%	9.6%
Expected $N_{\pi^0\pi^0}$	4.4	**14.4**	23.3	33.8
Grand sideband events	91	**285**	306	380
GSB-signal scaling ratio	0.1319	$\mathbf{0.1319 \pm 0.0022}$	0.1455	0.1455
Expected continuum	12	$\mathbf{37.6 \pm 2.9}$	44.5	55.3
Expected $N_{\rho^{\pm}\pi^0}$	1.6	$\mathbf{2.7 \pm 1.5}$	2.9	3.6
Expected background	13.6	$\mathbf{40.3 \pm 3.3}$	47.4	58.9
Expected significance	1.08 (1.07)	**2.04**	2.82 (2.81)	3.58 (3.55)

Table 4.5: Summary of the optimal cut and count selection criteria, showing efficiencies and expected levels of background. The final row shows the expected significance for the optimal cuts for each possible branching fractions, in brackets is the expected significance if the optimal cuts for $\mathcal{B}(B^0 \to \pi^0\pi^0) = 2 \times 10^{-6}$ are used instead.

Table 4.5 shows the results of the optimisation procedure for the different branching

fractions of $B^0 \to \pi^0\pi^0$. For $\mathcal{B}(B^0 \to \pi^0\pi^0) \geq 2 \times 10^{-6}$, we see that the optimal set of cuts are very consistent. For $\mathcal{B}(B^0 \to \pi^0\pi^0) = 1 \times 10^{-6}$ the optimal cuts remove far more continuum background than for the other optimised values, mainly due to the $\mathcal{F}$ cut. Because the expected number of signal events increases as the input signal branching ratio increases, so the optimised cuts become looser, allowing more continuum background events.

The selected optimisation is given by the results for $\mathcal{B}(B^0 \to \pi^0\pi^0) = 2 \times 10^{-6}$, where we could expect a significance of 2.04. The final row in the table gives the significance for the different optimisation cuts while in brackets is the expected significance if the selected optimisation cuts for $\mathcal{B}(B^0 \to \pi^0\pi^0)$ are applied. In all cases the expected significance for the optimal cuts and the selected optimisation cuts given by the $\mathcal{B}(B^0 \to \pi^0\pi^0) = 2 \times 10^{-6}$ optimisation are very close. We can therefore conclude that the choice of cuts is not highly dependent on the presumed $B^0 \to \pi^0\pi^0$ branching ratio and that our selected cuts given by the $\mathcal{B}(B^0 \to \pi^0\pi^0) = 2 \times 10^{-6}$ study are very close to optimal for all likely $B^0 \to \pi^0\pi^0$ branching fractions.
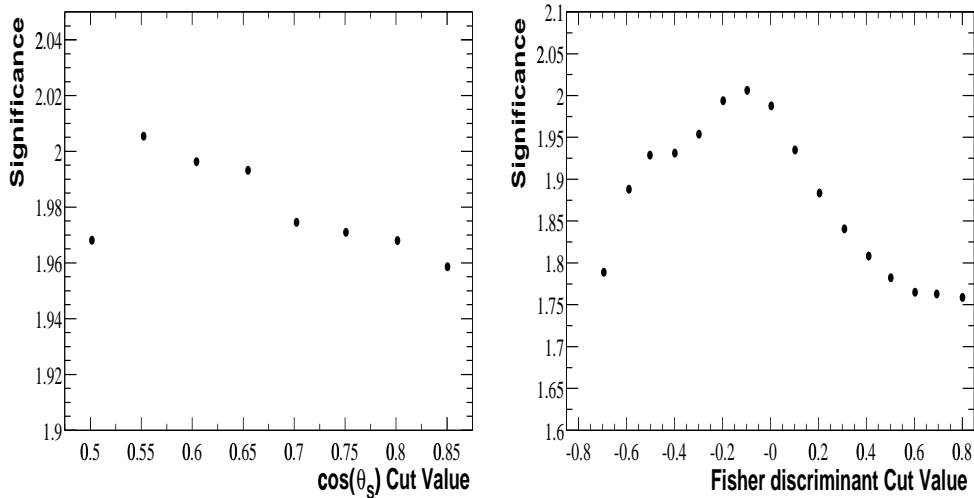
Figure 4.8: The expected significance for the cut and count analysis as a function of a cut on $|\cos(\theta_S)|$ (left) and the $\mathcal{F}$ discriminant (right). The optimisation presumes that $\mathcal{B}(B^0 \to \pi^0\pi^0) = 2 \times 10^{-6}$.

Figures 4.8, 4.9 and 4.10 show the individual significance distributions for each of the cut variables with the assumed $\mathcal{B}(B^0 \to \pi^0\pi^0) = 2 \times 10^{-6}$. For each of the
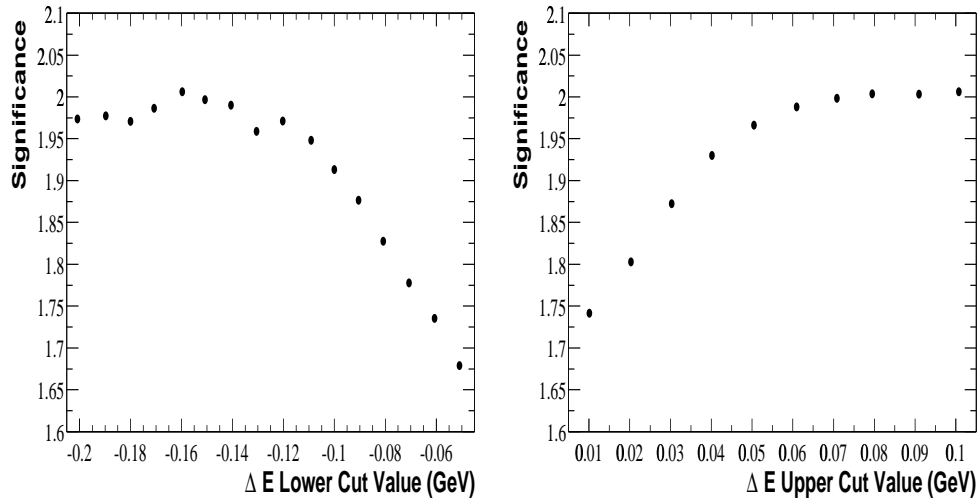
Figure 4.9: The expected significance for the cut and count analysis as a function of a cut on the low value of ΔE (left) and the high value of ΔE (right). The optimisation presumes that $\mathcal{B}(B^0 \rightarrow \pi^0 \pi^0) = 2 \times 10^{-6}$.
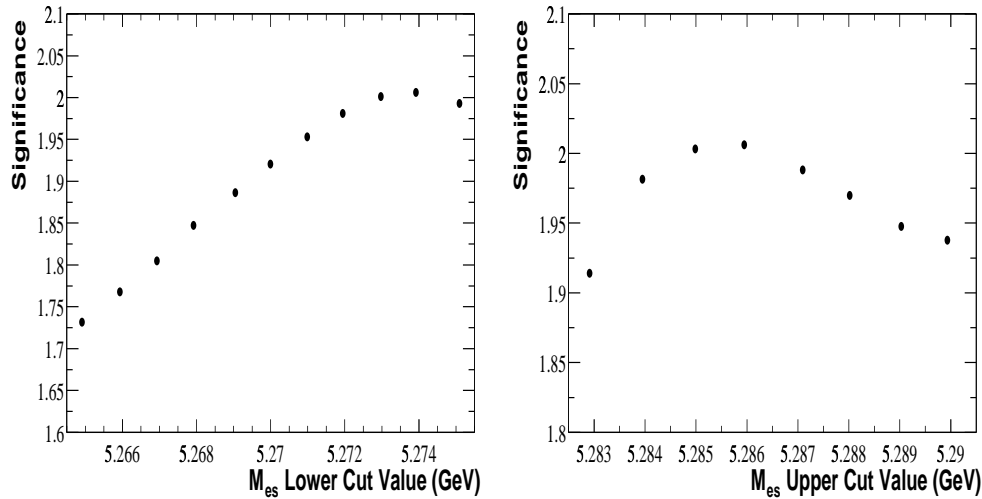
Figure 4.10: The expected significance for the cut and count analysis as a function of a cut on the low value of m_{ES} (left) and the high value of m_{ES} (right). The optimisation presumes that $\mathcal{B}(B^0 \rightarrow \pi^0 \pi^0) = 2 \times 10^{-6}$.

cut variables, all the other cut variables have been allowed to vary to maximise the significance and so are not necessarily set to their original optimal values to make the distributions. Figure 4.8 shows the effect of varying the cut on $|\cos(\theta_S)|$ and $\mathcal{F}$. Both have definite maximum points although the variation of maximum sensitivity with $|\cos(\theta_S)|$ cut value is minimal. Figure 4.9 shows the upper and lower cut values

for ΔE. In both cases the sensitivity distributions flatten out at some point, and any selection beyond that point will give largely similar results. Figure 4.10 shows the sensitivity distibutions for upper and lower cuts on m_{ES}. Both distributions come to definite peaks, but while the variation in sensitivity for the upper selection value is minimal, there is greater variation with the lower selected cuts.
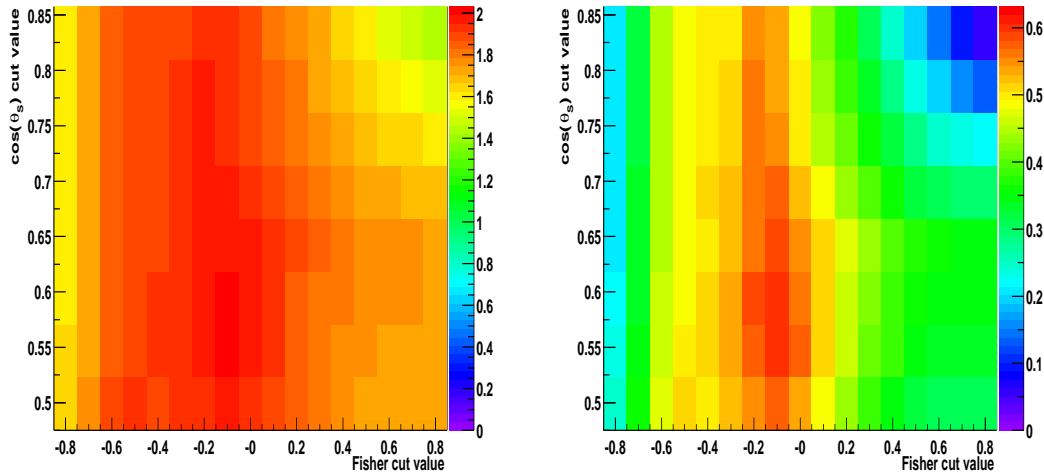
Figure 4.11: The $\mathcal{F}{:}|\cos(\theta_S)|$ cut plane showing the statistical significance for each cut. The left hand plot shows the raw data, while the right hand plot shows the same result but plots (significance - 1.4) rather than just the significance so to enhance the contrast. These optimisation results use the optimal selection for m_{ES} and ΔE and presume that $\mathcal{B}(B^0 \rightarrow \pi^0\pi^0) = 2 \times 10^{-6}$.

Figure 4.11 shows the variation in sensitivity across the cut plane of $|\cos(\theta_S)|$ and the $\mathcal{F}$ discriminant. The plots highlight that our selection at $|\cos(\theta_S)| < 0.55$ and $\mathcal{F} < -0.1$ is in the centre of a very stable sensitivity zone where changing the cuts up or down slightly makes no great difference to the overall result. The variation in sensitivity for all our cut variables is relatively slight. There is no great variation and we are certainly not searching for a small highly optimal region in six dimensional space. This is encouraging as it means we can make our selection cuts knowing that the significance should be relatively insensitive to the exact cuts.

4.5.3   Background scaling cross checks

The most vital part of the cut and count method is to accurately estimate the number of background events that are expected. While the method presented in the previous section appears robust it was decided to check how well the scaling of the GSB to signal regions worked on various elements of the on-resonance m_{ES}:ΔE plane.

The study uses 3 regions of the plane; an upper sideband defined by $0.2 < \Delta E < 0.4$ GeV, a central region where $-0.16 < \Delta E < 0.08$ GeV so matching the cut and count optimisation, and a lower sideband where $-0.4 < \Delta E < -0.2$ GeV. For each region a grand sideband region was defined in the same way as in the optimisation procedure with $5.20 < m_{ES} < 5.26$ GeV, and a signal region which was defined with $5.275 < m_{ES} < 5.285$ GeV. A cut was then applied ($\mathcal{F} > 0.5$) to remove potential B events in the on-resonance sample. Different cuts on $|\cos(\theta_S)|$ were also applied so as to check the validity of the background scaling method for tighter and tighter cuts on the background.

The same method as previously was then employed to predict how many events would be seen in the signal region. The same fit of the Argus function to the on-resonance m_{ES} distribution as with the cut and count was used to predict the ratio of GSB to signal region events. The number of GSB events were counted for each of the three regions and the ratio was used to predict the number of signal events. The actual number of signal events in each region was then counted.

The results of the scaling study are shown in table 4.6. In all cases we see good agreement between the number of events expected and those we actually see in the data once the relative statistical uncertainty has been taken into account. The data show that the scaling procedure applied to predict the number of continuum events in the cut and count analysis is accurate across the entire m_{ES}:ΔE plane, and consequently we can be confident in the accuracy of the cut and count analysis procedure.

Cuts applied	Region	GSB events	Scaling R	Expected events	Actual events
$\mathcal{F} > 0.5$, $\|\cos(\theta_S)\| < 0.8$	lower	930	0.106	98.6	87
$\mathcal{F} > 0.5$, $\|\cos(\theta_S)\| < 0.8$	central	770	0.106	81.6	88
$\mathcal{F} > 0.5$, $\|\cos(\theta_S)\| < 0.8$	upper	405	0.106	42.9	39
$\mathcal{F} > 0.5$, $\|\cos(\theta_S)\| < 0.75$	lower	400	0.106	42.4	45
$\mathcal{F} > 0.5$, $\|\cos(\theta_S)\| < 0.75$	central	319	0.106	33.8	37
$\mathcal{F} > 0.5$, $\|\cos(\theta_S)\| < 0.75$	upper	185	0.106	19.6	15
$\mathcal{F} > 0.5$, $\|\cos(\theta_S)\| < 0.6$	lower	50	0.106	5.3	5
$\mathcal{F} > 0.5$, $\|\cos(\theta_S)\| < 0.6$	central	38	0.106	4.0	1
$\mathcal{F} > 0.5$, $\|\cos(\theta_S)\| < 0.6$	upper	20	0.106	2.1	3

Table 4.6: .
The cut and count continuum background scaling cross check results. For 3 different sets of cuts, the number of events in the upper, lower and central signal regions is predicted using the same methodology as in the cut and count optimisation. The actual number of events seen is shown to compare against the predicted figures. The selection of $\mathcal{F} > 0.5$ effectively removes all B related events from the study.

4.6   Conclusions

In this chapter the initial criteria applied to efficiently select $B^0 \to \pi^0\pi^0$ events while reducing the dominant light quark backgrounds have been discussed. A cut-based analysis has been developed and the results of the optimisation procedure have been presented. The final results of the cut-based analysis on the full data sample are documented in Chapter 6, where the related systematic uncertainties are also discussed.

Chapter 5

Maximum Likelihood analysis of $B^0 \to \pi^0\pi^0$

5.1   Overview

In this chapter the maximum likelihood analysis for $B^0 \to \pi^0\pi^0$ is presented. The chapter begins by defining the components of the fit both in terms of the event types modelled and the PDF's (Probability Density Function) used to describe them. The analysis is then optimised to achieve the most significant result for $B^0 \to \pi^0\pi^0$ using a cut on $|\cos(\theta_S)|$ to reduce continuum background to the optimal level.

When searching for a rare decay such as $B^0 \to \pi^0\pi^0$ it is important to be sure that any signal you see is a real signal. We therefore extensively test the fit using various techniques; fits to different Monte Carlo and data samples, toy Monte Carlo studies of all the likely fit outcomes, and toy Monte Carlo studies where fully simulated $B^0 \to \pi^0\pi^0$ and $B^\pm \to \rho^\pm\pi^0$ events are used. The final results of the analysis are presented in chapter 6 along with the systematic errors and the cut-based analysis results.

5.2   Introduction

The analysis technique described in this section uses an unbinned multivariant extended maximum likelihood (ML) fit to extract the signal yield for $B^0 \to \pi^0\pi^0$ from the on-resonance data sample. A maximum likelihood technique is often preferable to a cut and count analysis as it uses more of the information within the data to give a result with greater statistical significance.

Three variables are used within the fit; m_{ES}, ΔE and the $\mathcal{F}$ discriminant. Three components are used within the fit to describe the different event types; $B^0 \to \pi^0\pi^0$, $B^{\pm} \to \rho^{\pm}\pi^0$ and continuum. PDF's are defined for each variable in each event type. The PDF's are defined using Monte Carlo events for the $B^0 \to \pi^0\pi^0$ and $B^{\pm} \to \rho^{\pm}\pi^0$ components, and the on-resonance data samples for the continuum component.

For each event the likelihood ($\mathcal{L}_i$) is defined as,

$$\mathcal{L}_i = \sum_{j=1}^{3} n_j \mathcal{P}_j(x_i) \tag{5.1}$$

where $\mathcal{P}_j(x_i)$ are the probabilities for each of the three event types evaluated with the observables x_i of the ith event. n_j are free parameters of the fit and correspond to the total number of events of each event type. The product of the PDF's for each type forms P_j.

For N input events, the overall likelihood is given by

$$\mathcal{L} = \frac{e^{-\sum n_i}}{N!} \prod_{i=1}^{N} \mathcal{L}_i \tag{5.2}$$

where the first term takes into account the Poisson fluctuations in the total number of events. Equation 5.2 represents the extended maxiumum likelihood function. The function is used to find the number of each signal and background component that maximises the likelihood $\mathcal{L}$.

5.3   PDF Definitions

5.3.1   Likelihood components, variables and correlations

The ML analysis methodology used in many other *BABAR* analyses uses the product
of PDF's describing individual variables. The validity of this concept is dependent
on the variables used being independent, or in other words uncorrelated. This is
not true for the $B^0 \to \pi^0\pi^0$ or $B^{\pm} \to \rho^{\pm}\pi^0$ final states. The correlation between
m_{ES}, ΔE, $\mathcal{F}$ and $\cos(\theta_S)$ have been studied for signal $B^0 \to \pi^0\pi^0$, $B^{\pm} \to \rho^{\pm}\pi^0$
and continuum Monte Carlo samples. Table 5.1 shows the results where only the
pre-selection (section 4.3) cuts were applied. There is a non-negligible correlation
between m_{ES} and ΔE for the $B^0 \to \pi^0\pi^0$ and $B^{\pm} \to \rho^{\pm}\pi^0$ samples. The correlation
is predominately in the low energy tails of the distributions that can be seen in
Figure 4.6.

Data type/ Correlation	m_{ES}:ΔE	ΔE:$\cos(\theta_S)$	ΔE:$\mathcal{F}$	m_{ES}:$\cos(\theta_S)$	m_{ES}:$\mathcal{F}$	$\mathcal{F}$:$\cos(\theta_S)$
$B^0 \to \pi^0\pi^0$	0.244	0.009	0.012	-0.025	-0.029	0.743
$B^{\pm} \to \rho^{\pm}\pi^0$	0.215	0.006	0.011	-0.026	-0.029	0.748
Continuum	0.013	-0.034	-0.046	-0.002	-0.004	0.692

Table 5.1: The correlations between variables for the components of the ML fit

The correlation between the $\mathcal{F}$ and $\cos(\theta_S)$ for all the fit components is expected
as they are both event-shape variables. This is taken into account by applying an
optimised cut in $\cos(\theta_S)$ while using $\mathcal{F}$ in the ML fit. This procedure is described
in section 5.4. The correlations between ΔE and m_{ES} mean that using a product of
1-D uncorrelated PDF's will never accurately take into account all the information
presented in the ΔE - m_{ES} plane for the $B^0 \to \pi^0\pi^0$ or $B^{\pm} \to \rho^{\pm}\pi^0$ components.
A numerical two dimensional *Keys* PDF [44] has therefore been used to model the
m_{ES}:ΔE plane for the $B^0 \to \pi^0\pi^0$ and $B^{\pm} \to \rho^{\pm}\pi^0$ components. The idea and
implementation of the Keys PDF is discussed further in section 5.3.2. As there is no
significant correlation between the m_{ES} and ΔE variables for the continuum sample,
individual PDF's are used to model these variables.

The ML fit used is based on fitting to the variables m_{ES}, ΔE and $\mathcal{F}$ for the signal $B^0 \to \pi^0\pi^0$, $B^\pm \to \rho^\pm\pi^0$ and continuum backgrounds. The fit region is $-0.4 < \Delta E < 0.4\,\text{GeV}$ and $5.20 < m_{ES} < 5.29\,\text{GeV}$ unless otherwise stated. The full range of the $\mathcal{F}$ discriminant is used within the fit. In addition the optimised cut in $|\cos(\theta_S)|$ is the only other cut used as well as the pre-selection cuts described in section 4.3.

The m_{ES} - ΔE plane for on-resonance events passing a cut at $|\cos(\theta_S)| < 0.7$ can be seen in Figure 5.1. Events in the signal region have been omitted but the plot shows the grand ($-0.4 < \Delta E < 0.4\,\text{GeV}$, $5.20 < m_{ES} < 5.25\,\text{GeV}$), upper ($0.2 < \Delta E < 0.4\,\text{GeV}$, $5.20 < m_{ES} < 5.29\,\text{GeV}$) and lower ($-0.4 < \Delta E < -0.2\,\text{GeV}$, $5.20 < m_{ES} < 5.29\,\text{GeV}$) sidebands used for various continuum PDF definitions and fit cross-checks. The events in the signal region are omitted as the ML analysis, like the cut-based, follows a blind-analysis principle. This dictates that all elements of the analysis are decided upon without viewing the signal region of the data so to avoid potential bias. The principle is further discussed in [45].

This section describes and documents the PDF's adopted for the ML fit section of the analysis and is followed by several plots showing the results of fitting them to Monte Carlo and data samples. Table 5.2 shows the functions used to parameterize the various components of the fit.

Variable/Data type	$B^0 \to \pi^0\pi^0$	$B^\pm \to \rho^\pm\pi^0$	Continuum
m_{ES}	2-D Keys	2-D Keys	Argus
ΔE	2-D Keys	2-D Keys	Polynomial
$\mathcal{F}$	Double Gaussian	Double Gaussian	Double Gaussian

Table 5.2: Functions used to determine PDF's for the ML fit components
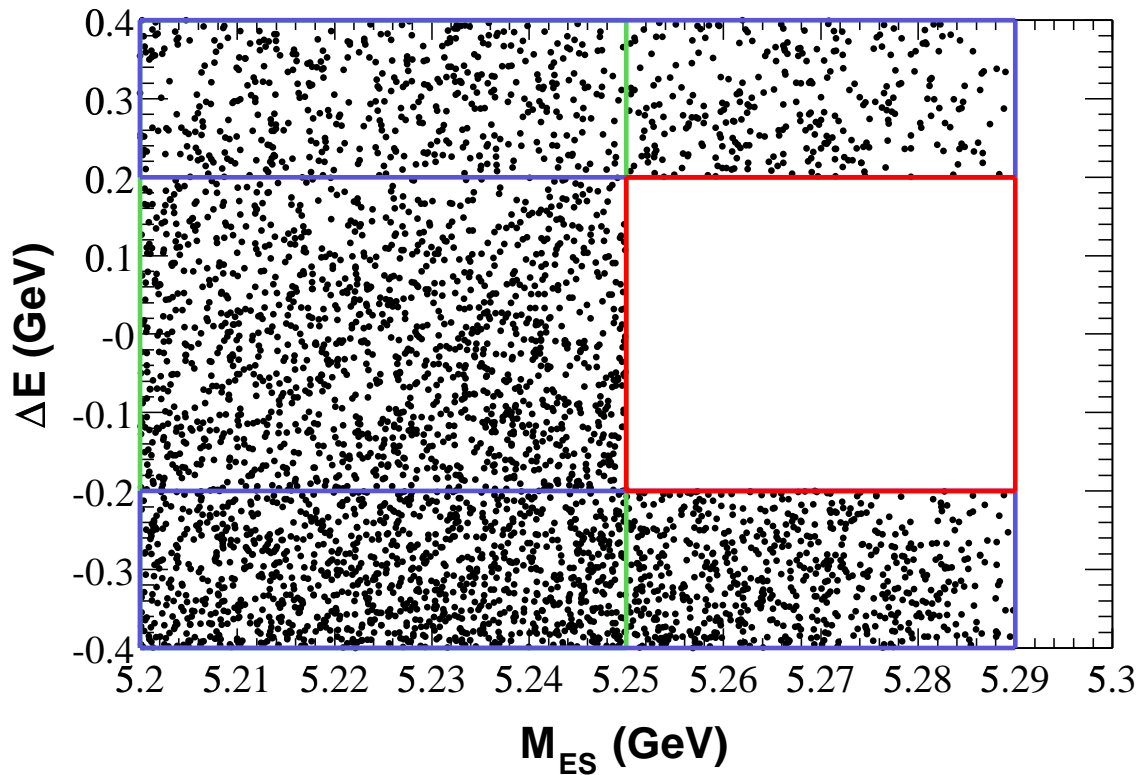
Figure 5.1: Events passing selection cuts for the ML analysis with the signal region blinded (for display purposes).

5.3.2   Functional Forms of the PDF's

The Gaussian distribution

The Gaussian distribution is given by

$$G(x : \mu : \sigma) = \frac{1}{\sigma\sqrt{2\pi}} \cdot e^{-(x-\mu)^2/(2\sigma^2)} \tag{5.3}$$

where μ is the mean of the distribution and σ is the width. The Double Gaussian distribution is given by

$$DG(x : \mu_1 : \sigma_1, \mu_2 : \sigma_2 : f) = fG(x : \mu_1 : \sigma_1) + (1 - f)G(x : \mu_2 : \sigma_2) \tag{5.4}$$

where G is a single Gaussian and f represents the fraction of each Gaussian included in the double Gaussian distribution.

The Argus background distribution

The Argus [42] distribution is used to parameterise the m_{ES} continuum background shape and is given by

$$A(x : x_0, c) = \frac{1}{N} x \sqrt{1 - (x/x_0)^2} e^{(\xi(1-(x/x_0)^2))} \qquad (5.5)$$

where x_0 represents the kinematic upper limit of m_{ES} (5.29 GeV for $e^+e^- \to \Upsilon(4S)$), N is a normalisation factor and ξ is the fitted parameter representing the line shape. The distribution was developed to parameterise distributions with kinematic limits.

Polynomial distribution

The polynomial distribution, of order n is given by

$$P(x : c_1, \ldots, c_n) = \frac{1}{N} \left(1 + \sum_{k=1}^{n} c_k x^k \right) \qquad (5.6)$$

where c_i are fitted parameters and N is a normalisation factor. A polynomial of order 2 is used to describe the continuum ΔE distribution.

Two dimensional Keys PDF

The 2-dimensional Keys PDF is based on the one dimensional model described in detail elsewhere [44]. The Keys PDF uses "kernal estimation" to effectively model any distribution. The idea is that any distribution can be modelled by placing a Gaussian kernal of probability at each event in the sample. By summing the contributions across the event sample a smoothed representation of the data can be achieved. For a 2-dimensional model, a 2-dimensional Gaussian kernal is applied at each data point and the contributions are summed across the 2-dimensional plane.

One problem when generating the Keys PDF is that if the fit domain matches the data domain, one tends to underestimate the PDF close to the boundary as there are no probability contributions from beyond the boundary. To overcome this it is

necessary to include data beyond the fit boundary to generate the PDF while only normalising over the fit domain. The quality of any 2-D Keys PDF relies heavily on the number of data points used to generate the model.

5.3.3   PDF's for $B^0 \to \pi^0\pi^0$ and $B^\pm \to \rho^\pm\pi^0$ components

The $B^0 \to \pi^0\pi^0$ and $B^\pm \to \rho^\pm\pi^0$ components of the fit use the 2-D Keys PDF to simultaneously model the m_{ES} and ΔE variables. The main reason for using the Keys is the belief that it will accurately model the correlations seen between these variables which were highlighted in section 5.3.1. The $\mathcal{F}$ distribution is modelled with a double Gaussian.

Figures 5.2 and 5.3 shows the projections of the generated Keys PDF for the m_{ES} and ΔE variables for $B^0 \to \pi^0\pi^0$ events. The 2-D Keys appears to model both distributions accurately. We can see that the m_{ES} distribution is peaked at the B mass, while ΔE has a central value slightly shifted from zero. Both distributions have tails, but the most significant is in ΔE where energy loss in the EMC gives a significant contribution to the $B^0 \to \pi^0\pi^0$ PDF all the way out to $-0.4\,\mathrm{GeV}$. While the Keys PDF appears to model the data well for the one dimensional projections, the PDF is best viewed in 2-dimensions.

Figure 5.4 shows a 2-dimensional lego plot of the m_{ES}:ΔE plane for both the $B^0 \to \pi^0\pi^0$ Monte Carlo events, and the Keys PDF generated from these data. While the Keys PDF is smoother in nature, it seems to accurately model the Monte Carlo distribution across the plane.

A better test is provided by $B^\pm \to \rho^\pm\pi^0$ as the m_{ES}:ΔE correlation is stronger. Figures 5.5 and 5.6 show the projections in m_{ES} and ΔE for the $B^\pm \to \rho^\pm\pi^0$ Monte Carlo events with the 2-D Keys PDF overlayed. Again the Keys PDF accurately models the two distributions. As the $B^\pm \to \rho^\pm\pi^0$ events are reconstructed as $B^0 \to \pi^0\pi^0$ with one low momentum $\pi^\pm$ missing, the resolution in m_{ES} is far worse than for $B^0 \to \pi^0\pi^0$ and the tail in the distribution is far more significant. In ΔE we
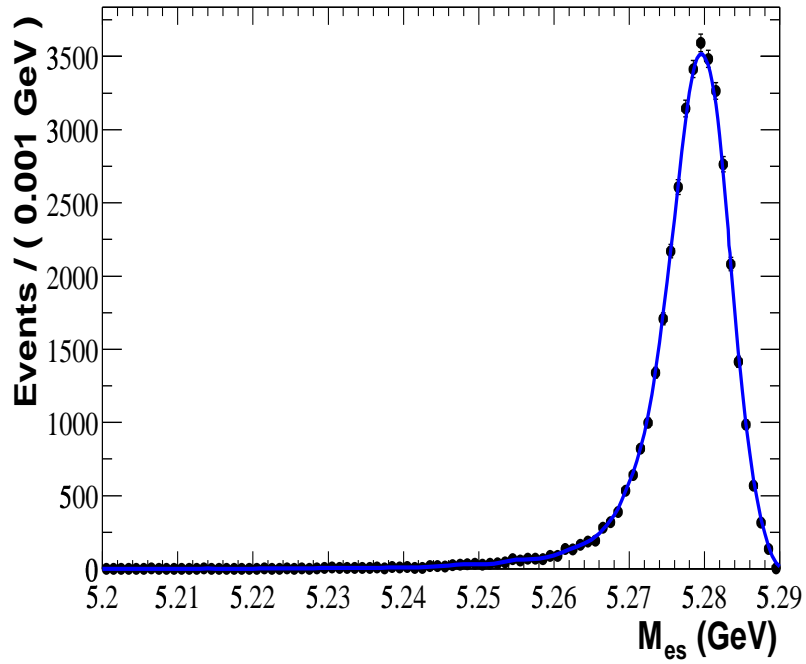
Figure 5.2: The Monte Carlo m_{ES} distribution for $B^0 \rightarrow \pi^0\pi^0$. The projected of the PDF generated by the 2-D Keys function is overlayed.
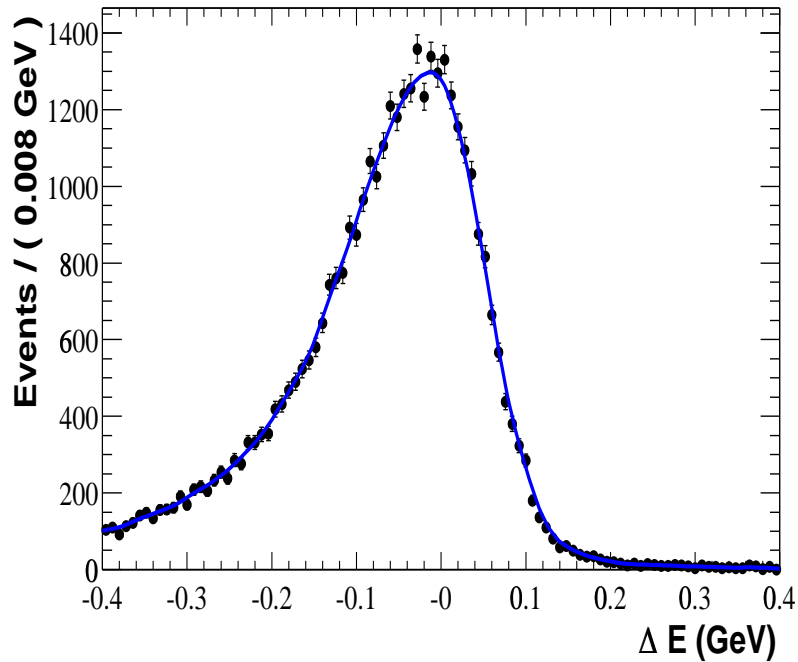
Figure 5.3: The Monte Carlo ΔE distribution for $B^0 \rightarrow \pi^0\pi^0$. The projection of the PDF generated by the 2-D Keys function is overlayed.
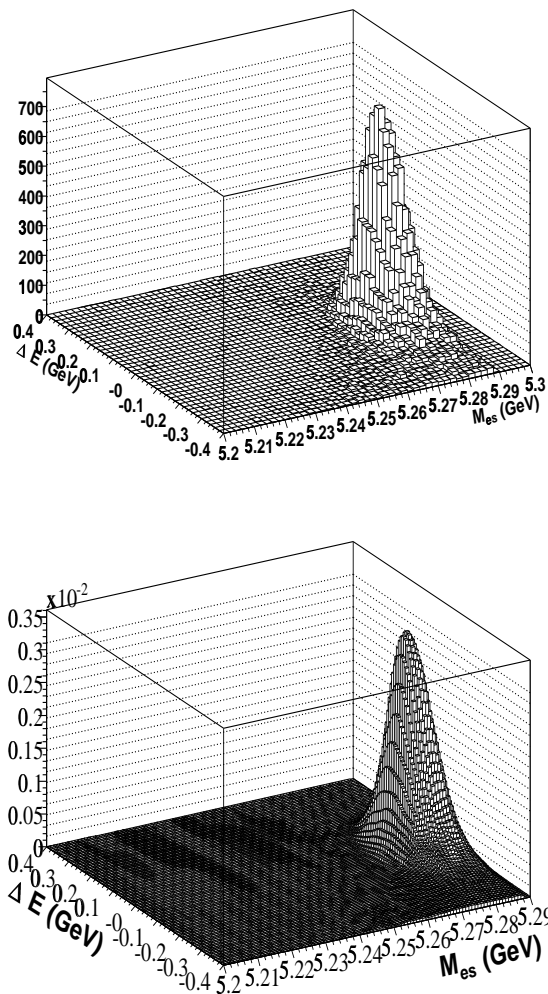
Figure 5.4: The $m_{ES} : \Delta E$ distribution for $B^0 \to \pi^0 \pi^0$ Monte Carlo is shown on the top lego plot, while the Keys PDF generated from these data is shown on the bottom.

can see that the distribution is centred around $-0.35\,\mathrm{GeV}$ giving relatively good separation with $B^0 \to \pi^0 \pi^0$ events.

Because of the missing track in the reconstruction, the $B^\pm \to \rho^\pm \pi^0$ events are spread across the $m_{ES} : \Delta E$ plane. Figure 5.7 shows the $m_{ES} : \Delta E$ plane for $B^\pm \to \rho^\pm \pi^0$ Monte Carlo events and for the 2-D Keys PDF generated from these data. As with $B^0 \to \pi^0 \pi^0$ the PDF appears to accurately model the distribution seen in the Monte Carlo events across all areas of the plane. For both $B^0 \to \pi^0 \pi^0$ and $B^\pm \to \rho^\pm \pi^0$
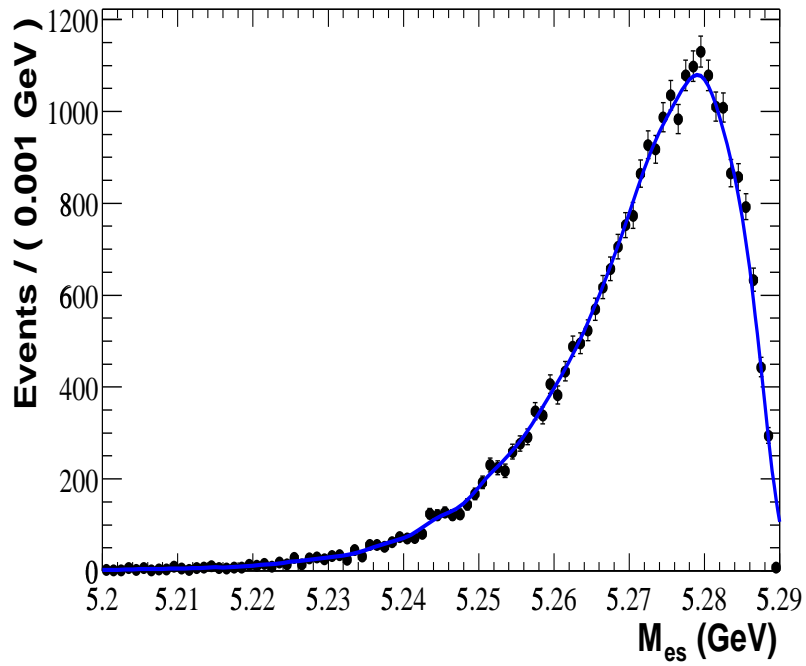
Figure 5.5: The Monte Carlo m_{ES} distribution for $B^{\pm} \rightarrow \rho^{\pm}\pi^0$. The projection of the PDF generated by the 2-D Keys function is overlayed
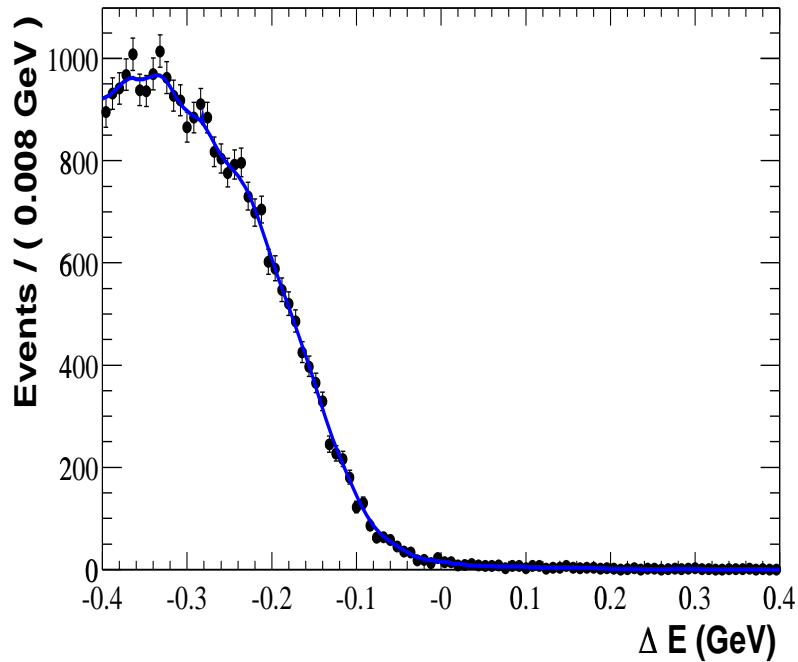
Figure 5.6: The Monte Carlo ΔE distribution for $B^{\pm} \rightarrow \rho^{\pm}\pi^0$. The projection of the PDF generated by the 2-D Keys function is overlayed.
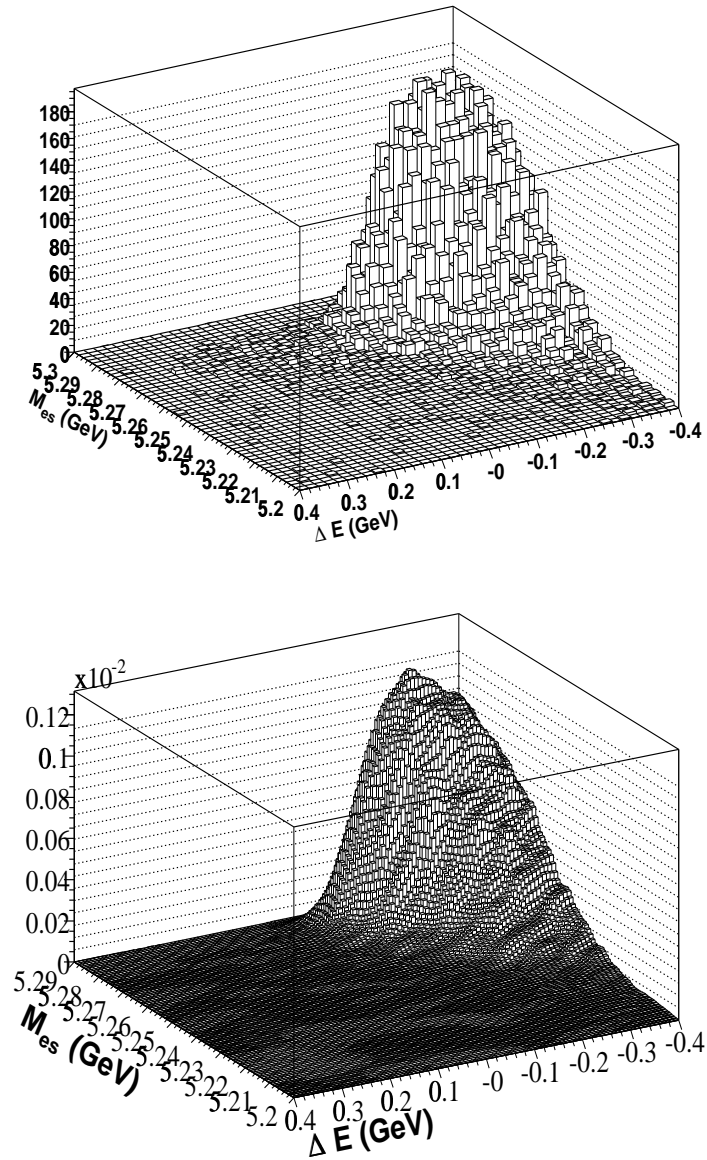
Figure 5.7: The $m_{ES} : \Delta E$ distribution for $B^{\pm} \to \rho^{\pm}\pi^0$ Monte Carlo events is shown in the top lego plot, while the Keys PDF generated from these data is shown at the bottom. Note that the $m_{ES} : \Delta E$ plane is rotated when compared to figure 5.4 so to show Monte Carlo - PDF comparison to best effect.

it appears that the 2-D Keys PDF provides a good model of the distributions and takes account of the correlations seen between m_{ES} and ΔE.

Figure 5.8 shows the $B^0 \to \pi^0\pi^0$ and $B^{\pm} \to \rho^{\pm}\pi^0$ $\mathcal{F}$ distributions with the respective
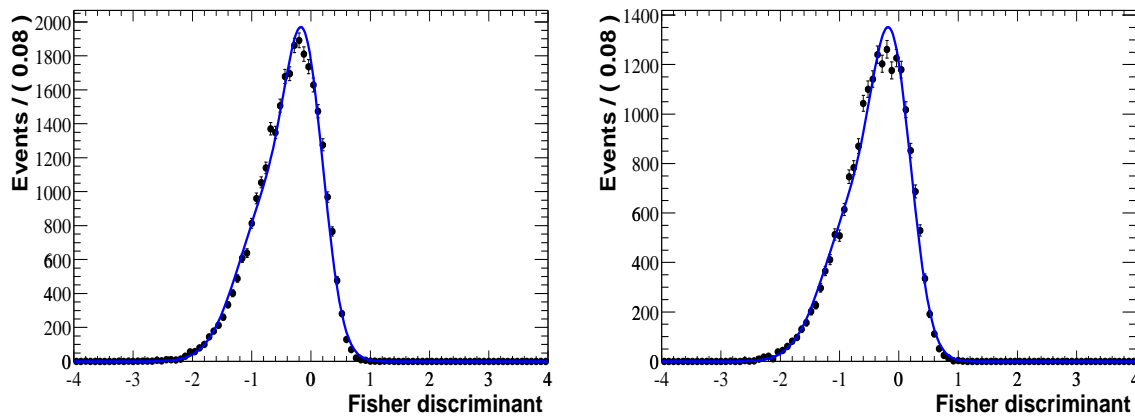
Figure 5.8: The Monte Carlo $B^0 \to \pi^0\pi^0$ (left) and $B^\pm \to \rho^\pm\pi^0$ (right) $\mathcal{F}$ distributions with the double Gaussian PDFs overlayed.

double Gaussian PDF's overlayed. The $\mathcal{F}$ discriminant is based on the tracks and clusters making up the rest of the event, so does not include the two π^0's used in the B reconstruction. For $B^0 \to \pi^0\pi^0$ and $B^\pm \to \rho^\pm\pi^0$ the rest of the event should simply be the tracks and clusters associated with the other B, so that the $\mathcal{F}$ distribution for $B^0 \to \pi^0\pi^0$ and $B^\pm \to \rho^\pm\pi^0$ should be almost identical. As $B^\pm \to \rho^\pm\pi^0$ includes a soft track that is missing in the B reconstruction, this must be included in the calculation of the $\mathcal{F}$ discriminant so we expect to see a small difference between the $\mathcal{F}$ PDF for $B^0 \to \pi^0\pi^0$ and $B^\pm \to \rho^\pm\pi^0$. We therefore use two separate parameterisations for $B^0 \to \pi^0\pi^0$ and $B^\pm \to \rho^\pm\pi^0$.

5.3.4   Continuum PDFs

Figure 5.9 shows the m_{ES} distribution for on-resonance events with a cut at $\mathcal{F} > 0.5$ applied to remove potential B related signal events. A fit to the Argus function is overlayed. Figure 5.10 shows the ΔE distributions for the on-resonance data with $m_{ES} < 5.25 \, \text{GeV}$ so removing potential B related events. A second order polynomial is used to fit the distribution and is overlayed on the data. Figure 5.11 shows the $\mathcal{F}$ distribution for the same on-resonance data sample as that used for the ΔE figure. A double Gaussian fit to the data is overlayed.

The on-resonance data are used to determine the PDF's for each of the m_{ES}, ΔE and $\mathcal{F}$ distributions rather than a potentially larger sample of continuum Monte
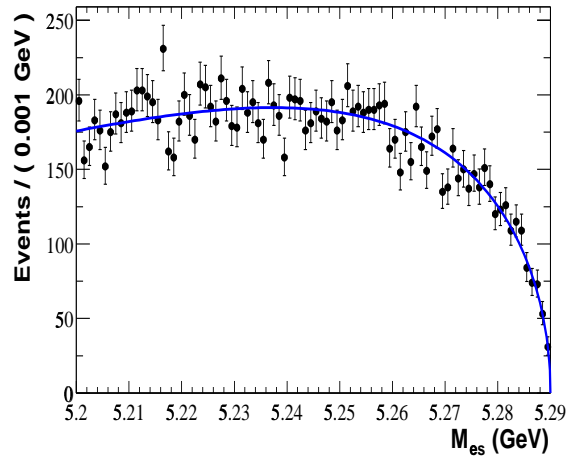
Figure 5.9: The on-resonance m_{ES} distribution showing the Argus PDF fit overlayed.
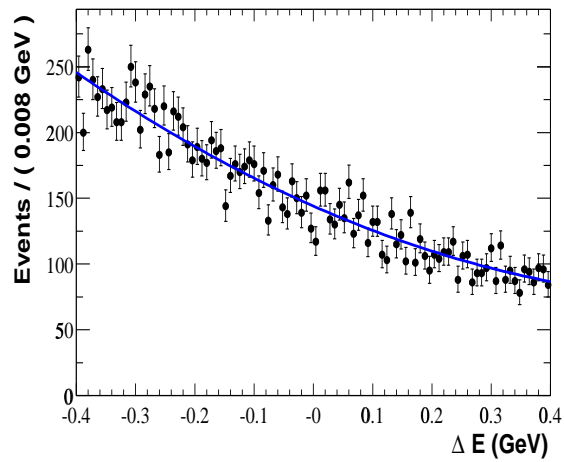
Figure 5.10: The on-resonance ΔE distribution showing the second order polynomial PDF over-layed.
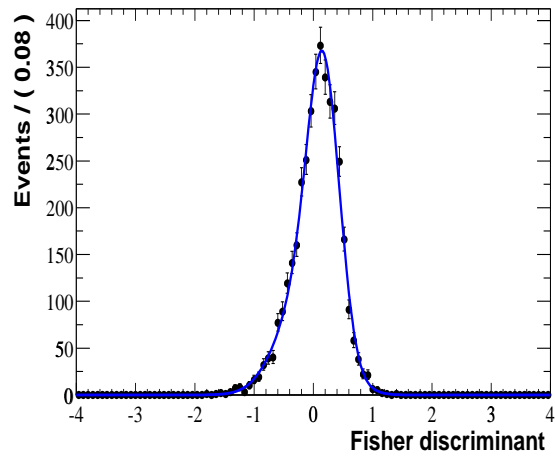
Figure 5.11: The on-resonance $\mathcal{F}$ distribution with the double Gaussian PDF fit overlayed.

Carlo events as there are then no systematic errors for PDF shape assumptions associated with modelling the on-resonance sample. In defining the data samples to fit these PDF's, a cut has to be applied to remove potential B related signal events. This limits the statistics of the available sample so increasing the size of the statistical error on the fitted PDF parameters. One possible way to reduce these is to use the final sample, where we have the maximum on-resonance statistics to define the PDF parameters, so floating the parameters in the final fit. This option is further investigated in the following sections.

5.3.5   Continuum PDF crosschecks with different data samples

One of the problems seen in earlier versions of this analysis [46] came from an apparent correlation between the fitted ξ parameter of the Argus function and the value of ΔE in the on-resonance sample. Previous versions of the analysis used an alternative to m_{ES} known as m_{EC} which used an additional B energy constraint to kinematically fit the constrained mass. m_{EC} is further discussed in [40] where a study shows that it gives a better resolution for B signal events than m_{ES}, so making it the variable of choice. However, when using this variable, a trend became apparent when trying to parameterise m_{EC} for continuum events where the value of ξ became progressively more negative at higher values of ΔE.

Table 5.3 shows the fitted value of ξ for both m_{ES} and m_{EC} for on-resonance and continuum Monte Carlo events across different ΔE strips. We can see that for the on-resonance sample the values of ξ across the different ΔE strips are in good agreement when considering m_{ES}. For m_{EC} we see far greater variation with ξ becoming more negative at higher values of ΔE and the individual values being barely statistically consistent. The same trends can be seen in the continuum Monte Carlo but the effect is even more pronounced.

The consistency of ξ for m_{ES} and the variation in m_{EC} is shown in figures 5.12 and 5.13. The figures clearly show a variation in the m_{EC} shape across the plane,
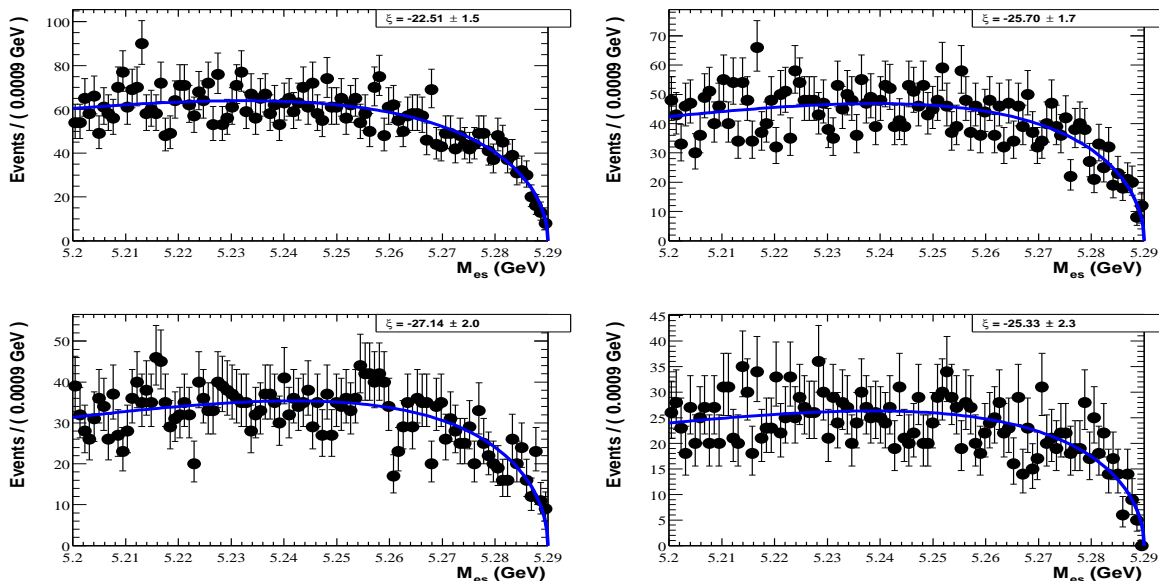
Figure 5.12: On-resonance m_{ES} distributions showing the variation in the fitted ξ Argus parameter. The top left plot corresponds to the ΔE range $(-0.4 < \Delta E < -0.2\,\text{GeV})$, top right to $(-0.2 < \Delta E < 0.0\,\text{GeV})$, bottom left to $(0.0 < \Delta E < 0.2\,\text{GeV})$ and bottom right to $(0.2 < \Delta E < 0.4\,\text{GeV})$. A cut on $\mathcal{F}$ was applied to remove over 90% of the $B^0 \to \pi^0\pi^0$ and $B^\pm \to \rho^\pm\pi^0$ events in the sample.
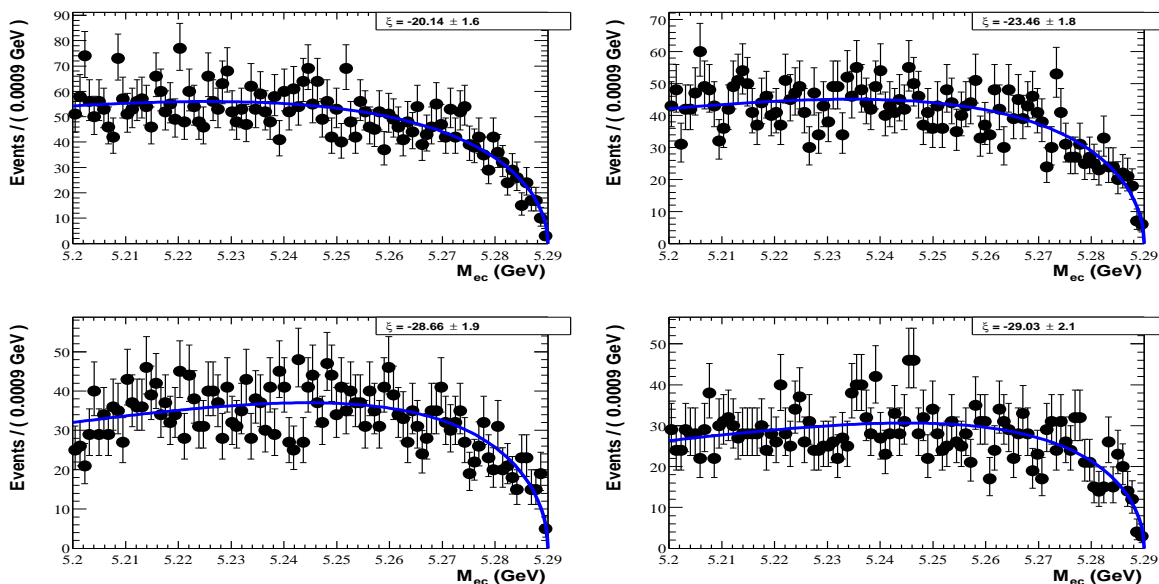
Figure 5.13: On-resonance m_{EC} distributions showing the variation in the fitted ξ Argus parameter. The top left plot corresponds to the ΔE range $(-0.4 < \Delta E < -0.2\,\text{GeV})$, top right to $(-0.2 < \Delta E < 0.0\,\text{GeV})$, bottom left to $(0.0 < \Delta E < 0.2\,\text{GeV})$ and bottom right to $(0.2 < \Delta E < 0.4\,\text{GeV})$. A cut on $\mathcal{F}$ was applied to remove over 90% of the $B^0 \to \pi^0\pi^0$ and $B^\pm \to \rho^\pm\pi^0$ events in the sample.

| Fit Region | On-resonance | | Continuum MC | |
in $\Delta E(\text{GeV})$	$m_{ES}\ \xi$	$m_{EC}\ \xi$	$m_{ES}\ \xi$	$m_{EC}\ \xi$
-0.45 - 0.45	-25.2 ± 0.8	-24.2 ± 0.9	-25.6 ± 0.8	-26.1 ± 0.9
-0.45 - -0.30	-24.2 ± 1.6	-18.7 ± 1.8	-24.7 ± 1.6	-21.0 ± 1.8
-0.30 - -0.15	-23.1 ± 1.8	-19.9 ± 1.9	-21.1 ± 1.8	-19.0 ± 1.9
-0.15 - 0.00	-27.4 ± 2.0	-26.0 ± 2.1	-26.9 ± 2.0	-27.1 ± 2.0
0.00 - 0.15	-26.1 ± 2.2	-27.5 ± 2.2	-29.9 ± 2.2	-29.9 ± 2.2
0.15 - 0.30	-28.8 ± 2.5	-31.0 ± 2.4	-27.0 ± 2.5	-31.5 ± 2.4
0.30 - 0.45	-23.1 ± 2.9	-28.6 ± 2.6	-27.4 ± 2.8	-36.2 ± 2.6
-0.40 - 0.40	-24.8 ± 0.9	-24.5 ± 0.9	-25.6 ± 0.9	-26.3 ± 0.9
-0.40 - -0.20	-22.5 ± 1.5	-20.1 ± 1.6	-23.2 ± 1.5	-20.8 ± 1.6
-0.20 - 0.00	-25.7 ± 1.7	-23.5 ± 1.8	-25.3 ± 1.7	-25.2 ± 1.7
0.00 - 0.20	-27.1 ± 2.0	-28.6 ± 1.9	-29.9 ± 2.0	-30.8 ± 1.9
0.20 - 0.40	-25.3 ± 2.3	-29.0 ± 2.1	-26.2 ± 2.3	-32.1 ± 2.1

Table 5.3: The results of Argus function fits to the on-resonance and continuum m_{ES} and m_{EC} distributions for different slices of ΔE. The fits were performed with a cut imposed on the $\mathcal{F}$ discriminant to remove over 90% of possible B signal contamination.

while m_{ES} is far more consistent. If we were using m_{EC} we would be forced to either develop a 2-dimensional fit similar to the 2-D Keys PDF for the $B^0 \to \pi^0\pi^0$ and $B^{\pm} \to \rho^{\pm}\pi^0$ components, or to apply a large systematic error to ξ so to take account of the possible variation. Fortunately the effect is not seen in m_{ES}, so a 2-dimensional fit or large systematic is not necessary. The reason that m_{EC} sees this subtle correlation with ΔE seems to be the due to fact that the B mass constraint is not appropriate for non-B events so it produces a bias on the continuum events.

Table 5.4 shows an additional crosscheck of the stability of ξ with different cuts applied to the $\mathcal{F}$ discriminant and to $|\cos(\theta_S)|$. Again for all the cuts applied the value of ξ is stable, both for the on-resonance and continuum Monte Carlo samples. The studies in this section give us confidence that the continuum events can be represented by separate PDF's for m_{ES}, ΔE and $\mathcal{F}$ which are not correlated.

Cut on $\|\cos(\theta_{SPH})\|$	Cut on $\mathcal{F}$	On-resonance m_{ES} ξ	Continuum MC m_{ES} ξ
< 0.9	None	−24.1± 0.7	−28.4± 1
< 0.9	> −0.5	−26.4± 1	−28.6± 1
< 0.9	> 0.0	−26.2± 1	−28.1± 1
< 0.9	> 0.5	−26.2± 2	−27.1± 2
< 0.9	> 1.0	−27.1± 3	−25.9± 3
< 0.8	None	−26.2± 2	−29.2± 2
< 0.75	None	−25.6± 2	−29.0± 2
< 0.7	None	−26.7± 3	−30.1± 3
< 0.6	None	−29.7± 3	−27.5± 3
< 0.5	None	−31.7± 4	−24.5± 4

Table 5.4: The results of Argus function fits to the on-resonance and continuum m_{ES} distribution with different selection criteria imposed for the $\mathcal{F}$ and $|\cos(\theta_S)|$ variables. The fits were performed using data across the ΔE plane ($-0.4 < \Delta E < 0.4$). Over 90% of the B related signal components were removed by the various selections.

5.4   Optimisation Procedure for the Maximum Likelihood Fit

5.4.1   Methodology

The maximum likelihood analysis optimisation uses a cut on $|\cos(\theta_S)|$ and is performed in the following way.

1. The branching fraction for $B^0 \to \pi^0\pi^0$ is assumed to be $2{\times}10^{-6}$ and for $B^{\pm} \to \rho^{\pm}\pi^0$ to be $2{\times}10^{-5}$. These are effectively the CLEO [43] central values although only upper limits were published.

2. Given a cut value for $|\cos(\theta_S)|$ the presumed mean number of $B^0 \to \pi^0\pi^0$ and $B^{\pm} \to \rho^{\pm}\pi^0$ are determined by the following equations:

$$N_{comp} \;=\; \epsilon_{comp} \cdot \mathcal{B}(comp) \cdot \mathcal{N}_{B\bar{B}}; \tag{5.7}$$

where ϵ_{comp} is the efficiency of either component, $\mathcal{B}(comp)$ is the assumed branching fraction and $\mathcal{N}_{B\bar{B}}$ is the number of $B\bar{B}$ events in the Run 1 data sample.

3. The mean number of continuum events is assumed to be the same as the number of events passing the $|\cos(\theta_S)|$ cut within our data sample as the number of $B^0 \to \pi^0 \pi^0$ and $B^\pm \to \rho^\pm \pi^0$ events is very small compared to the overall number of events.

4. For each cut on $|\cos(\theta_S)|$ a likelihood $\mathcal{L}$ is built from the three variables m_{ES}, ΔE and $\mathcal{F}$ as described in section 5.3. While the m_{ES}:ΔE PDF's are unaffected by a change in the $|\cos(\theta_S)|$ cut, it is necessary to re-parameterize the $\mathcal{F}$ PDF due to the correlations shown in table 5.1.

5. 1000 toy Monte Carlo experiments are made for each $|\cos(\theta_S)|$ value. The cut on $|\cos(\theta_S)|$ is varied between (0.5 - 0.9) in steps of 0.05. The m_{ES}, ΔE and $\mathcal{F}$ distributions are generated according to the appropriate PDF's while the numbers of signal and background events are fluctuated according to Poisson's law about a mean determined by the methods described in points 2) and 3).

6. The distribution of statistical significance for each cut value is formed from performing the nominal fit on each of the 1000 experiments. The statistical significance is given by:

$$\text{Significance} \quad = \quad \sqrt{-2\text{Log}(L_{null}/L_{max})} \tag{5.8}$$

where L_{max} is the maximum likelihood from the fit, while L_{null} is the likelihood for the null fit hypothesis, where the fit is performed with the number of $B^0 \to \pi^0 \pi^0$ set to zero. The mean of the significance is the value used to decide which cut provides the optimum configuration and is calculated by fitting a Gaussian to the significance distribution from the 1000 toy Monte Carlo experiments.

7. The free parameters in the fit are the number of $B^0 \to \pi^0 \pi^0$, $B^\pm \to \rho^\pm \pi^0$ and continuum which are not constrained to return positive values. Additionally the parameters for the continuum PDF's (m_{ES} Argus function, ΔE polynomial and double Gaussian $\mathcal{F}$) are also floated in the fit. The continuum components are floated as this removes the systematic errors associated with

these components in the final fit to the on-resonance sample, and the full on-resonance data represents the largest sample that can be used to define these PDF's, so minimising the statistical error related to these PDF's also. The continuum PDF's used for generation of the continuum events are given by those shown and described in section 5.3.4.

As well as observing the mean significance, it is useful to also monitor the quality of the fit. It is no use selecting the cut value with the highest mean significance if the fit is in some way biased in favour of the $B^0 \rightarrow \pi^0\pi^0$ component. To do this we define the pull for each fit component as.

$$Pull = \frac{\mathcal{N}_{fitted} - \mathcal{N}_{input}}{\sigma_{fitted}} \tag{5.9}$$

where $\mathcal{N}_{fitted}$ is the number fitted for each component, $\mathcal{N}_{input}$ is the mean number expected and σ_{fitted} is the error on the fitted component. As we are dealing with low numbers of generated and fitted $B^0 \rightarrow \pi^0\pi^0$ and $B^\pm \rightarrow \rho^\pm\pi^0$ components it is necessary to use the asymmetric Migrad errors from the fit. In practice this means that if the value $\mathcal{N}_{fitted} - \mathcal{N}_{input}$, or the residual of this fit component, is positive we use the absolute value of the lower, or negative, asymmetric error to define the pull. If the residual is negative we use the positive asymmetric error. Figure 5.14 shows typical pull and significance distributions for the toy Monte Carlo studies with the respective Gaussian fits overlayed.

As we also have two B components in $B^0 \rightarrow \pi^0\pi^0$ and $B^\pm \rightarrow \rho^\pm\pi^0$ which have similar PDF's, it is also necessary to examine the correlation between these components in the toy MC studies. The correlation is extracted by plotting the residuals (as defined above) for each of the two components on a 2-D histogram and extracting the correlation factor between the two variables. Figure 5.15 shows the correlations for all the components. We check the correlations derived in this way by taking the correlation directly from the fit correlation matrix. Figure 5.16 shows an example of the correlation between $B^0 \rightarrow \pi^0\pi^0$ and $B^\pm \rightarrow \rho^\pm\pi^0$ derived in this way, with a
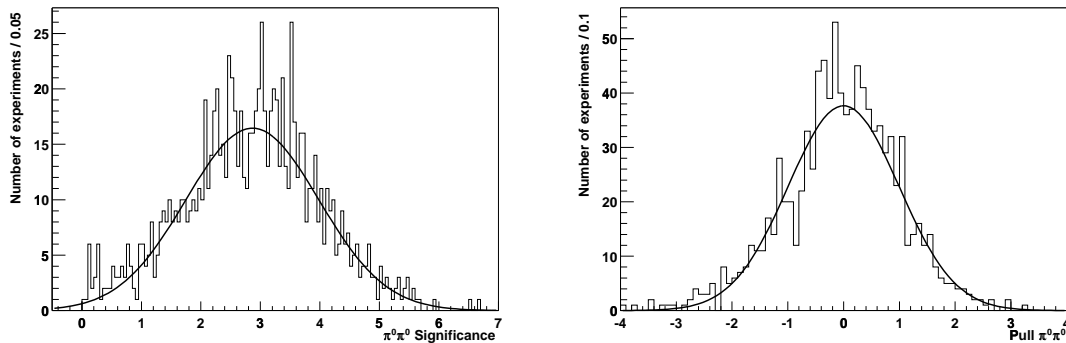
Figure 5.14: Examples of the significance distribution (left) and the $B^0 \to \pi^0\pi^0$ pull distribution (right) from the optimisation procedure. Both distributions are fitted with a Gaussian to extract their mean values. These results are taken from the study where a cut at $|\cos(\theta_S)| < 0.7$ is applied.

Gaussian fit overlayed. The two methods for deriving the correlations give results which are very compatible.

The examination of the pulls and correlations for the $B^0 \to \pi^0\pi^0$ component is undertaken in all the studies we perform as the accuracy of the final fit result is the primary concern of the analysis.
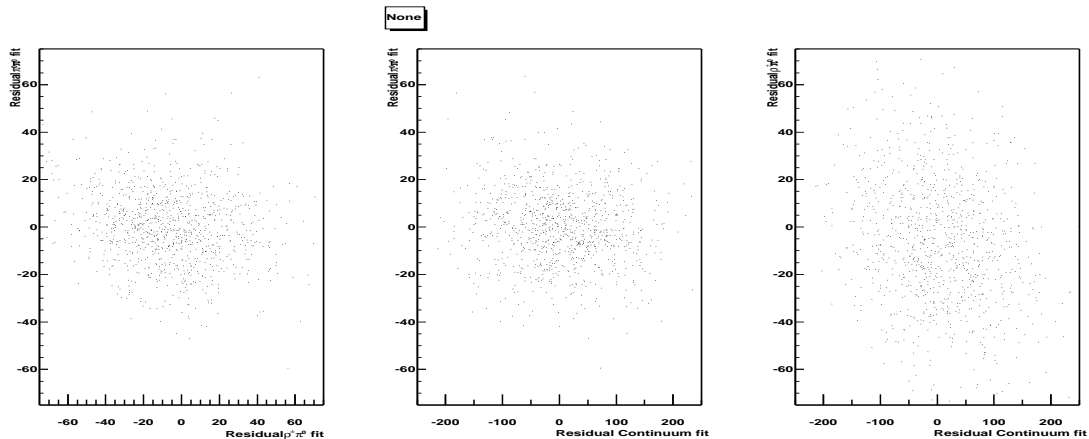
Figure 5.15: The fit residuals (fitted - expected) from 1000 toy Monte Carlo studies for each fit component plotted against each other to show the presence of correlations. The left hand plot shows the residuals for $B^0 \to \pi^0\pi^0$ against $B^{\pm} \to \rho^{\pm}\pi^0$, the centre plot shows $B^0 \to \pi^0\pi^0$ against continuum, and the right hand plot shows $B^{\pm} \to \rho^{\pm}\pi^0$ against continuum. The $B^0 \to \pi^0\pi^0$:$B^{\pm} \to \rho^{\pm}\pi^0$ correlation factor is -0.16
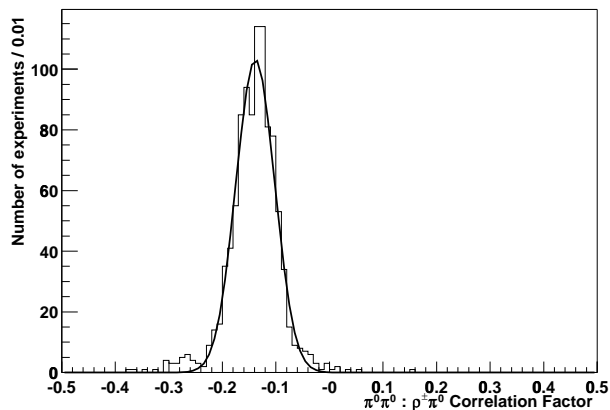
Figure 5.16: An example of the fit correlation for the $B^0 \to \pi^0 \pi^0$ and $B^\pm \to \rho^\pm \pi^0$ components taken from 1000 toy Monte Carlo experiments. The distribution is fitted with a Gaussian and the correlation is extracted from the Minuit correlation matrix once the fit has been performed. The mean of the fitted Gaussian is -0.14. and the RMS of the distribution is 0.04.

Cut $< |\cos(\theta_S)|$	$B^0 \to \pi^0 \pi^0$ efficiency %	Mean Significance	$B^0 \to \pi^0 \pi^0$ Pull central value	Correlation
0.90	26.7	2.913 ± 0.042	-0.167 ± 0.034	-0.114
0.85	25.1	2.693 ± 0.041	-0.137 ± 0.032	-0.164
0.80	23.5	2.687 ± 0.042	-0.051 ± 0.033	-0.084
0.75	21.9	2.712 ± 0.042	-0.065 ± 0.034	-0.159
0.70	20.4	2.865 ± 0.038	-0.001 ± 0.035	-0.166
0.65	18.9	2.801 ± 0.041	-0.082 ± 0.032	-0.133
0.60	17.4	2.806 ± 0.043	-0.061 ± 0.034	-0.112
0.55	15.8	2.752 ± 0.043	0.053 ± 0.032	-0.172
0.50	14.3	2.698 ± 0.044	-0.014 ± 0.033	-0.121

Table 5.5: The results of the maximum likelihood optimisation procedure showing the expected significance from Toy Monte-Carlo studies and parameters related to the quality of the fit for $B^0 \to \pi^0 \pi^0$, the pull on the fitted $B^0 \to \pi^0 \pi^0$ component and the correlation between the $B^0 \to \pi^0 \pi^0$ and $B^\pm \to \rho^\pm \pi^0$ components are shown. These studies were undertaken with all the components of the continuum background floating.

5.4.2   Toy MC results for different cuts

Table 5.5 shows the results of the optimisation studies. The cut giving the highest average sensitivity is $|\cos(\theta_S)| < 0.9$ which has the highest signal efficiency and would give an average significance of 2.9 for a $B^0 \to \pi^0 \pi^0$ branching ratio of 2×10^{-6}. However this cut and that at $|\cos(\theta_S)| < 0.85$ give negative pulls for the signal $B^0 \to \pi^0 \pi^0$ component. All the other studies show no trend for significant $B^0 \to$

$\pi^0\pi^0$ pulls. The reason for this may be that the number of background events is very high for these two studies and this combined with the floating continuum parameters creates the negative bias for the relatively small $B^0 \to \pi^0\pi^0$ component. For a cut at $|\cos(\theta_S)| < 0.9$ we have 24,500 continuum events, for $|\cos(\theta_S)| < 0.85$ there are 14,500 continuum events and 10,000 for $|\cos(\theta_S)| < 0.8$. When the same study was performed but with fixed continuum components there were no biases from the studies.

As the primary goal is to achieve an accurate result for $B^0 \to \pi^0\pi^0$, the chosen optimisation cut is $|\cos(\theta_S)| < 0.70$ which gives the greatest average significance of those studies which show no biases. This cut gives a signal efficiency of 20.4% and an expected statistical significance of 2.865 ± 0.038 for $\mathcal{B}(B^0 \to \pi^0\pi^0) = 2 \times 10^{-6}$. We can also see from the studies that the correlation between the fitted $B^0 \to \pi^0\pi^0$ and $B^\pm \to \rho^\pm\pi^0$ component is approximately 15% with no particular relation to the cut in $|\cos(\theta_S)|$. The results for this optimisation also show the additional significance that can be achieved by using a ML fit rather than the cut and count analysis. Table 4.5 shows that the cut and count analysis should have a significance of 2.04, while the ML should give 2.87 for the same input branching fractions.

5.5   Maximum Likelihood Fit validation

In this section a series of fit validations are performed using Monte Carlo event and data samples, toy Monte Carlo studies and studies using both toy and full Monte Carlo. Before going on it is worth restating the floating parameters of the fit:

1. The number of $B^0 \to \pi^0\pi^0$ events.

2. The number of $B^\pm \to \rho^\pm\pi^0$ events.

3. The number of continuum events.

4. The ξ Argus parameter describing the continuum m_{ES} distribution.

5. The two parameters of the 2nd order polynomial describing the continuum ΔE distribution.

6. The five parameters of the double Gaussian describing the continuum $\mathcal{F}$ distribution.

5.5.1   Fits to data and MC samples

Having performed the optimisation, the first check performed on the fitting technique was to apply it to samples of $B^0 \to \pi^0\pi^0$ Monte Carlo, $B^\pm \to \rho^\pm\pi^0$ Monte Carlo, continuum Monte Carlo, off-resonance data and on-resonance sideband data. The results of these tests are shown in Table 5.6. To perform the fits to pure samples of the signal B modes, it was necessary to fix the continuum PDF's rather than allowing them to float so the fit could give reasonable results. The nominal fit region was used for these studies except for the on-resonance lower and upper sidebands where additional selection given by $(-0.4 < \Delta E < -0.2\,\mathrm{GeV})$ and $(0.2 < \Delta E < 0.4\,\mathrm{GeV})$ were applied.

| Data | Fitted number of events | | |
Sample	$B^0 \to \pi^0\pi^0$	$B^\pm \to \rho^\pm\pi^0$	Continuum
$B^0 \to \pi^0\pi^0$ MC	29,950.9 ± 182.7	-324.3 ± 61.5	-7.42 ± 3.99
$B^\pm \to \rho^\pm\pi^0$ MC	-8.0 ± 19.3	20,604 ± 145.2	2.07 ± 11.0
Continuum MC	7.4 ± 12.3	-3.7 ± 1.2	4,581.5 ± 71.4
On-resonance lower sideband	-9.6 ± 6.1	13.3 ± 9.1	2,138.0 ± 47.3
On-resonance upper sideband	3.7 ± 6.9	-6.3 ± 7.7	1,238.7 ± 36.2

Table 5.6: The number of events reported for fits to various data and Monte Carlo samples.

The results are extremely encouraging as the fit appears to always correctly identify the different components even though the statistics and nature of each fit can vary significantly. There is no sign of any significant crossfeed between the $B^0 \to \pi^0\pi^0$ and $B^\pm \to \rho^\pm\pi^0$ components, one of the problems seen by previous attempts to perform this analysis [47]. One interesting result is the fit to the on-resonance lower sideband. This is the region in which we would expect to see $B^\pm \to \rho^\pm\pi^0$ events and while we see 13 events, for $\mathcal{B}(B^\pm \to \rho^\pm\pi^0) = 2 \times 10^{-5}$ and with a final

efficiency of 4.3%, we would expect 77 $B^\pm \to \rho^\pm \pi^0$ events. The toy Monte Carlo studies performed in section 5.4.2 gave biases in the $B^\pm \to \rho^\pm \pi^0$ component which averaged -0.2σ. That is to say that the $B^\pm \to \rho^\pm \pi^0$ pull distribution was centered at -0.2. While the $B^0 \to \pi^0 \pi^0$ component was not affected, it is clear that the $B^\pm \to \rho^\pm \pi^0$ component is partly absorbed into the continuum component within the fit. It is therefore true to say that any number of $B^\pm \to \rho^\pm \pi^0$ that we finally fit will not give an accurate indication as to the branching fraction of $B^\pm \to \rho^\pm \pi^0$, but it is still necessary to include this component in the fit so not to bias the $B^0 \to \pi^0 \pi^0$ result.

Overall we conclude that the fit performs well and seems capable, within the accuracy of our own Monte Carlo samples, to distinguish the different fit components.

5.5.2   Toy MC studies for different fit configurations

Toy Monte Carlo studies were performed to examine the correctness of the fitting procedure and the potential correlations between the fit components. As the levels of $B^0 \to \pi^0 \pi^0$ and $B^\pm \to \rho^\pm \pi^0$ are not well understood, we performed many different experiments, varying the numbers of $B^0 \to \pi^0 \pi^0$ and $B^\pm \to \rho^\pm \pi^0$ generated, and using a set number of continuum background determined by the number of on-resonance events passing the optimised cuts. This combination allows us to effectively simulate the different scenarios we may face in the data sample. Poissonian fluctuations about the pre-determined mean number were applied to each generated component individually. Each toy Monte Carlo study consisted of 1000 sample experiments and the pulls and correlations were determined for each component using the methods set out in section 5.4.

Table 5.7 shows the results of the various toy studies. While for most individual studies we see negative pulls for $B^0 \to \pi^0 \pi^0$, there is no trend in this direction with input branching fraction. One of the reasons that we see small negative pulls for most of the studies is that for small numbers of fitted $B^0 \to \pi^0 \pi^0$ we can expect a slightly asymmetric pull distribution. This effect is documented in [48] and we

$\mathcal{B}(B^0 \to \pi^0\pi^0)$ $(\times 10^{-6})$	$\mathcal{B}(B^\pm \to \rho^\pm\pi^0)$ $(\times 10^{-5})$	$B^0 \to \pi^0\pi^0$ Pull central value	Correlation
1	1	-0.058 ± 0.033	-0.187
1	2	-0.104 ± 0.034	-0.116
1	3	0.064 ± 0.033	-0.170
2	1	-0.153 ± 0.030	-0.143
2	2	-0.092 ± 0.031	-0.118
2	3	-0.023 ± 0.033	-0.169
3	1	-0.059 ± 0.033	-0.164
3	2	-0.039 ± 0.035	-0.118
3	3	-0.037 ± 0.033	-0.150

Table 5.7: The results of toy Monte-Carlo studies for different input branching fractions for $B^0 \to \pi^0\pi^0$ and $B^\pm \to \rho^\pm\pi^0$. Parameters related to the quality of the fit for $B^0 \to \pi^0\pi^0$, the pull on the fitted $B^0 \to \pi^0\pi^0$ component and the correlation between the $B^0 \to \pi^0\pi^0$ and $B^\pm \to \rho^\pm\pi^0$ components are shown. These studies were undertaken with all the components of the continuum background floating and with a cut at $|\cos(\theta_S)| < 0.7$.

can see that as the $B^0 \to \pi^0\pi^0$ branching fraction increases, so the pull tends more towards zero.

The effect is however small, and this study shows that the fit performs well in identifying the $B^0 \to \pi^0\pi^0$ component whatever the possible branching fraction of $B^0 \to \pi^0\pi^0$ or $B^\pm \to \rho^\pm\pi^0$. The correlation between $B^0 \to \pi^0\pi^0$ and $B^\pm \to \rho^\pm\pi^0$ is consistent with what we saw in section 5.4.2 and this level of correlation does not appear to effect our ability to fit $B^0 \to \pi^0\pi^0$.

5.5.3   Toy MC studies using full $B^0 \to \pi^0\pi^0$ and $B^\pm \to \rho^\pm\pi^0$ MC events

One of the key checks that CLEO [49] used to evaluate whether they could successfully fit for $B^0 \to \pi^0\pi^0$ was to use toy MC studies with full $B^0 \to \pi^0\pi^0$ and $B^\pm \to \rho^\pm\pi^0$ Monte Carlo events. This serves two purposes; firstly it provides a validation technique for the other toy studies that we perform in this analysis and, more importantly, it validates the ability of the fit to accurately measure the number of $B^0 \to \pi^0\pi^0$ events in the data sample assuming that the full Monte Carlo simulation accurately represents the data.

While there are a relatively high number of events in both the $B^0 \to \pi^0\pi^0$ and $B^{\pm} \to \rho^{\pm}\pi^0$ Monte Carlo samples to perform these studies, there are clearly not enough statistics available in the continuum samples. For these studies it is therefore necessary to generate toy Monte Carlo data sets for the continuum component before mixing in pre-defined numbers of $B^0 \to \pi^0\pi^0$ and $B^{\pm} \to \rho^{\pm}\pi^0$ events. The PDF's described in section 5.3.4 were used to generated the continuum data sample.

These studies were performed in exactly the same way as the other toy studies presented in this analysis. For each study a mean number of $B^0 \to \pi^0\pi^0$, $B^{\pm} \to \rho^{\pm}\pi^0$ and continuum events was determined. The exact number for each component within each experiment was varied using Poissonian statistics about the pre-defined mean. The continuum sample was first generated before random $B^0 \to \pi^0\pi^0$ and $B^{\pm} \to \rho^{\pm}\pi^0$ full Monte Carlo events were added at the required level. The complete data sample was then analysed with the nominal fit with floating continuum fit parameters and this process was repeated 1000 times per study. Once again studies were performed for all the likely scenarios we might see in the on-resonance data sample with the number of $B^0 \to \pi^0\pi^0$ and $B^{\pm} \to \rho^{\pm}\pi^0$ events varied to match the possible branching fractions we might expect. Additionally no limits were set on the fitted number of events so both the $B^0 \to \pi^0\pi^0$ and $B^{\pm} \to \rho^{\pm}\pi^0$ components were allowed to return negative values for these studies.

An additional factor in the fit became apparent during these studies. The 2-D Keys described in section 5.3.2 relies on building a PDF from the contribution of 2-D Gaussian probability kernals representing each of the $B^0 \to \pi^0\pi^0$ or $B^{\pm} \to \rho^{\pm}\pi^0$ Monte Carlo events across the $m_{ES} : \Delta E$ plane. The width of the Gaussian kernals is initially determined by the number of events and the various dimensions of the fit. Table 5.8 shows the results of performing toy studies with full $B^0 \to \pi^0\pi^0$ and $B^{\pm} \to \rho^{\pm}\pi^0$ Monte Carlo but with various kernal bandwidths applied to generate the Keys PDF's. The Keys bandwidth factor represents a multiple of the standard generation bandwidth.

We can see that as the bandwidth increases and the number of fitted $B^0 \to \pi^0\pi^0$ increases, so we see postive biases develop in the fitted $B^0 \to \pi^0\pi^0$ result. As the

$\mathcal{B}(B^0 \to \pi^0\pi^0)$	$\mathcal{B}(B^\pm \to \rho^\pm\pi^0)$	$B^0 \to \pi^0\pi^0$ pull for different bandwidths				
$(\times 10^{-6})$	$(\times 10^{-5})$	0.3	0.6	1.0	1.3	1.6
1	1	-0.081	-0.055	-0.052	0.038	0.029
1	2	-0.101	-0.078	-0.005	0.021	0.064
1	3	-0.061	-0.015	-0.018	-0.024	-0.045
2	1	-0.028	-0.103	0.048	0.070	0.115
2	2	-0.038	0.011	0.090	0.027	0.164
2	3	0.045	0.023	0.030	0.107	0.159
3	1	-0.026	-0.028	0.086	0.124	0.244
3	2	0.018	-0.039	0.185	0.154	0.232
3	3	-0.075	-0.009	0.090	0.209	0.233

Table 5.8: The $B^0 \to \pi^0\pi^0$ central pull values from toy Monte Carlo studies (using full Monte Carlo events for $B^0 \to \pi^0\pi^0$ and $B^\pm \to \rho^\pm\pi^0$) where different bandwidths have been used to generate the 2-D Keys PDF and different input branching fractions have been used for $B^0 \to \pi^0\pi^0$ and $B^\pm \to \rho^\pm\pi^0$. The error on each pull reported is between 0.03 and 0.04.

bandwidth is decreased the bias disappears. This effect can only be seen by using full $B^0 \to \pi^0\pi^0$ and $B^\pm \to \rho^\pm\pi^0$ Monte Carlo events, as in regular toy studies we are simply generating and fitting with identical PDF's. The effect can be understood by looking at the PDF's generated by the different bandwidths.
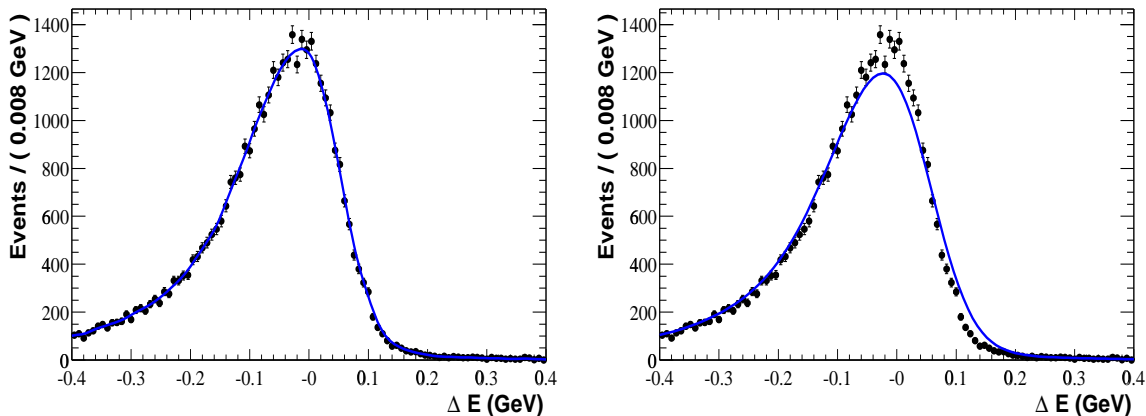
Figure 5.17: The $B^0 \to \pi^0\pi^0$ ΔE distribution with the generated Keys PDF overlayed for a Keys PDF generated using a small (0.3× nominal) Gaussian bandwidth (left) and a larger (1.6× nominal) Gaussian bandwidth (right).

Figure 5.17 shows the ΔE distribution for $B^0 \to \pi^0\pi^0$ generated with small and large bandwidths. The larger bandwith gives a smooth PDF but over and under-estimates the actual $B^0 \to \pi^0\pi^0$ distribution, while the smaller bandwidth almost perfectly models the events used to generate it. The larger bandwidths could clearly create biases within the fit.

If we kept decreasing the bandwidths we would perfectly model the Monte Carlo sample used to generate the 2-D Keys PDF, effectively we would produce a PDF that was a series of δ functions across the $m_{ES} : \Delta E$ plane. Obviously this does not accurately represent the situation in data as the Monte Carlo samples used in these studies to create and then test the Keys PDF are a statistically limited snap shot of what we should expect the distributions to be. Additionally moving to very small bandwidths may leave parts of the $m_{ES} : \Delta E$ plane with gaps in the 2-D Keys PDF due to the statistical limits of the Monte Carlo samples for $B^0 \to \pi^0\pi^0$ and $B^\pm \to \rho^\pm\pi^0$.

With this in mind, the nominal bandwidth adjusted by a factor of 0.6 was used to give the best pull results for $B^0 \to \pi^0\pi^0$ while retaining a generated PDF which is relatively smooth and covers the whole $m_{ES} : \Delta E$ plane effectively. All the studies prior to this, and the PDF's shown in section 5.3.3 were performed using this bandwidth factor so all the previous results are valid for the analysis.

In conclusion we see that using a bandwith which is 0.6 of the nominal gives the best results and allows the fit to accurately determine the number of $B^0 \to \pi^0\pi^0$ events when full $B^0 \to \pi^0\pi^0$ and $B^\pm \to \rho^\pm\pi^0$ Monte Carlo events are used in the toy studies and various $B^0 \to \pi^0\pi^0$ and $B^\pm \to \rho^\pm\pi^0$ branching fractions are used. If we believe that the Monte Carlo simulation accurately models the distributions from real $B^0 \to \pi^0\pi^0$ and $B^\pm \to \rho^\pm\pi^0$ events, then the fit can accurately measure the $B^0 \to \pi^0\pi^0$ component in the on-resonance data sample.

5.6   Conclusions and Final Fit configuration

This chapter has documented the maximum likelihood strategy used to fit for $B^0 \to \pi^0\pi^0$ in the on-resonance data sample. The fit consists of the m_{ES}, ΔE and $\mathcal{F}$ variables and has signal $B^0 \to \pi^0\pi^0$, $B^\pm \to \rho^\pm\pi^0$ and continuum components. The fit is made up of a series of PDF's to describe each variable for the components, and a 2-D Keys PDF for the $m_{ES} - \Delta E$ variables for both the $B^0 \to \pi^0\pi^0$ and $B^\pm \to \rho^\pm\pi^0$

components. The Keys PDF uses an adjusted bandwidth so as to accurately fit the $B^0 \to \pi^0\pi^0$ and $B^\pm \to \rho^\pm\pi^0$ components, and the continuum PDF parameters are determined within the final fit. An optimised cut on $|\cos(\theta_S)| < 0.7$ is used for the analysis. Toy Monte Carlo studies with various input $B^0 \to \pi^0\pi^0$ and $B^\pm \to \rho^\pm\pi^0$ branching fractions and using full $B^0 \to \pi^0\pi^0$ and $B^\pm \to \rho^\pm\pi^0$ events show that the fit can determine the number of $B^0 \to \pi^0\pi^0$ events without any bias.

Chapter 6

Results and Conclusions

6.1   Introduction

Chapters 4 and 5 documented the cut and count and maximum likelihood analysis structure respectively for measuring $B^0 \to \pi^0\pi^0$ at *BABAR*. This chapter documents the systematic errors and then presents the results of both analyses.

6.2   Systematic Errors

6.2.1   Neutral efficiency corrections

The neutral correction applied to the standard Monte Carlo events for $B^0 \to \pi^0\pi^0$ and $B^{\pm} \to \rho^{\pm}\pi^0$ was discussed in section 4.4. While this automatically provides an efficiency correction and a correction for the PDF shapes for m_{ES}, ΔE and $\mathcal{F}$ there are systematic uncertainties associated with the correction. The neutral working group at *BABAR* who developed the correction recommend that an additional 5% systematic error should be applied to the reconstructed $B^0 \to \pi^0\pi^0$ and $B^{\pm} \to \rho^{\pm}\pi^0$ efficiencies for every π^0 in the reconstruction [41]. This means a 10% error on the corrected $B^0 \to \pi^0\pi^0$ and $B^{\pm} \to \rho^{\pm}\pi^0$ efficiency.

Additionally there is another systematic for the $B^0 \to \pi^0\pi^0$ and $B^\pm \to \rho^\pm\pi^0$ ΔE distributions. In the *BABAR* $B^\pm \to \pi^\pm\pi^0$ analysis [25], the central value for the signal ΔE distribution is one of the parameters in the final ML fit. The comparison between the fitted central value in data and that from the neutral corrected Monte Carlo events allows a systematic error to be derived for the ΔE distribution. In the full $81\,\mathrm{fb}^{-1}$ sample the mean value of ΔE is fitted as $-9.4 \pm 5.2\,\mathrm{MeV}$, while in the corrected Monte Carlo it is $-11.2 \pm 0.2\,\mathrm{MeV}$. These two results show good agreement. From this we derive a conservative systematic of $\pm 10.4\,\mathrm{MeV}$ for the central ΔE value for $B^0 \to \pi^0\pi^0$ and $B^\pm \to \rho^\pm\pi^0$ distributions. This is derived by taking the uncertainty on the fitted $B^\pm \to \pi^\pm\pi^0$ ΔE central value and doubling it to take account of the two π^0's in the $B^0 \to \pi^0\pi^0$ and $B^\pm \to \rho^\pm\pi^0$ reconstruction. This correction is applied to the ML fit by shifting both the $B^0 \to \pi^0\pi^0$ and $B^\pm \to \rho^\pm\pi^0$ distributions in the $m_{ES} : \Delta E$ plane by $\pm 10.4\,\mathrm{MeV}$ in ΔE and then generating new 2D Keys PDF's which are then used in the fit.

6.2.2   PDF variations

The greatest source of systematic error in the ML fit comes from the uncertainty in the PDF shapes that make up the fit. These are typically taken into account by changing the PDF's within some systematic error and reperforming the fit to find the change in signal yield. One of these systematics has been discussed in the previous section through the variation in the $B^0 \to \pi^0\pi^0$ and $B^\pm \to \rho^\pm\pi^0$ ΔE central values. Typically in other two-body analyses and in previous versions of this analysis, the largest source of systematic comes from the variation of the continuum parameters. For this analysis we do not suffer from this as each continuum PDF for m_{ES}, ΔE and $\mathcal{F}$ is floated in the final fit and so is determined from the on-resonance data themselves. This does of course increase the statistical error from the final fit. For the cut and count analysis we predict the number of continuum background events by using the Argus function. The systematic error in the predicted number comes from varying the Argus parameter ξ within its error and seeing how this changes the expected number of continuum events.

The next largest source typically comes from the variation of the $\mathcal{F}$ PDF for $B^0 \to \pi^0\pi^0$ and $B^\pm \to \rho^\pm\pi^0$. These PDF's are determined from the corrected Monte Carlo events. As the $\mathcal{F}$ discriminant relies only on the basic properties of the tracks and clusters in the event, such as the momentum and the angular distribution, the Monte Carlo simulation recreates this distribution well. The primary systematic for these variables comes from the statistical error on the parameters making up the PDF's. Typically the systematic is determined by varying each parameter of the double Gaussian parameterisation within its statistical limits, refitting the data sample, and adding the variation in the $B^0 \to \pi^0\pi^0$ yield in quadrature to get an overall systematic error. This assumes that the parameters of the double Gaussian are uncorrelated, which is not the case. To take account of the correlations we can diagonalise the error matix for the parameters, shifting the eigenvectors by 1σ, and then transforming back to the correlated parameter space. The procedure and mechanics is further outlined in [50]. Once this has been done the systematic error is calculated by using the shifted parameters in the fit and seeing the variation in the $B^0 \to \pi^0\pi^0$ result as compared to the nominal fit result.

The m_{ES} distribution for $B^0 \to \pi^0\pi^0$ and $B^\pm \to \rho^\pm\pi^0$ is insensitive to the neutral corrections, meaning that the only PDF variations in the fit come from ΔE and $\mathcal{F}$ for $B^0 \to \pi^0\pi^0$ and $B^\pm \to \rho^\pm\pi^0$.

6.2.3   B counting

The final source of systematic error comes from the number of B mesons in the on-resonance data samples. The number is determined by the B-counting group at *BABAR* [51] and comes from the study of well understood physics processes to benchmark the number of $B\overline{B}$ events contained in the *BABAR* data sample. The error due to this systematic is 1.6%, so giving $(87.9 \pm 1.4) \times 10^6$ $B\overline{B}$ events and hence the same number of B^0 and $\overline{B}^0$ mesons, assuming equal production of B^+B^- and $B^0\overline{B}^0$.

6.3   Analysis Results

6.3.1   Maximum Likelihood Analysis Results

Fit Component	Result
$B^0 \to \pi^0 \pi^0$	36^{+15}_{-14}
$B^\pm \to \rho^\pm \pi^0$	33^{+20}_{-17}
Continuum	6471 ± 83
Statistical significance	$3.1\ \sigma$
Upper Limit $(90\% CL)$	56.9

Table 6.1: The results of the fit to the full on-resonance data sample.

Table 6.1 shows the results of the maximum likelihood fit to the on-resonance sample. The statistical significance is determined by using the difference in $-ln(L)$ between the full fit and the case where the $B^0 \to \pi^0 \pi^0$ component is set to zero as shown in equation 5.8. The upper limit of the number of events N_{UL} is determined by numerical integration of the likelihood function, $L(N)$, as a function of fitted $B^0 \to \pi^0 \pi^0$ yield N where

$$\frac{\int_0^{N_{UL}} L(N)dN}{\int_0^\infty L(N)dN} = 0.9. \tag{6.1}$$

This gives the statistical 90% CL upper limit before systematic errors are included. The likelihood function is shown in figure 6.1. To check the goodness of the fit, 1000 toy Monte Carlo studies were performed using the full fit result and the value of $-ln(L)$ from the full fit result was compared with those from the toy studies. The result is shown in figure 6.2 where the arrow shows the full fit value.

Figure 6.3 shows the full fit result on the data for m_{ES}, ΔE and $\mathcal{F}$. As this shows all events over the GSB as well as signal region, it is very difficult to determine whether there are any $B^0 \to \pi^0 \pi^0$ or $B^\pm \to \rho^\pm \pi^0$ events in the sample. To overcome this we can make an optimised cut on the probability ratio for the event to be signal $B^0 \to \pi^0 \pi^0$. For each event we define $\mathcal{R} = n_{\pi^0\pi^0}\mathcal{P}_{\pi^0\pi^0}/(n_{\pi^0\pi^0}\mathcal{P}_{\pi^0\pi^0} + n_{\rho\pi^0}\mathcal{P}_{\rho\pi^0} + n_{cont}\mathcal{P}_{cont})$ where n is the number seen of each component in the full fit, while $\mathcal{P}$ is the probability of the individual event being a specific type. From toy Monte Carlo studies of the three types of event $B^0 \to \pi^0 \pi^0$, $B^\pm \to \rho^\pm \pi^0$ and continuum it is
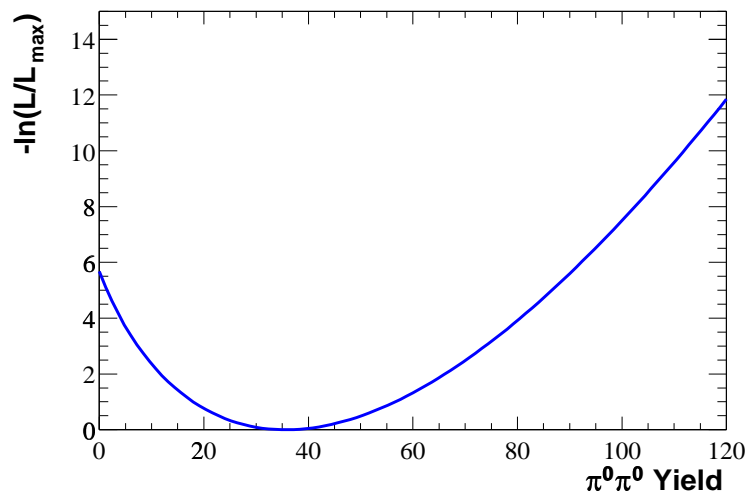
Figure 6.1: The distribution of $-ln(L/L_{max})$ against $B^0 \to \pi^0\pi^0$ yield for the ML fit.
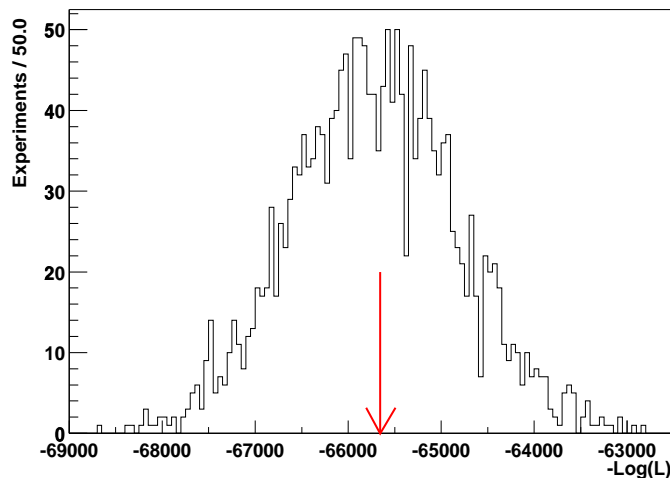
Figure 6.2: The distribution of $-(L_{max})$ for 1000 toy Monte Carlo experiments with the full ML fit result as the input number of events generated. The arrow represents the value obtained from the fit to the data sample.

possible to plot the expected value of the significance $s = S/(\sqrt{S+B})$ for a cut on $\mathcal{R}$ using all but the one variable we want to plot in the calculation of the probability.

Figure 6.4 shows the distribution of s against $\mathcal{R}$ for m_{ES}. We select the most significant point which is given by the peak in the distribution and place a cut on $\mathcal{R}$ to select the data most likely to be $B^0 \to \pi^0\pi^0$. From the toy Monte Carlo
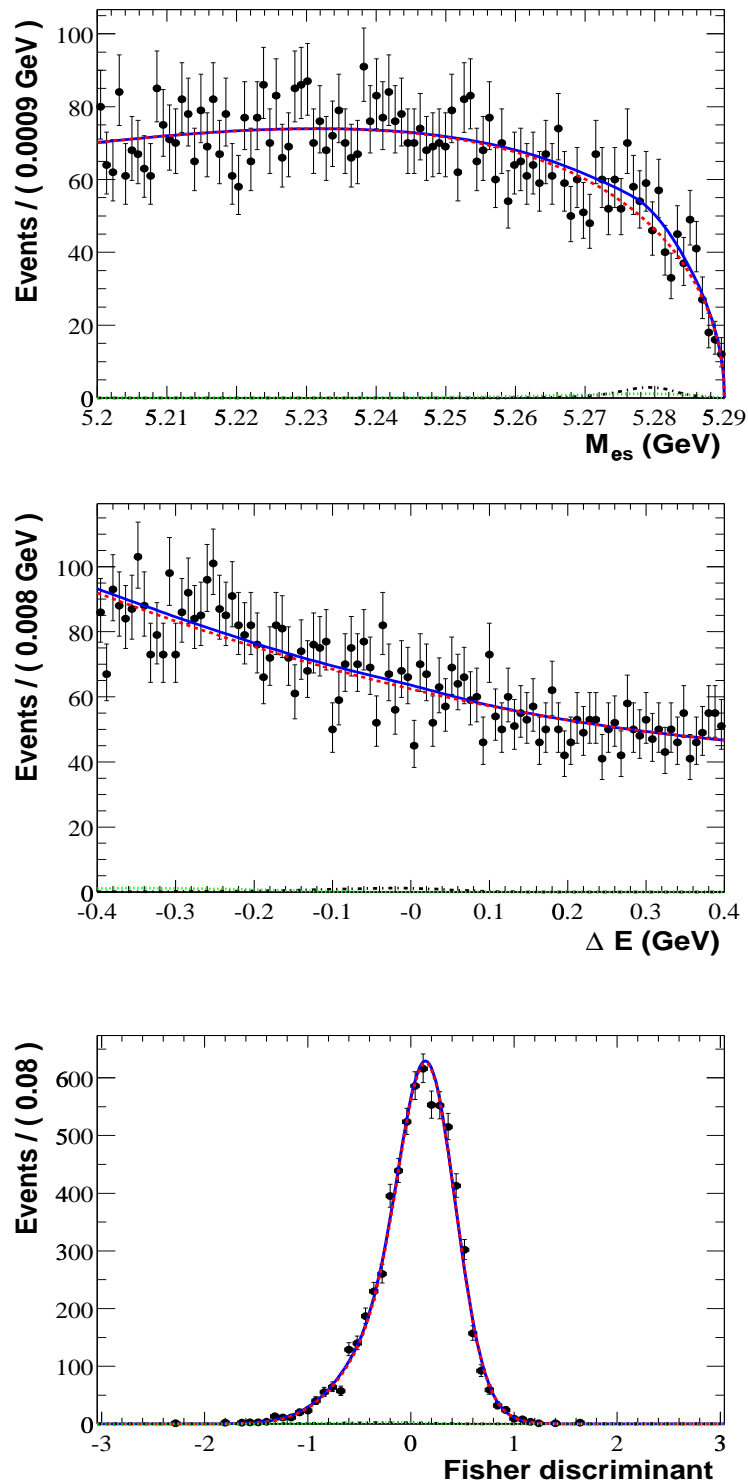
Figure 6.3: The projections of the ML fit on the full data sample. The top plot shows the m_{ES} distribution, the central plot is the ΔE distribution and the bottom is the $\mathcal{F}$ distribution. The solid (blue) curve represents the total PDF, the dashed (red) is the continuum PDF projection, the dotted (black) curve is the $B^0 \to \pi^0\pi^0$ projected PDF and the heavy dashed (green) is the $B^\pm \to \rho^\pm\pi^0$ projected PDF.
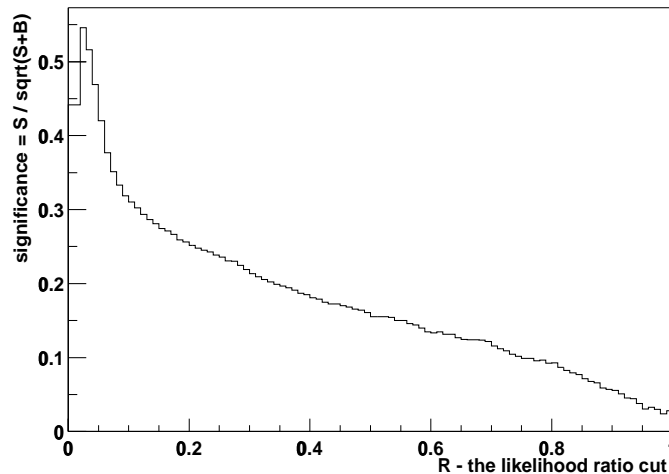
Figure 6.4: The significance $s = S/\sqrt{S+B}$ as a function of a cut on the probability ratio $\mathcal{R} = n_{\pi^0\pi^0}\mathcal{P}_{\pi^0\pi^0}/(n_{\pi^0\pi^0}\mathcal{P}_{\pi^0\pi^0} + n_{\rho\pi^0}\mathcal{P}_{\rho\pi^0} + n_{cont}\mathcal{P}_{cont})$, using $\mathcal{F}$ and ΔE in the probability

studies we can tell how the efficiency for each fit component should be effected, so it is possible to rescale the fit to take account of the imposed cut on the data. This optimisation is done separately for each variable. The peak value of s shown in figure 6.4 is far smaller than one might expect from the cut-based analysis or indeed from the ML analysis. This is because in calculating s for one of the variables no selection is made using that variable. For example for m_{ES} the entire region between $(5.20 - 5.29\,\mathrm{GeV})$ is used which includes large numbers of background events which in turn gives low values of s. Figure 6.5 shows the distributions for m_{ES}, ΔE and $\mathcal{F}$ with an optimised cut on $\mathcal{R}$ applied.

Systematic source	Upper error (events)	Lower error (events)
$B^0 \to \pi^0\pi^0$ ΔE shift	$+0.5$	-0.5
$B^\pm \to \rho^\pm\pi^0$ ΔE shift	$+0.7$	0
$B^0 \to \pi^0\pi^0$ $\mathcal{F}$ PDF	$+0.3$	-0.3
$B^\pm \to \rho^\pm\pi^0$ $\mathcal{F}$ PDF	$+0.3$	-0.3
Total PDF error on yield	$+1.0$	-0.7

Table 6.2: The systematic errors on the $B^0 \to \pi^0\pi^0$ yield from the PDF shapes for ΔE and $\mathcal{F}$.

Tables 6.2 and 6.3 show a summary of the systematic errors that effect the ML fit from the variation of the PDF's and from the efficiency from B counting and
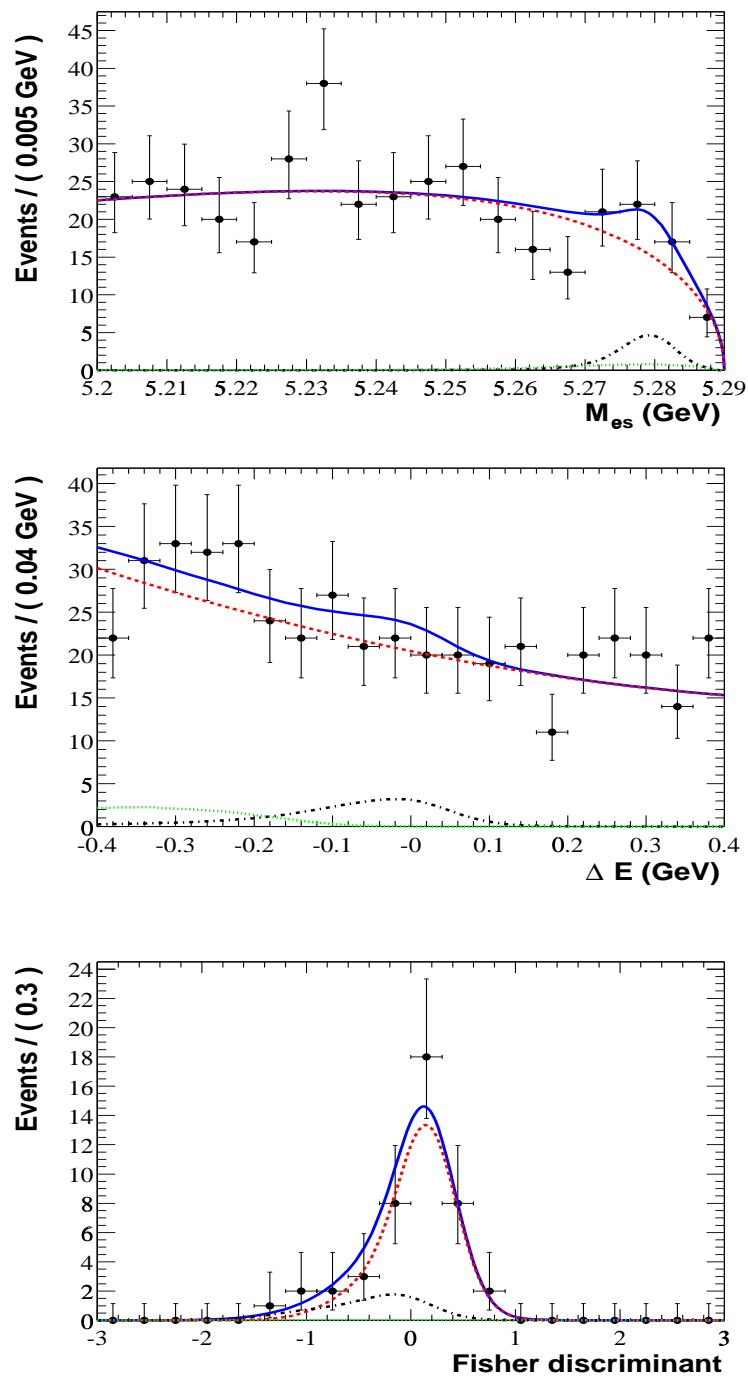
Figure 6.5: The projections of the ML fit on reduced data samples corresponding to cuts on the ratio $\mathcal{R} = n_{\pi^0\pi^0}\mathcal{P}_{\pi^0\pi^0}/(n_{\pi^0\pi^0}\mathcal{P}_{\pi^0\pi^0} + n_{\rho\pi^0}\mathcal{P}_{\rho\pi^0} + n_{cont}\mathcal{P}_{cont})$ to maximise the significance of the signal $B^0 \to \pi^0\pi^0$. The top plot shows the m_{ES} distribution, the central plot is the ΔE distribution and the bottom is the $\mathcal{F}$ distribution. The solid (blue) curve represents the total PDF, the dashed (red) is the continuum PDF projection, the dotted (black) curve is the $B^0 \to \pi^0\pi^0$ projected PDF and the heavy dashed (green) is the $B^{\pm} \to \rho^{\pm}\pi^0$ projected PDF. The optimised cut on $\mathcal{R}$ for each projection are ($\mathcal{R} > 0.0201$) for the m_{ES} projection, ($\mathcal{R} > 0.0302$) for the ΔE projection and ($\mathcal{R} > 0.1501$) for the $\mathcal{F}$ projection.

Systematic source	Error (%)
B Counting	$\pm 1.6\%$
Neutrals	$\pm 10.0\%$
Total Efficiency Error	$\pm 10.1\%$

Table 6.3: The systematic errors on the $B^0 \to \pi^0 \pi^0$ yield from the efficiency corrections.

neutral corrections. The exact source of the systematics are described in section 6.2. When comparing systematic errors to similar analyses at *BABAR* [22], it is clear that the strategy of allowing the continuum PDF parameters to float in the fit has significantly reduced the systematic error that we might have seen for this analysis. The largest sources of systematic error comes from the neutral efficiency correction.

Quantity	Number
$B^0 \to \pi^0 \pi^0$ fitted	$36^{+15\ +1}_{-14\ -1}$
$\epsilon_{B^0 \to \pi^0 \pi^0}$	$(20.4 \pm 2.0)\%$
Number of B Mesons	$(87.9 \pm 1.4)M$
$\mathcal{B}(B^0 \to \pi^0 \pi^0)$	$\left(2.0^{+0.9\ +0.3}_{-0.8\ -0.2} \right) \times 10^{-6}$
Upper Limit of fitted $B^0 \to \pi^0 \pi^0$	56.9
Upper Limit with Systematic	57.9
$\mathcal{B}(B^0 \to \pi^0 \pi^0)$ Upper Limit	$< 3.6 \times 10^{-6}\ (90\% CL)$
Statistical significance	3.1σ

Table 6.4: Summary table of the final numbers for the maximum likelihood analysis. The first error on the $B^0 \to \pi^0 \pi^0$ fitted number and branching fraction is statistical, the second is systematic.

Table 6.4 shows the final numbers for the analysis. The branching fraction for $B^0 \to \pi^0 \pi^0$ is given by

$$\mathcal{B}(B^0 \to \pi^0 \pi^0) = \frac{N_{B^0 \to \pi^0 \pi^0}}{\left(\epsilon_{B^0 \to \pi^0 \pi^0} \times N_{B\bar{B}} \right)} \tag{6.2}$$

which gives a final branching fraction for $B^0 \to \pi^0 \pi^0$ of

$$\mathcal{B}(B^0 \to \pi^0 \pi^0) = (2.0^{+0.9\ +0.3}_{-0.8\ -0.2}) \times 10^{-6} \tag{6.3}$$

where the first error is statistical and the second is sytematic. The statistical upper-limit from the fit was 56.9 events, adding a one sigma systematic error and calcu-

lating the upper limit gives

$$\mathcal{B}(B^0 \to \pi^0\pi^0) < 3.6 \times 10^{-6}(90\% CL) \tag{6.4}$$

and the statistical significance including the systematic error is found to be 3.1σ. This is determined by using the fits with the systematically altered PDF's and taking the combination of altered PDF's which give the lowest significance. The fact that the significance does not appreciably alter is due to the systematic error being small compared with the statistical error.

6.3.2 Cut and Count analysis results

Selection/Details	Optimisation Results
$m_{ES}(\text{GeV})$	5.274 - 5.286
$\Delta E(\text{GeV})$	-0.16 - 0.08
$\mathcal{F}$	< -0.1
$|\cos(\theta_S)|$	< 0.55
ϵ_{sig}	$(8.2 \pm 0.9)\%$
$N_{B\bar{B}}$	$87.9 \pm 1.4M$
Grand sideband events	285
GSB-signal scaling ratio	0.1319 ± 0.0022
Expected continuum	37.6 ± 2.9
Expected $N_{\rho^{\pm}\pi^0}$	2.7 ± 1.5
Expected total background	40.3 ± 3.3
Actual number of events	55 ± 7.4
Number of signal events	$14.7 \pm 7.4 \pm 3.3$
$\mathcal{B}(B^0 \to \pi^0\pi^0)$	$2.0 \pm 1.0 \pm 0.5 \times 10^{-6}$

Table 6.5: The final results of the cut and count analysis. The first error on number of $B^0 \to \pi^0\pi^0$ events and $\mathcal{B}(B^0 \to \pi^0\pi^0)$ is statistical, the second is systematic.

The validation of the fit result comes from the cut and count analysis. The final numbers for the analysis are shown in figure 6.5. We see 55 events in the signal region with an expected background of 40.3 events. The branching fraction for the cut and count analysis is calculated using equation 6.2 and includes the effect of the neutral correction and B counting systematic. The cut and count analysis gives a branching fraction of

$$\mathcal{B}(B^0 \to \pi^0\pi^0) = 2.0 \pm 1.0 \pm 0.5 \times 10^{-6} \tag{6.5}$$

where the first error is statistical the second systematic. This is in very good agreement with the maximum likelihood fit result given in equation 6.3. Figure 6.6 shows the m_{ES}:ΔE plane for events passing the cut and count selection criteria. It is difficult to see any clear evidence of $B^0 \to \pi^0\pi^0$ signal in this plot.

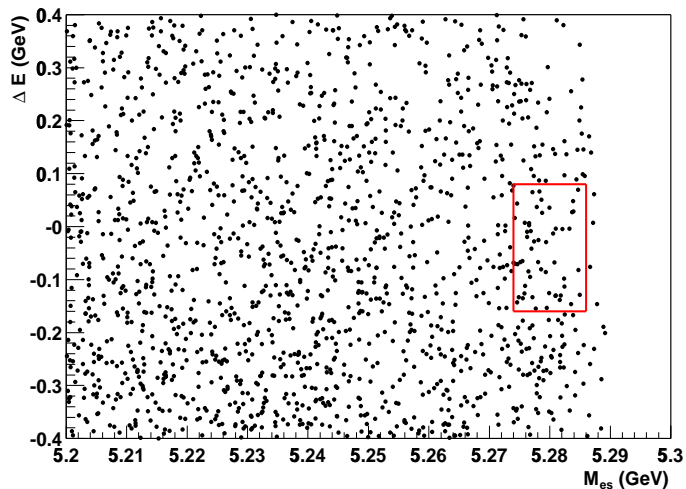**Figure 6.6:** The m_{ES}:ΔE plane for events passing the cut and count selection. The box highlights the optimised signal region.
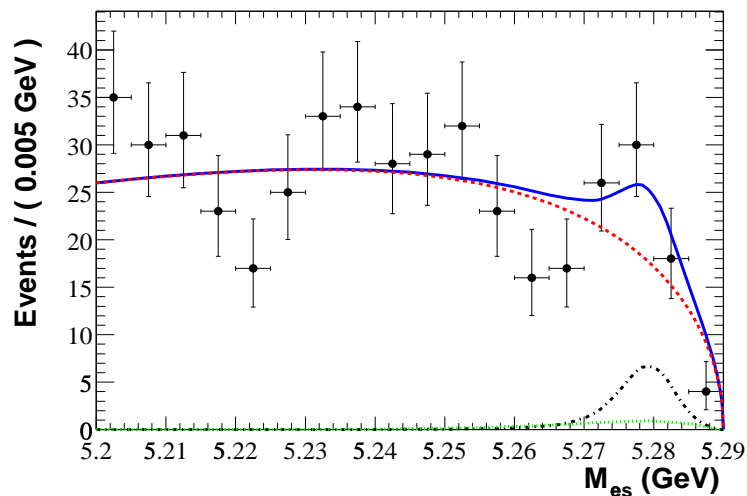
Figure 6.7: The m_{ES} distribution for events passing the cut and count selection criteria apart from the cut on m_{ES} itself. The figures shows the PDF's from the ML fit overlayed and normalised to the expected results of the cut and count. The solid (blue) line shows the total PDF, the dashed (red) line shows the continuum PDF contribution, the black (dot-dashed) shows the $B^0 \to \pi^0\pi^0$ contribution and the green (heavy dashed) shows the $B^{\pm} \to \rho^{\pm}\pi^0$ component.

Figure 6.7 shows the m_{ES} distribution for events passing the cuts except for that

applied to m_{ES}, overlayed are the PDF's from the maximum likelihood fit which have been normalised to the expected number of events from the cut and count result. This shows a much clearer excess of events in the signal $B^0 \to \pi^0\pi^0$ region. Even though the statistical and systematic errors are relatively large for the cut and count analysis, it clearly supports the findings of the maximum likelihood fit.

6.4 Conclusions

In a data sample consisting of 87.9 Million neutral B mesons we have observed $36^{+15}_{-14}{}^{+1}_{-1}$ $B^0 \to \pi^0\pi^0$ events with a significance of 3.1σ and an efficiency of 20.4%. This gives a central value for the branching fraction of

$$\mathcal{B}(B^0 \to \pi^0\pi^0) = (2.0^{+0.9}_{-0.8}{}^{+0.3}_{-0.2}) \times 10^{-6} \tag{6.6}$$

and an upper limit of

$$\mathcal{B}(B^0 \to \pi^0\pi^0) < 3.6 \times 10^{-6}(90\%CL) \tag{6.7}$$

The results are confirmed by a simple cut-based analysis. We can use these results to examine the Grossman-Quinn bound described in section 1.5.3. Using the central value for $\mathcal{B}(B^0 \to \pi^0\pi^0)$ given here and the result for $\mathcal{B}(B^+ \to \pi^+\pi^0) = (5.5^{+1.0}_{-0.9} \pm 0.6) \times 10^{-6}$ [25] we can say that

$$\sin^2(\alpha_{eff} - \alpha) \leq \frac{\langle \mathcal{B}(B^0 \to \pi^0\pi^0)\rangle_{CP}}{\mathcal{B}(B^+ \to \pi^+\pi^0)} = \frac{2.0 \pm 1.0}{5.5 \pm 1.2} \tag{6.8}$$

so

$$(\alpha_{eff} - \alpha) \leq 37°{}^{+17°}_{-15°}. \tag{6.9}$$

It is therefore possible that penguins play a significant role in the various $B \to \pi\pi$ decays and that a full isospin analysis will be necessary to extract α. Recent studies [52] [53] have shown that with similar branching ratios to those presented here, between $5 - 10ab^{-1}$ of data would be required to give reasonable errors on $\sin(2\alpha)$ from a full isospin analysis. That is between 50-100 times more than *BABAR* has collected at present, and is one of the main motivations for an enhanced luminosity B factory which is being discussed within the *BABAR* collaboration [54].

References

[1] C.S. Wu *et al.*, Phys. Rev. 105 (1957) 1413

[2] J.H. Christenson *et al.*, Phys. Rev. Lett. **13**, 138 (1964).

[3] A. D. Sakharov, Pisma Zh. Eksp. Teor. Fiz. **5**, 32 (1967).

[4] B. Aubert *et al.* [BaBar Collaboration], "Observation of CP violation in the B^0 meson system," Phys. Rev. Lett. **87**, 091801 (2001), [hep-ex/0107013].

[5] K. Abe *et al.* [Belle Collaboration], Phys. Rev. Lett. **87**, 091802 (2001), [hep-ex/0107061].

[6] D. E. Groom *et al.*, [Particle Data Group], Eur. Phys. J. **C15**, 1 (2000).

[7] M. Kobayashi and T. Maskawa, Prog. Theor. Phys. **49**, 652 (1973).

[8] L. Wolfenstein, Phys. Rev. Lett. **51** 1945 (1983).

[9] J. R. Batley *et al.* [NA 48 Collaboration], "A precision measurement of direct *CP* violation in the decay of neutral kaons into two pions", Phys. Lett. **B544** 97-112 (2002).

[10] P. F. Harrison and H. R. Quinn [BABAR Collaboration], "The BABAR physics book: Physics at an asymmetric B factory", Section 1, (1998).

[11] "*B* Decays and *CP* violation" M. Neubert, Int. J. Mod. Phys. All,4173 (1996), [hep-ph/9604412].

[12] N. Cabibbo, Phys. Rev. Lett.**10**, 531 (1963).

[13] B. Aubert *et al*, [*BABAR* collaboration] "Measurements of Branching Fractions and *CP*- violating Aysmmetries in $B^0 \to \pi^+\pi^-, K^+\pi^-, K^+K^-$ Decays", Submitted to Phys. Rev. Lett., [hep-ex/0207055], (2002).

[14] M. Gronau and D. London, Phys. Rev. Lett. **65**, 3381 (1990).

[15] Y. Grossman and H. Quinn, Phys. Rev. Lett. **58**, 017504 (1998).

[16] A. Hocker *et al.*, "A New Approach to a Global Fit of the CKM Matrix", Eur. Phys. J. **C21**, 225 (2001), [hep-ph/0104062].

[17] Y. F. Zhou *et al.*, "The interplay between weak and strong phases and direct *CP* violation from Charmless *B*-meson Decays", [hep-ph/0006225].

[18] "Taming the penguin contributions in the $B_d^0 \to \pi^+\pi^-$ *CP* asymmetry: observables and minimal theoretical input", J. Charles, Phys. Rev. D **59** 054007 (1999)

[19] A. Hocker *et al.*,
http://ckmfitter.in2p3.fr/ckm_measure.html

[20] B. Aubert *et al.*,[*BABAR* Collaboration], "Measurement of the *CP*-Violating Asymmetry Amplitude $\sin(2\beta)$" Submitted to Phys. Rev. Lett., [hep-ex/0207042].

[21] K. Abe *et al.* ,[Belle Collaboration] "An improved Measurement of Mixing-induced *CP* Violation in the Neutral *B*-Meson System", Submitted to Phys. Rev. D., [hep-ex/0208025].

[22] B. Aubert *et al.* [*BABAR* Collaboration], "A search for the decay $B^0 \to \pi^0\pi^0$", Contributed to 31st International Conference on High Energy Physics (ICHEP 2002), Amsterdam, The Netherlands, 24-31 Jul 2002, [hep-ex/0207063].

[23] Toru Iijima, "Direct Angles determination at B-Factories", Talk at the Workshop on the CKM Unitarity Triangle, February 2002

http://d.home.cern.ch/d/dimartin/www/ckm/op_plenary/ijima_0213.
pdf''
http://ckm-workshop.web.cern.ch/ckm-workshop/

[24] D. M. Asner *et al.*, [CLEO Collaboration], "Search for $B^0 \rightarrow \pi^0\pi^0$ decay", Phys. Rev. D **65** 031103 (2002).

[25] B. Aubert *et al.* [*BABAR* Collaboration], "Measurements of Branching Fractions and Direct *CP* Asymmetries in $\pi^+\pi^0$, $K^+\pi^0$ and $K^0\pi^0$ B Decays", Contributed to 31st International Conference on High Energy Physics (ICHEP 2002), Amsterdam, The Netherlands, 24-31 Jul 2002, [hep-ex/0207065].

[26] The $PEP-II$ Conceptual Design Report, SLAC-PUB-418, (1993).

[27] The *BABAR* Technical Design Report, SLAC-R-95-457, (1995).

[28] B. Aubert *et al.* [*BABAR* Collaboration], "The *BABAR* Detector", Nucl. Inst. and Methods A**479**, 1. (2002) [hep-ex/105044].

[29] D. Best *et al.*, "Crosstalk in the EMC Front End Electronics", *BABAR* note #550, Version 1, (2002).

[30] J. J. Olsen *et al.*, "*BABAR* DAQ ROM Untriggered Personality Card Description", http://www.slac.stanford.edu/BFROOT/www/Detector/DAQ/ ReadoutModule/rom.html.

[31] S. Menke, "Offline Correction of Non-Linearities in the *BABAR* Electromagnetic Calorimeter Electronics", *BABAR* note #527, Version 1, (2000).

[32] M. Freytag, Private communication.

[33] S. Menke, "Calibration of the *BABAR* Electromagnetic Calorimeter with π^0's", *BABAR* note #528, Version 1, (2000).

[34] T. Skwarnicki, "A Study of the Radiative Cascade Transitions Between the Upsilon-Prime and Upsilon Resonances", DESY F31-86-02 (1986).

[35] P. F. Harrison and H. R. Quinn [BABAR Collaboration], "The BABAR physics book: Physics at an asymmetric B factory," (1998). Section 4.

[36] G. C. Fox and S. Wolfram, Nucl. Phys. **B149**, 413 (1979).

[37] J. D. Bjorken and S.J. Brodsky, Phys. Rev. D**1**, 1416 (1970).

[38] R. A. Fisher, Annals of Eugenics **7**, 179 (1936);
M. S. Srivastava and E.M.Carter, "An introduction to Applied Multivariate Statistics", North Holland, Amsterdam.

[39] J. Ocariz *et al.*, "Background fighting in Charmless Two-body analyses" *BABAR* analysis document # 346, Version 2, (2002).

[40] W. Ford *et al.*, "Choice of Kinematic Variables in B Meson Reconstruction - Take 3", *BABAR* analysis document # 53, Version 5, (2000).

[41] F. Di Lodivico *et al.*, *BABAR* Neutrals Working Group,
http://www.slac.stanford.edu/BFROOT/www/Physics/Analysis/AWG/
Neutrals/validation/results/results.html.

[42] H. Albrecht *et al.*, [ARGUS Collaboration], Phys. Lett. **B185** (1987) 218.

[43] C. P. Jessop *et al.*, [CLEO Collaoboration], "Study of charmless hadronic B meson decays to pseudoscalar-vector final states", Phys. Rev. Lett.**85** 2881, (2000), [hep-ex/0006008]

[44] K. S. Cranmer, "Kernal Estimation for Parameterization of Discriminant Variable Distributions", ALEPH 99-144,
http://www-wisconsin.cern.ch/~cranmer/keys.html

[45] Blind Analysis Task Force and *BABAR* Publications Board, "Draft Guildlines for Blind Analyses in *BABAR*", *BABAR* analysis document #91, Version 1, 2002.

[46] A. Bevan *et al*, "Branching Fraction measurement for the decay $B^0 \rightarrow \pi^0\pi^0$", *BABAR* analysis document #360, Version 7, 2002.

[47] A. Bevan *et al*, "Measurement of Branching Fraction for Charmless $B \to h^0 h^0$ Decays", *BABAR* analysis document #148, Version 6, 2001.

[48] R. Lui and F. Le Diberder,
http://www.slac.stanford.edu/BFROOT/www/Physics/Analysis/AWG/
chrmls_hadronic/meetings/Dec07_01/ran.ps.

[49] F. Blanc and J. G. Smith, private Communication.

[50] S. Menke, "Treatment of correlated systematic errors", *BABAR* analysis document #387, Version 1, 2002.

[51] C. Touramanis *et al.*, The *BABAR* Luminosity working group, "Luminosity measurement for the Run 1 data", *BABAR* analysis document #229, Version 1, 2001.
http://babar-hn.slac.stanford.edu:5090/HyperNews/get/luminosity.
html,

[52] R. Cahn and A. Roodman, "Update on Projections for the measurement of α in $B \to \pi\pi$", Sept 2002,
http://www.slac.stanford.edu/BFROOT/www/Organization/CollabMtgs/
2002/detSep2002/Tues3b/cahn.pdf

[53] A. Roodman *et al.*, "Physics at a 10^{36} Asymmetric B Factory", Prepared for APS / DPF / DPB Summer Study on the Future of Particle Physics (Snowmass 2001), Snowmass, Colorado, 30 Jun - 21 Jul 2001. [SLAC-PUB-8970].

[54] D. Hitlin, "B physics with an Asymmetric 10^{36} e^+e^- Collider", www.physics.
purdue.edu/Snowmass2001_E2/slides_0704/Hitlin_0704.pdf